

# **Photomixers as tunable terahertz local oscillators**

## **Dissertation**

zur

Erlangung des Doktorgrades (Dr. rer. nat.)

der

Mathematisch-Naturwissenschaftlichen Fakultät

der

Rheinischen Friedrich-Wilhelms-Universität Bonn

vorgelegt von

Iván Cámara Mayorga

aus

Madrid (Spanien)

Bonn 2008

Angefertigt mit Genehmigung der Mathematisch-Naturwissenschaftlichen  
Fakultät der Rheinischen Friedrich-Wilhelms-Universität Bonn

1. Referent: Prof. Dr. Karl Menten

2. Referent: Prof. Dr. Karl Maier

Tag der Promotion: 18 September 2008

Diese Dissertation ist auf dem Hochschulschriftenserver der ULB Bonn  
[http://hss.ulb.uni-bonn.de/diss online/](http://hss.ulb.uni-bonn.de/diss_online/) elektronisch publiziert

Dedico este trabajo a mi esposa, Evgenia Muraviova.



# Abstract

This work reports on the development of the photomixing technology and its immediate application to realize a tunable coherent source in the terahertz (THz) frequency range with an unprecedented bandwidth. An extensive experimental study of low-temperature-grown gallium arsenide (LT-GaAs) and ion-implanted GaAs as photomixing materials is performed in order to determine the optimal material parameters and fabrication conditions.

Defect Engineering allows to create photoconducting materials with outstanding properties for THz signal generation. The type and concentration of semiconductor defects has a critical importance in the performance of the material used for photomixing. In LT-GaAs, defects are highly dependent on the arsenic beam equivalent pressure (BEP), growth and anneal temperature. Unfortunately, the growth temperature at which an LT-GaAs sample shows optimal properties lacks very often of fabrication reproducibility. In contrast to LT-GaAs, the defects created in ion-implanted GaAs can be tailored by varying the implantation dose and energy. In order to achieve a given concentration of defects, Monte Carlo simulations were performed to determine optimal implantation conditions. The precise control over implantation dose and energy allows to overcome the reproducibility limitations of LT-GaAs.

Photomixers were fabricated patterning Ti/Au interdigitated electrodes by electron beam lithography on the feed point of different planar antenna designs (resonant dipoles and broadband logarithmic spirals). Electromagnetic simulations of the radiating structures are shown. In addition, semiconductor simulations were performed, revealing the build-up of space charge regions next to the electrodes. The problematic of space charge formation is analyzed and discussed.

Experiments with optimized photomixers demonstrate successfully pumping of astronomical heterodyne receivers at 450 GHz with a superconductor-insulator-superconductor (SIS) mixer and at 750 GHz with a hot-electron-bolometer (HEB) mixer. The double sideband (DSB) noise temperature of the astronomical receiver pumped by a photomixer and by a solid state local oscillator (both measured at an intermediate frequency band of 2 to 4 GHz) were identical ( $T_{receiver} = 170$  K).

In addition to the photomixing results, the issue of frequency stabilization

of free-running lasers is covered. Experiments were performed using an optical comb generator as a relative frequency reference. Under the frequency lock condition, the beat signal fulfilled the linewidth requirements for the photomixing system to be used as a local oscillator for heterodyne receivers in radio astronomy.

# Contents

<b>Abstract</b>	<b>i</b>
<b>1 Introduction</b>	<b>1</b>
<b>2 Principles of photomixing</b>	<b>7</b>
2.1 Introduction . . . . .	7
2.2 Basics of photomixing . . . . .	7
2.3 Carrier injection in recombination- and transit time-limited photomixers . . . . .	9
2.4 Photoconduction kinetics . . . . .	10
2.5 Modeling of small-area recombination lifetime-limited photomixers . . . . .	11
<b>3 Materials for terahertz photomixing</b>	<b>15</b>
3.1 Introduction . . . . .	15
3.2 Optical absorption in gallium arsenide . . . . .	15
3.3 Defects in gallium arsenide . . . . .	16
3.4 Measurement of subpicosecond carrier dynamics . . . . .	19
3.5 Low-temperature-grown GaAs: Fabrication and control of defects . . . . .	21
3.6 Ion implanted gallium-arsenide . . . . .	23
<b>4 Measurement setup for THz photomixing</b>	<b>27</b>
4.1 Introduction . . . . .	27
4.2 Optical system . . . . .	27
4.3 The Photomixing device . . . . .	33
4.3.1 The MSM structure . . . . .	34

Capacity of the interdigitated structure . . . . .	34
Build-up of space-charge regions . . . . .	35
Simulations of the photomixing device . . . . .	40
4.3.2 Quasi-optics . . . . .	48
4.3.3 Antenna designs . . . . .	51
Resonant designs . . . . .	54
Broadband designs . . . . .	56
<b>5 Measurements with LT-GaAs photomixers</b>	<b>61</b>
5.1 Introduction . . . . .	61
5.2 Measurements . . . . .	61
5.2.1 The effect of bias voltage . . . . .	62
5.2.2 The effect of laser power . . . . .	65
5.2.3 Cryogenic operation . . . . .	68
<b>6 Measurements with ion-implanted GaAs photomixers</b>	<b>73</b>
6.1 Introduction . . . . .	73
6.2 Motivation . . . . .	73
6.3 Fabrication . . . . .	74
6.4 Measurements . . . . .	76
<b>7 Terahertz photonic mixers as local oscillators for SIS and HEB receivers.</b>	<b>81</b>
7.1 Introduction . . . . .	81
7.2 Motivation . . . . .	81
7.3 Mixing experiment with an SIS receiver at 450 GHz . . . . .	82
7.4 Mixing experiment with a HEB at 750 GHz . . . . .	85
<b>8 Conclusions and future work</b>	<b>91</b>



---

<b>A</b>	<b>Relative frequency stabilization of free-running lasers.</b>	<b>93</b>
A.1	Introduction . . . . .	93
A.2	Motivation for the frequency stabilization of free-running lasers	93
A.3	The optical comb generator . . . . .	95
A.4	The electro-optic modulator . . . . .	98
A.5	Measurements with the optical comb . . . . .	99
A.6	Relative frequency stabilization with a comb generator . . .	105
A.7	Conclusions and future work . . . . .	106
	<b>Bibliography</b>	<b>107</b>
	<b>Acknowledgments</b>	<b>115</b>
	<b>Publications and Conferences</b>	<b>117</b>
	<b>Curriculum Vitae</b>	<b>131</b>



# Chapter 1

## Introduction

The concept of photomixing, or optical heterodyne downconversion, was tested experimentally for the first time in 1962 [1], [2], [3]; only two years after the availability of the first solid-state laser [4] as an optical coherent source. Photomixing is a process in which a photodetector converts an optical signal consisting of two or more wavelengths into an electrical signal. The latter signal contains the mixing or beat of the different frequency components. The photodetector is usually located in the feed-point of a planar antenna, which is optimized to couple the beat signal to free space. Seen as a whole, photomixing could be misinterpreted as a non-linear process, but this would be wrong, since both the optical and electrical processes involved in photomixing are completely linear. Examples of devices making use of electrical non-linear processes for generation of terahertz radiation are Gunn oscillators (as a source) and Schottky varactor diodes (as frequency multipliers). On the other hand, devices making use of optical non-linear processes for direct optical generation of THz signals [6] are difference frequency generation (DFG) crystals like zinc germanium phosphide ( $ZnGeP_2$ ). The process involves the second order susceptibility term  $\chi^{(2)}$ . Through the interaction of two optical waves in the non linear crystal, difference frequency photons are generated. The main drawback of this THz generation method in comparison to photomixing is that for a second order non-linear process to occur, the electric field in the optical medium created by the laser must be comparable to the atomic electric field  $E_{atom} = \frac{1}{4\pi\epsilon} \cdot \frac{e}{a_0^2} \approx 6 \cdot 10^{11} V/m$ , where  $e$  and  $a_0$  are the electron charge and Bohr radius, respectively. These extremely high electric fields require laser powers of hundreds of Watts for systems focused to the diffraction limit for continuous-wave operation. A way to reduce the power requirements is to increase the interaction length of the non-linear optical medium. Nevertheless the difference between the phase velocity of the THz signal and group velocity of the optical signal reduces the maximum attainable length (coherence length) to typically hundreds of  $\mu m$ . Quasi-phase matching by periodically poling the optical medium addresses this problem. Up to date, efficient terahertz generation by non-linear optical processes, has been demonstrated in a pulsed regime with femtosecond

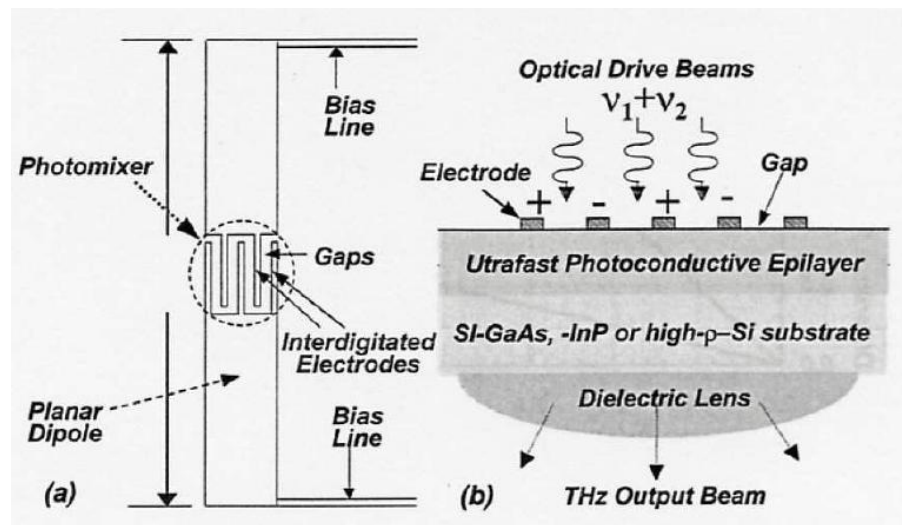


**Fig. 1.1:** (a) Small area MSM interdigitated photomixer on the feed-point of a planar dipole antenna. (b) Photomixer cross-section. The THz radiation is collimated through a dielectric lens to free space. From [5].

lasers. In the pulsed regime huge instantaneous electric fields are generated that give rise to the desired non-linear optical process. In the pulsed operation, the THz emission is broadband, making impossible its use for applications which require a high spectral purity.

In contrast to photodetectors, which are employed to convert optically coded information signals – a band of frequencies – into an electrical signal, photomixers are optimized to deliver a mixing signal – usually a very sharp frequency component – inside a certain frequency band. We can classify photomixers according to their physical dimensions in:

- Small area photomixers. The area where photomixing takes place is much smaller than the wavelength of the beat signal. Some examples are photomixers with a metal-semiconductor-metal (MSM) interdigitated structure (see figure 1.1) on an ultra-fast semiconductor, NIP-NIP superlattice ballistic photomixers [8] and Uni-travelling-carrier photodiodes [9].
- Large area photomixers. A traveling-wave with the mixing signal is generated along a transmission line. The area where photomixing takes place is comparable to the wavelength of the beat signal. Usually the phase velocity of the mixing signal is matched to the group velocity of the optical wave by different approaches. Figures 1.2 and 1.3 show a planar travelling-wave structure and a PIN travelling-wave based photomixers respectively.

Recently, an interesting photomixing device using high temperature super-

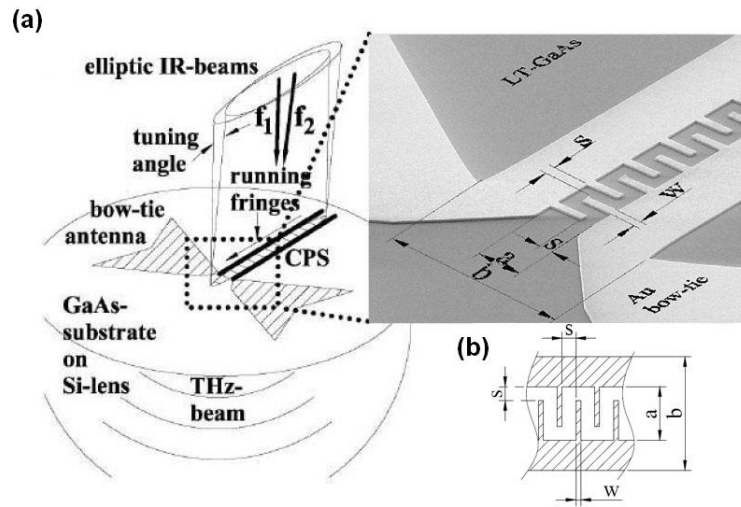


**Fig. 1.2:** (a) Laser interference fringes are velocity matched to the intermediate frequency wave on the coplanar stripline by tuning the angle between the both laser beams (inset) Scanning electron microscope picture of a traveling-wave metal-semiconductor-metal (TW-MSM) device showing the feed point of a bow-tie antenna (b) A section of the TW-MSM structure. From [7].

conductors (HTS) has been proposed by Saeedkia [10] (see figure 1.4)<sup>1</sup>. In these novel devices, the supercurrent flowing through a superconductor stripe is modulated by the optical signal. The mixing signal is generated by the interaction of the incoming photons with the superconductor electrons: these photons split Cooper pairs almost instantaneously, reducing the supercurrent. The splitted electrons then relax back to the superconducting condensed state on a few picoseconds timescale. There is a limit to the maximum beat frequency, which is imposed by the gap frequency of the superconducting film. Beyond this limit the energy of the mixing signal is sufficient to break additional Cooper pairs, thereby reducing the efficiency of the device. These attractive devices open up the exciting possibility of creating a THz current directly on a radiating antenna.

This work focuses on the generation of THz radiation by photomixing in small area photomixers and is organized as follows:

- Chapter 2 gives a brief theoretical description of the photomixing process and explains the properties that a material must exhibit in order to be optimal for photomixing applications.
- Chapter 3 focuses on gallium arsenide as a photomixing material. The role of defects to account for the ultrafast carrier lifetimes ob-

<sup>1</sup>The idea of using High Temperature Superconductors was originally developed for pulsed terahertz generation by Tonouchi [11]

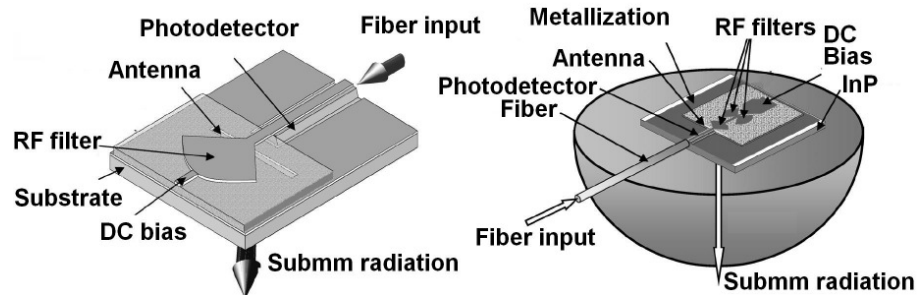


**Fig. 1.3:** (Left) Schematic of a photonic 0.46 THz transmitter consisting of a TW photodetector monolithically integrated with a planar full-wave single slot antenna and submm-wave filter structures to enable the dc-bias supply for the detector. (Right) Schematic of a photonic transmitter chip mounted on a hemispherical silicon lens. From [12].

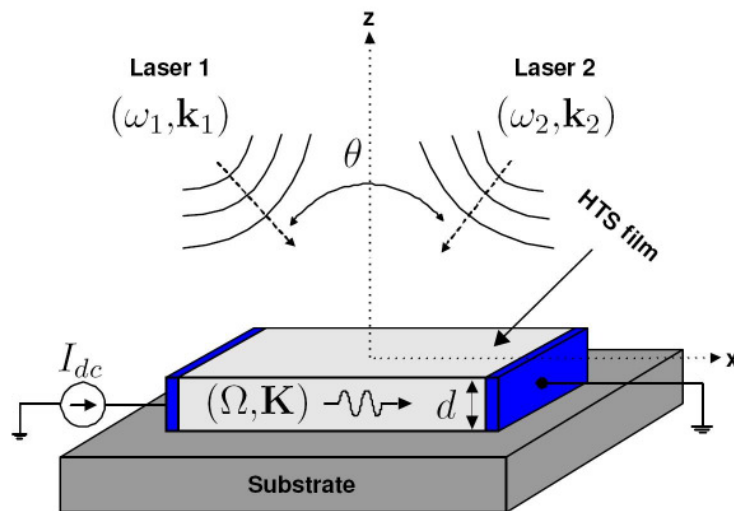


**Fig. 1.4:** Schematic of superconducting photomixing. Taken from [13].

served in this material is discussed. The fabrication and characteristics of low-temperature-grown gallium arsenide (LT GaAs) and ion-implanted GaAs are shown.

- Chapter 4 describes the laboratory setup used for photomixing. The photomixer device is presented as well as electromagnetic and semiconductor simulations.
- Chapter 5 deals with LT GaAs measurements performed at room temperature and cryogenic temperatures.
- Chapter 6 shows measurements with ion-implanted photomixers
- Chapter 7 describes experiments performed with photomixers as local oscillators for radio astronomical receivers.
- The outlook and perspectives of this work are discussed in chapter 8
- Finally, appendix A presents the technique of optical comb generation for frequency stabilization of free-running lasers. Frequency locking experiments are shown.





# Chapter 2

## Principles of photomixing

### 2.1 Introduction

This chapter gives a theoretical overview of the photomixing kinetics and describes the differences between the recombination- and transit time-limited photomixers. The dependence of the small signal photocurrent on important parameters like frequency, carrier lifetime and irradiance is discussed.

### 2.2 Basics of photomixing

If two monochromatic plane waves

$$\mathbf{E}_1(t) = \mathbf{E}_1 \cdot e^{j\mathbf{k}_1 \cdot \mathbf{z} - j\omega_1 t}, \mathbf{E}_2(t) = \mathbf{E}_2 \cdot e^{j\mathbf{k}_2 \cdot \mathbf{z} - j\omega_2 t} \quad (2.1)$$

interfere on the surface of a semiconductor (which is taken at  $z = 0$  as reference and the  $-z$  direction is defined towards the substrate), the phasorial expression for the total electric field on the semiconductor surface can be described as:

$$\mathbf{E}_T(t) = \mathbf{E}_1(t) + \mathbf{E}_2(t) = |_{z=0} \mathbf{E}_1 \cdot e^{-j\omega_1 t} + \mathbf{E}_2 \cdot e^{-j\omega_2 t} \quad (2.2)$$

where the plane waves are supposed to incide perpendicularly to the semiconductor surface ( $\hat{k}_1 = \hat{k}_2 = \hat{z}$ ). In figure 2.1, the real part of the total electric field phasor on the semiconductor surface  $\mathbf{E}_T(t)|_{z=0}$  for two monochromatic sources is plotted. The incoming photons will be absorbed if their energy is above the energy gap of the semiconductor. This energy will be used to raise electrons from the valence band to the conduction band, thus creating electron-hole pairs. In case that the photon energy is much higher than the strictly necessary, i. e. much greater than the energy gap,  $E_g$ , through a thermalization process, the electrons lose their excess energy in form of lattice vibrations or phonons. By the photogeneration of

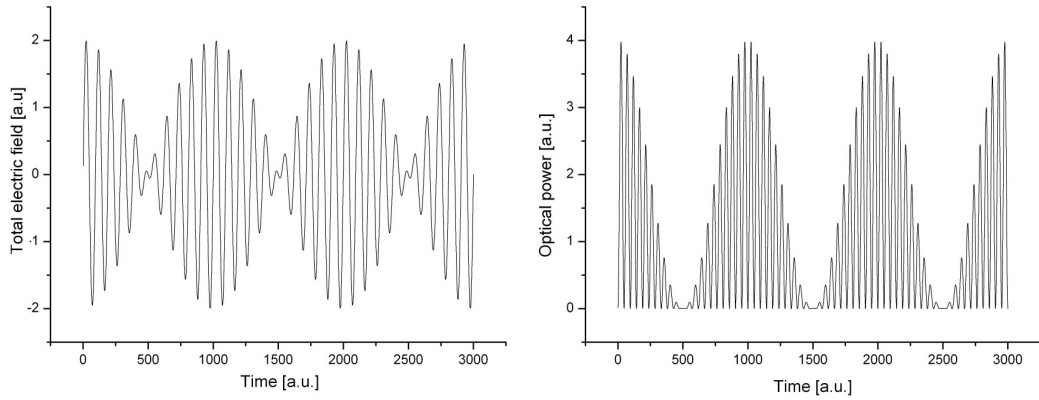


**Fig. 2.1:** Total electric field at  $z=0$  (left) and power (right) from the beat between two frequencies. The frequency difference between  $\mathbf{E}_1(t)$  and  $\mathbf{E}_2(t)$  ( $f_2 - f_1$ ) is one order of magnitude smaller than the absolute frequency of the central frequency ( $f_0 \simeq f_1, f_2$ ).

electron-hole pairs, so called photocarriers, the conductivity  $\sigma(z, t)$  of the semiconductor increases proportionally to the absorbed optical power or amount of absorbed photons <sup>1</sup>:

$$\begin{aligned} \sigma(z, t) &\propto e^{\alpha 2z} |\mathbf{E}_1(t) + \mathbf{E}_2(t)|^2 = \\ &e^{\alpha 2z} \cdot (\mathbf{E}_1 \cdot e^{-j\omega_1 t} + \mathbf{E}_2 \cdot e^{-j\omega_2 t}) \cdot (\mathbf{E}_1 \cdot e^{-j\omega_1 t} + \mathbf{E}_2 \cdot e^{-j\omega_2 t})^* = \\ &e^{\alpha 2z} \cdot \left\{ |\mathbf{E}_1|^2 + |\mathbf{E}_2|^2 + \frac{|\mathbf{E}_1|^2}{2} \cdot \cos 2\omega_1 t + \frac{|\mathbf{E}_2|^2}{2} \cdot \cos 2\omega_2 t \right. \\ &\quad \left. + |\mathbf{E}_1 \cdot \mathbf{E}_2| \cdot \cos(\omega_1 + \omega_2)t + |\mathbf{E}_1 \cdot \mathbf{E}_2| \cdot \cos(\omega_1 - \omega_2)t \right\} \end{aligned} \quad (2.3)$$

where  $\alpha$  is the semiconductor optical absorption coefficient.

The photogenerated electron-hole pairs will only exist for a certain amount of time, after which they:

- Recombine:
  - directly between conduction and valence bands (inter-band transition)
  - assisted by an intermediate energy level (intra-band transition).

thereby emitting phonons or photons –radiative recombination. The related timescale is known as recombination lifetime.

<sup>1</sup>To be completely strict this is not completely exact since in the framework of quantum optics, the number of photons, which is described by the number state  $|n\rangle$ , does not commute with the electric field. The existence of shot noise or quantum noise derives from this non-commutativity.

- Become trapped in a hole or electron trap. From the trap the carrier can be re-emitted or, in case that a counterpart carrier interacts with the trap, recombine. Traps will be presented in section 3.3.
- Reach the electrodes. The related timescale is known as transit time.

Depending on the dominant process by which the photocarriers disappear, we speak about recombination-lifetime or transit-time limited photodetectors [14]. In this thesis we will focus on the former type of photodetector.

The electron-hole recombination process has a time constant of several hundreds of femtoseconds in the fastest semiconductors and is the main power limiting mechanism at THz frequencies for recombination limited photomixers. If an external electric field is applied to the semiconductor, the photoelectrons and holes are swept by the applied electric field and a current "photocurrent" will flow. The total photocurrent can be calculated from the well known expression for the current density :

$$\mathbf{J}(\mathbf{r}, t) = \sigma(\mathbf{r}, t) \cdot \mathbf{E}_{bias}(\mathbf{r}) \quad (2.4)$$

As seen in figure 2.1, the optical power contains the terms of the last expression:

- a.) A DC component  $|\mathbf{E}_1|^2 + |\mathbf{E}_2|^2$ , responsible for the positive average value of the optical power.
- b.) High frequency components  $\frac{|\mathbf{E}_1|^2}{2} \cdot \cos 2\omega_1 t + \frac{|\mathbf{E}_2|^2}{2} \cdot \cos 2\omega_2 t + |\mathbf{E}_1 \cdot \mathbf{E}_2| \cdot \cos(\omega_1 + \omega_2)t$ , responsible for the "fast" variations of the optical power.
- c.) A difference frequency component  $|\mathbf{E}_1 \cdot \mathbf{E}_2| \cdot \cos(\omega_1 - \omega_2)t$ , responsible for the observed envelope curve.

The fast optical power variations in b.) can not be "followed" by the photocurrent, since their timescale is around four orders of magnitude above the response time of the fastest semiconductors. On the other hand, the difference frequency component c.), or envelope of the optical power, can be "followed" by the photocarriers up to several terahertz [15] in certain semiconductors and therefore is susceptible to be converted to an electrical signal. This difference frequency component will be maximized in case that both plane waves have the same polarization and amplitude ( $\mathbf{E}_1 = \mathbf{E}_2$ ).

## 2.3 Carrier injection in recombination- and transit time-limited photomixers

The bandwidth of a photomixer is determined by how fast it is able to translate the incoming optical power changes to photocurrent changes. Therefore, an ideal photomixer has a Dirac delta transfer function. If we consider

the event of a single photon being absorbed, an electron-hole pair is immediately created and a photocurrent will flow until **both** carriers recombine, get trapped or reach the electrodes. When a photocarrier reaches its corresponding electrode, its contribution to the photocurrent does not necessarily end, since in order to maintain space-charge neutrality in the semiconductor region between electrodes, an additional carrier is injected from the electrodes (supposing ohmic contacts). The timescale in which the carrier is injected, is given by the dielectric relaxation time  $\tau_{dielectric} = \epsilon\epsilon_0/\sigma$  (unless  $\tau_{dielectric} > \tau_{drift}$ ). For practical photomixers,  $\tau_{dielectric}$  is in the sub-picosecond range.

In high-speed transit-time limited photomixers, the drift time is several orders of magnitude below the recombination time. Usually, the hole drift velocity is much smaller than the electron drift velocity, so that electrons might be injected several times –as often as necessary until the hole reaches the cathode. As a consequence, the time constant in these photomixers is determined by the hole drift time. Therefore, for transit time-limited photomixers, thin drift zones are preferred, so that the holes reach the cathode as fast as possible. Unfortunately, thin drift zones have usually a negative impact on the photoresponsivity and capacity.

For recombination time-limited photomixers,  $\tau_{dielectric} = \epsilon\epsilon_0/\sigma \propto 1/\tau_{lifetime}$  is several orders of magnitude larger than in transit-time limited photomixers, due to the reduced carrier lifetime, so that the mentioned carrier injection processes occur in a time scale much larger than the carrier lifetime.

## 2.4 Photoconduction kinetics

Let us consider a semiconductor material in thermodynamical equilibrium. The concentrations of electrons and holes with no light impinging are  $n_0$  and  $p_0$ . Under these conditions the conductivity of the sample is:

$$\sigma_d = e(n_0\mu_n + p_0\mu_p) \quad (2.5)$$

where  $\mu_n$  and  $\mu_p$  are the electron and holes mobilities. This dark conductivity is due to thermally excited electron and holes and consequently temperature dependent. In photodetectors it represents a source of noise (Johnson noise).

If the sample, whose surface is taken as the origin of the  $z$  axis, is uniformly illuminated by photons of frequency  $\nu$  and the irradiance on the semiconductor surface is  $I_0$ , the electron-hole generation rate is given by:

$$G_0(z) = \alpha\eta \frac{I_0(1-R)}{h\nu} e^{\alpha z} \quad (2.6)$$

where  $\alpha$  is the absorption coefficient,  $\eta$  the quantum efficiency,  $R$  is the Fresnel reflection coefficient at the air-semiconductor interface,  $h$  the

Planck constant and the  $-z$  direction is defined towards the substrate. The photogenerated electrons and holes exist during a time  $\tau_n$  and  $\tau_p$ , respectively. The steady-state concentration of photoelectrons is given by  $n_{ph} = G_0(\mathbf{r})\tau_n$  and for holes  $p_{ph} = G_0(\mathbf{r})\tau_p$ . In the case of a time dependent irradiance the generation rate contains an additional time dependent term in the same fashion as the expression for the time dependent conductivity given by formula 2.3. In order to calculate analytically the current density in a photoconductor, the continuity equations must be solved:

$$\frac{\partial n(\mathbf{r}, t)}{\partial t} = \frac{1}{e} \cdot \nabla \cdot \mathbf{J}_n(\mathbf{r}, t) + G(\mathbf{r}, t) - R_n(\mathbf{r}, t) \quad (2.7)$$

$$\frac{\partial p(\mathbf{r}, t)}{\partial t} = -\frac{1}{e} \cdot \nabla \cdot \mathbf{J}_p(\mathbf{r}, t) + G(\mathbf{r}, t) - R_p(\mathbf{r}, t) \quad (2.8)$$

where  $R_n(\mathbf{r}, t) = n(\mathbf{r}, t)\tau_n^{-1}$ ,  $R_p(\mathbf{r}, t) = p(\mathbf{r}, t)\tau_p^{-1}$  represent the recombination rates for electron and holes. The current densities consist of a drift and a diffusion term:

$$\mathbf{J}_n(\mathbf{r}, t) = e \cdot n(\mathbf{r}, t) \cdot \mathbf{v}_n(\mathbf{r}, t, \mu_n(E), E) + eD_n \nabla n(\mathbf{r}, t) \quad (2.9)$$

$$\mathbf{J}_p(\mathbf{r}, t) = e \cdot p(\mathbf{r}, t) \cdot \mathbf{v}_p(\mathbf{r}, t, \mu_p(E), E) + eD_p \nabla p(\mathbf{r}, t) \quad (2.10)$$

where  $\mathbf{v}_{n(p)}(\mathbf{r}, t)$  is the drift velocity and  $D_{n(p)}$  are the diffusion coefficients for electrons (holes). Note that for the high electric fields at which photomixers are usually operated, the mobility depends on the electric field. Finally, using Poisson's equation

$$\nabla \cdot \mathbf{E}(\mathbf{r}, t) = \frac{e}{\epsilon} (p(\mathbf{r}, t) - n(\mathbf{r}, t)) \quad (2.11)$$

we have a complete set of equations from which the current density can be calculated.

## 2.5 Modeling of small-area recombination lifetime-limited photomixers

Remarkable efforts [16] have been undertaken to solve analytically the set of nonlinear coupled differential equations 2.9, 2.10 and 2.11 for the case of small area photomixers. It is important to outline that the electric field in the semiconductor has large variations as it approaches the electrodes (this will be illustrated in section 4.3.1) so that a parallel plate approximation for the electric field yields inaccurate results. This fact makes it a nonviable task to find an analytic solution for the photocurrents. Nevertheless, the expression of the longitudinal component - between electrodes - of the current density calculated for the case of a constant electric field is of great interest since, although it is not completely exact, it gives good

insight for the DC and AC components and their relationship. If we consider that the finger structure exhibits a capacity  $C$  and that the resistance seen by the photomixer due to the biasing circuit and/or antenna equals  $R$ , then [16]:

$$\mathbf{J}_x(z, t) \approx G_0(z) \cdot e \left[ (\tau_n v_n + \tau_p v_p) + \left( \frac{\tau_n v_n}{\sqrt{1 + (\omega \tau_n)^2} \sqrt{1 + (\omega RC)^2}} + \frac{\tau_p v_p}{\sqrt{1 + (\omega \tau_p)^2} \sqrt{1 + (\omega RC)^2}} \right) \cos(\omega t + kz) \right] \quad (2.12)$$

We can see that the AC photocurrent equals the DC photocurrent for small frequencies. The Lorentz factors present in the denominator of formula 2.12 restrict the photomixer performance at high frequencies since they introduce two cut-off frequencies related to the carrier lifetime  $\tau$  and the photomixer RC constant.

By integration of the longitudinal component of the current density over the whole photomixer active region we obtain the total photocurrent. Taking some approximations [17] as small-signal limit and provided that the power and polarization of the plane-waves interfering on the photomixer are equal, the expression for the rf power yields:

$$P_{rf} = \frac{R}{2} \frac{(V_b G_0)^2}{\sqrt{1 + \omega^2 \tau^2}} \cdot \frac{1}{\sqrt{1 + \omega^2 (RC)^2}} \quad (2.13)$$

where  $V_b$  is the bias voltage and  $G_0$  is the photomixer DC conductance. In a log-log rf power *versus* frequency plot of formula 2.13, two frequency roll-off's of 20 dB/decade (or 6 dB/octave) are present, which are associated with the RC constant and effective <sup>3</sup>carrier lifetime. There are several techniques that promise to cancel the effect of the RC constant-related roll-off: the travelling wave concept [18] and the technique proposed and demonstrated by Duffy [19], in which the capacitive behavior of the interdigitated structure is compensated by an inductive tuning of the last  $\lambda/4$  section of the rf choke in photomixers with integrated resonant antennas.

As we shall see, the electrons contribute mainly to the photocurrent at high frequencies due to their higher saturation velocity and smaller trapping time. Since the main interest of photomixers is the generation of

<sup>2</sup>In general the photomixer does not see a pure-real impedance. This can only be fulfilled by certain broadband antennas – which show a constant impedance over a large frequency range –, the bond wires used to bias the photomixer structure are situated at the outer extremes of the antenna so that the effect of the biasing circuit can be neglected for sufficiently large (in terms of mixing frequency wavelength) antennas. For the case of photomixers driving resonant antennas, an rf choke is implemented to avoid power leakage towards the biasing circuit. It usually consists of a butterfly choke or of alternating high-impedance low-impedance  $\lambda/4$  sections, which are inherently resonant and can only offer a purely real impedance at certain frequencies.

<sup>3</sup>accounts for both electron and hole carrier lifetime.

a difference frequency signal, the DC part of the photocurrent does not provide any benefit and is the main source of Joule effect heating in the photomixer. Formula 2.12 shows that a high drift velocity is always beneficial for a high AC photocurrent, whereas the effect of the carrier lifetime depends on the difference frequency. At low ( $\omega\tau \ll 1$ ) and moderate ( $\omega\tau \approx 1$ ) difference frequencies the current density strongly depends on the carrier lifetime. At high frequencies ( $\omega\tau \gg 1$ ), formula 2.12 becomes independent of the carrier lifetime. From this fact one could conclude that at high frequencies, photomixing materials with different carrier lifetimes should behave identically in terms of power generation and that at small and moderate frequencies the power achieved by long carrier lifetime materials should be higher than that achieved by short carrier lifetime materials. This is completely contrary to the empirical data which show the trend of a higher rf power for short carrier lifetime in defect-rich gallium arsenide (GaAs). The apparent contradiction between theory and experiment arises from the supposition that the carrier velocity in formula 2.12 remains unaltered with the carrier lifetime. Counterintuitively, Monte-Carlo simulations [20] show that GaAs samples with a low carrier lifetime exhibit a higher electron saturation velocity than samples with a larger carrier lifetime<sup>4</sup>. From this fact, we can define three regimes for the dependence of rf power with frequency:

1. Low frequency: rf power is constant and is determined by the product  $\tau_{eff} \cdot v_{eff}$ , where  $\tau_{eff}$  and  $v_{eff}$  account for the effective (ambipolar) velocity and carrier lifetime.
2. Moderate frequency: The rf power begins to drop in a 20 dB/dec fashion.
3. High frequency: The electron drift velocity determines the rf power difference between the different materials. The power roll-off equals -20dB/dec.

An additional 20 dB/dec roll-off component is present due to the  $RC$  constant, which depends on the electrode capacity (C) and antenna resistance (R). The associated cut-off frequency is given by  $\frac{1}{2\pi\sqrt{RC}}$ .

---

<sup>4</sup>This holds only if electron transit times are comparable to their lifetime, which is usually the case for photodetectors with electrode gaps in the micron or sub-micron scale





# Chapter 3

## Materials for terahertz photomixing

### 3.1 Introduction

In this chapter, the material properties and the relevant physical mechanisms for ultrafast carrier lifetimes (below 1 ps) are described. The important role of defects in semiconductors is explained as well as some experimental techniques used to study the ultrafast carrier dynamics in semiconductors.

### 3.2 Optical absorption in gallium arsenide

In the internal photoemission process, photons of certain energy are absorbed by a semiconductor, thus emitting an electron (hole) from the valence (conduction) band to the conduction (valence) band. The absorption coefficient of a semiconductor depends on many factors such as type of absorption process – indirect or direct<sup>1</sup> –, wavelength and temperature. As an example, figure 3.1 shows the absorption coefficient of gallium arsenide (GaAs) in the near infrared (NIR) range. The graph illustrates the bandgap narrowing effect with temperature as well as the exciton band responsible for the finite slope of the absorption coefficient for energies below the energy gap.

The optical absorption is a relatively fast process; typical values are in the range of several femtoseconds. On the contrary, the electron-hole recombination process which follows the absorption of a photon has a much

---

<sup>1</sup>A semiconductor is called indirect if an electron transition from the valence to the conduction band at the minimum energy gap requires the intervention of a phonon to conserve the wavevector. This reduces the absorption rate if compared to direct absorption, in which the crystalline momentum is similar in the valence and conduction band edges.

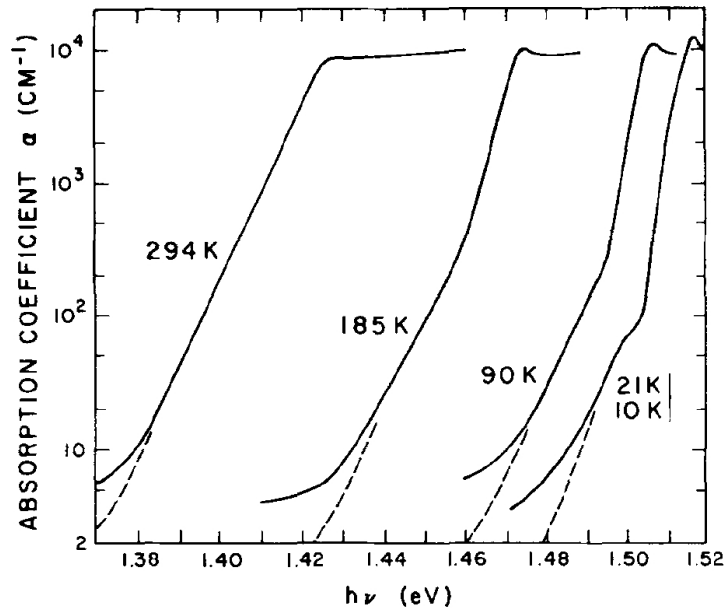


**Fig. 3.1:** Intrinsic absorption of semi-insulating GaAs at different temperatures. The dashed curves show an estimate of the absorption for an impurity-free sample. [21].

larger time scale and varies from several nanoseconds to milliseconds depending on the semiconductor. This is the main mechanism which limits the bandwidth performance of recombination-limited photodetectors.

For room temperature conditions, the energy gap of GaAs is 1.42 eV, which corresponds to a wavelength of 870 nm. Typical bulk recombination lifetimes are in the nanosecond range. Due to the strong curvature of the gamma valley (see figure 3.2), the effective electron mass,  $0.063m_0$ , is low if compared with semiconductors from the IV group or II-VI compounds. The neighboring X and L valleys may cause inter-valley scattering for high electric fields ( $>3$  kV/cm) and account for negative differential mobility, limiting the electron velocity in transit-time limited photomixers and/or ballistic transport photomixers [22].

### 3.3 Defects in gallium arsenide

For terahertz photomixing in recombination-time limited photodetectors, the carrier lifetime must be reduced to the sub-picosecond range, which is three orders of magnitude less than the carrier recombination in crystalline GaAs. In order to reduce it, defects are deliberately created during molecular-beam-epitaxy (MBE) growth in LT-GaAs or by ion implantation in GaAs. Antisites (zero-dimensional defects) and precipitates (three-dimensional defects) play a key role in GaAs as an ultrafast photoconduc-

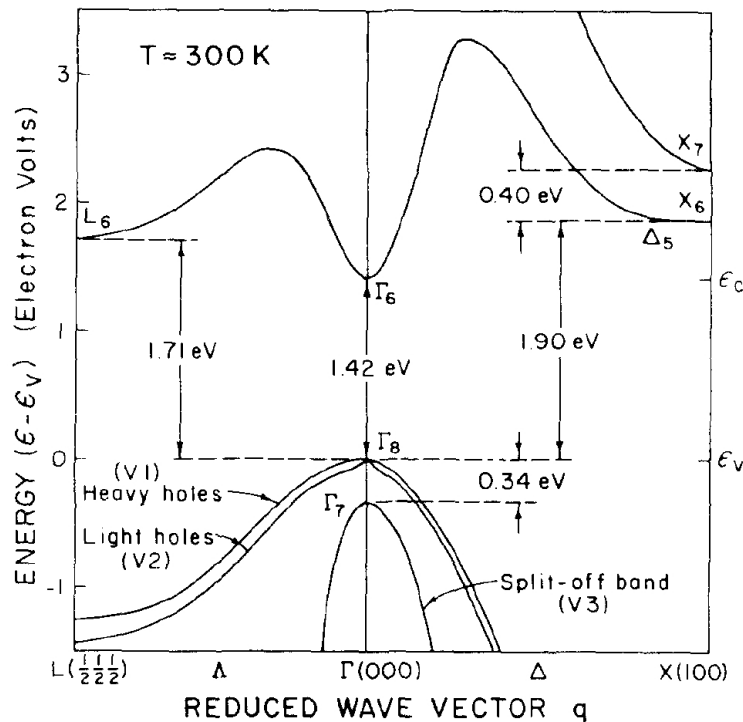


**Fig. 3.2:** Plot of the electron energy as a function of the reduced wave vector for GaAs. [23].

tive material. Some techniques enable the tailoring of the concentration and type of defects in GaAs as will be shown.

A vacancy  $V_A$  is created when an atom A is missing from its lattice position. When a host atom A occupies the position of another host atom B, an antisite  $A_B$  is produced. If a host atom A is located between the regular lattice positions (see figure 3.3), we talk about self-interstitial  $A_i$  (self-comes from the fact that the atom is originally from the lattice).

Numerous studies performed in the 90's discussed the role of arsenic antisites  $As_{Ga}$  and arsenic precipitates in the ultrafast carrier dynamics and their relative contributions. These defects have been studied by several techniques like electron paramagnetic resonance (EPR), deep transient level spectroscopy (DTLS), near-infrared absorption (NIRA), magnetic circular dichroism of absorption (MCDA), scanning tunneling microscopy (STM), positron annihilation and transmission electron microscopy (TEM).

Ionized arsenic antisites  $As_{Ga}^+$  and arsenic precipitates (Arsenic precipitates are reported to act as buried metallic Schottky contacts [24]), seem to be responsible for trapping in the sub-picosecond range. These defects are localized quantum states close to the middle of the bandgap and trap electrons from the conduction band in a timescale as low as 100 femtoseconds [25]. Since the electrons are trapped in a deep level band and not in a shallow level, their thermal re-emission back to the conduction band,

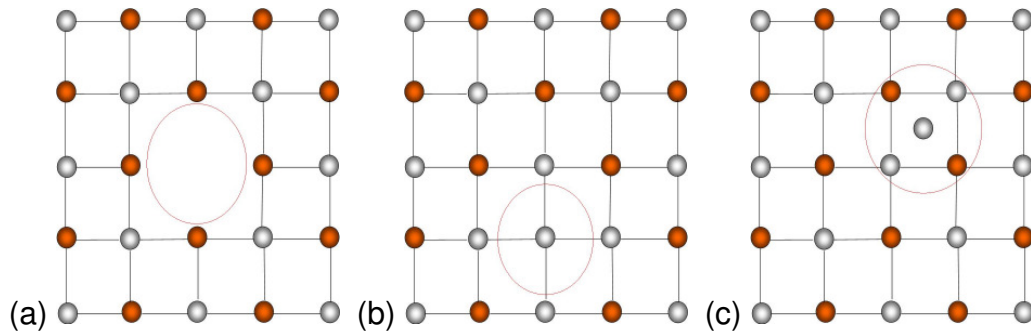


**Fig. 3.3:** An atom missing from its lattice site forms a vacancy (a) thereby substituting another atom (b) or occupying an interstitial position (c). Note: the balls are a schematic representation and do not correspond to the real atomic dimensions relative to the lattice constant.

which would increase the photoelectron lifetime, is improbable. This is due to the associated time constant of this process which is larger than that of a hole recombining with the trapped electron.

An electron trap can be:

1. empty (ionized). In this case it is positively charged and can capture an electron or emit a hole.
2. filled (unionized). In this case it is electrically neutral and can emit an electron or capture a hole (the trap acts as a recombination center).

The dynamics of recombination are modelled by the Shockley-Read-Hall recombination model [26], [27].

In GaAs, the above mentioned transitions for electron traps find place in arsenic antisites  $As_{Ga}^+$  (empty trap) and  $As_{Ga}$  (filled trap). These traps form a deep donor band, which is situated  $\approx 0.75eV$  above the valence band.

One would expect that for a material with abundant defects, the time that an electron needs to find an unoccupied trap would be shorter. Of course there is a limit for the concentration of defects, firstly, to avoid material amorphization and secondly, to maintain the dark current within an acceptable range. Defects are described quantum mechanically by a Bloch wave multiplied by a negative exponential, so that the amplitude of the wave function diminishes radially. At higher concentration of defects the wave-functions of defects begin to overlap, making electron tunneling possible between them. This process is known as hopping conductivity [28] and is responsible for increased dark currents in semiconductors with high defect concentration.

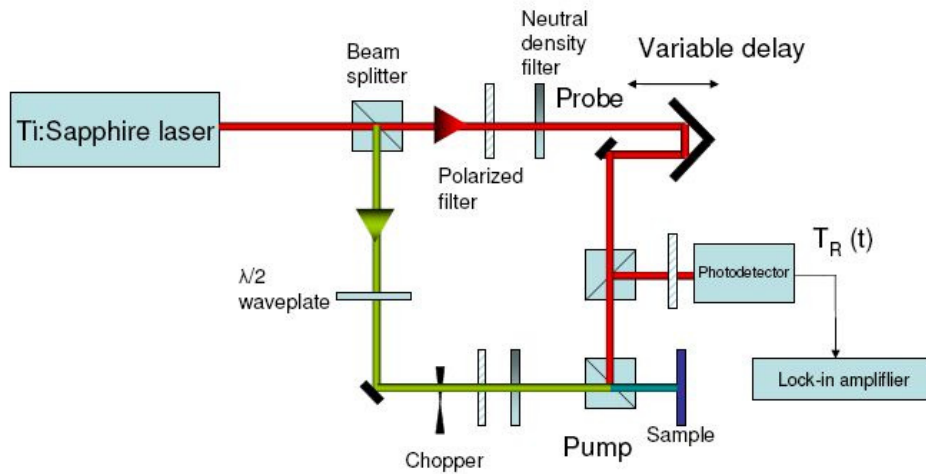


*Fig. 3.4: Setup for optical pump-probe reflectometry measurements.*

### 3.4 Measurement of subpicosecond carrier dynamics

Pure-electrical techniques are not suitable for carrier dynamics characterization of defect-rich GaAs, since the recombination and trapping processes usually occur in the picosecond and sub-picosecond range, which lies well below the acquisition time of any state-of-the-art electronic instrumentation. Electro-Optical methods are widely used since they circumvent this difficulty.

Figure 3.4 depicts a typical optical pump-probe setup for time-resolved reflectometry. A mode-locked Ti:sapphire laser operating in the 800 nm wavelength range generates pulses with typical duration of several tens of fs and a pulse repetition rate of approximately 100 MHz. A beamsplitter divides the beam into pump and probe components. The pump component passes through a  $\lambda/2$  waveplate to rotate its polarization, making it orthogonal with respect to the probe component. This allows to minimize interference effects. To obtain a time-resolved reflectivity signal, a variable time delay is introduced between the pump and probe pulses. The pump beam is chopped and focused to the sample whereas the probe beam is focused to a slightly smaller area within the pump spot. The power reflected from the probe-beam in the ultrafast sample surface is measured with a slow silicon photodiode, which is then phase-sensitively detected in a lock-in amplifier. The presence of photogenerated carriers from the pump beam changes the reflectivity of the sample and therefore the reflected probe beam power. As the time delay between pump and probe pulses is varied, the time dependent reflectivity signal can be recorded. The time resolution of this measurement technique is defined by the duration of the laser pulses. Therefore, resolutions of tens of femtoseconds are possible. Nev-

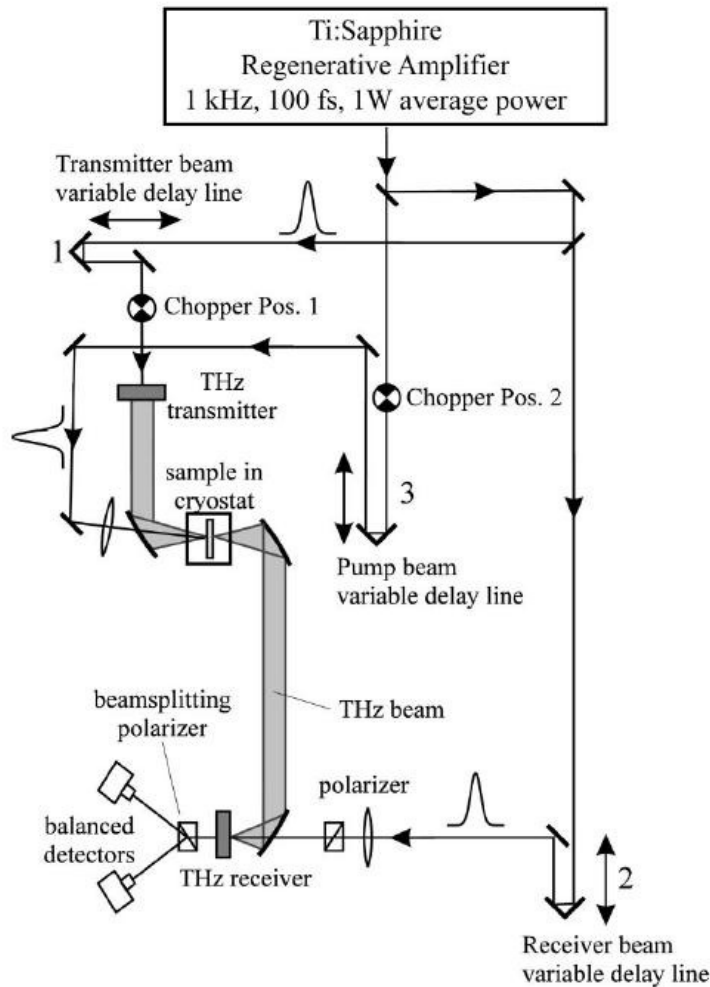


**Fig. 3.5:** Setup for time-domain terahertz spectroscopy (From [29]).

ertheless, high laser intensities are needed to get an adequate signal from the photodetector, which leads to the occurrence of undesired processes as free-carrier absorption, bandfilling, bandgap renormalization and Auger recombination. The interpretation of the data is a very complex task, from which realistic results can be rendered provided that a good model accounting for the mentioned effects is available.

There is another well established technique called time-domain terahertz spectroscopy [30]. In this technique, which is sketched in figure 3.5, the optical pulses are divided into three beams. The first (pump) beam illuminates the sample and generates electron-holes pairs in a similar manner as in pump-probe reflectometry. The second beam is coupled to a biased large-aperture GaAs antenna, inducing a transient photocurrent. From this transient photocurrent, THz pulses are generated (probe beam). These THz probe pulses are transmitted through the sample to be characterized and interact with the free carriers. From the attenuation of the THz probe beam, one can extract the concentration and mobility of carriers using the Drude model [29]. The transmitted THz probe beam is combined with

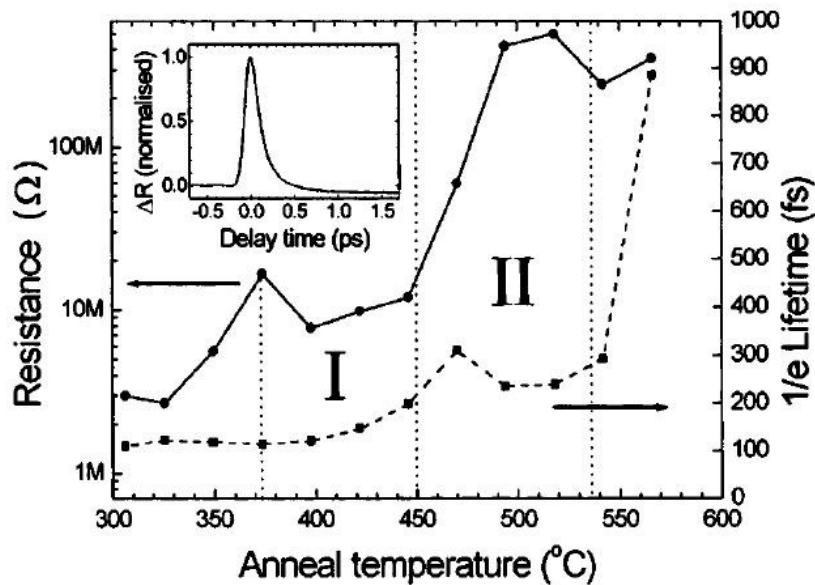


**Fig. 3.6:** Resistance and lifetime measurements for a bow-tie test antenna with a 5 mm photoconductive gap. Regions I and II are marked according to the two-stage increase in the resistivity at intermediate anneal temperatures, and correspond to expected optimum requirements for THz receivers and emitters, respectively. Inset is a sample reflectance curve for material annealed at 350 °C. Taken from [25].

the third beam. The combined (optical + THz beam) passes through an electro-optical crystal (ZnTe for example), which changes its birefringence according to the amplitude of the THz beam. The polarization components from the optical pulse are then measured in balanced photodetectors. The amplitude of the time-dependent terahertz signal containing the information of carrier dynamics is obtained by varying the time delay between the pump and probe pulse. Since low laser intensities are needed to achieve a reasonable photodetector signal, the additional absorption effects of all-optical pump-probe measurements are not present in this technique.

### 3.5 Low-temperature-grown GaAs: Fabrication and control of defects

Over the last decade, the generation of terahertz radiation by photomixing in LT-GaAs has been extensively investigated. The high electric breakdown field ( $> 300 \text{ kV/cm}$ ) and high resistivity ( $> 10^6 \Omega \text{ cm}$ ), make LT-GaAs optimal for optoelectronic applications. Despite its high density of defects, which enable ultrashort electron trapping times ( $\sim 200 \text{ fs}$ ), the carrier mobility is maintained at an acceptable range ( $> 200 \text{ cm}^2/\text{V} \cdot \text{s}$ ).

The MBE growth of this III-V compound semiconductor is performed under low temperature conditions (200 - 300°C) and with arsenic overpressure. Owing to excess arsenic (1-2%) during deposition, a non-stoichiometric, defect-rich material is created. The excess arsenic atoms can be present in the form of interstitials ( $As_i$ ) and antisites  $As_{Ga}$ . The unoccupied lattice positions of gallium atoms, gallium vacancies  $V_{Ga}$ , acts as triply charged acceptors. Ionized arsenic antisites  $As_{Ga}^+$  and arsenic precipitates seem to be responsible for electron trapping in the sub-picosecond range. The MBE growth of LT GaAs samples is usually performed on semi-insulating GaAs epitaxial buffer layers. In some cases it is useful to first grow an isolating AlAs layer to prevent the influence of the bulk GaAs electric properties on the LT-GaAs sample and to avoid arsenic diffusion toward the substrate. The LT-GaAs layer thickness is limited by its non-stoichiometry, so that typical thicknesses around 1-2  $\mu\text{m}$  can be achieved, which represent more than one optical absorption length for wavelengths in the 800 nm range. Nevertheless a technique that takes advantage of strain relaxation occurring with anneal has been reported [31] and allows the growth of LT-GaAs samples without restrictions in thickness.

The relative distribution of arsenic antisites  $As_{Ga}$  and arsenic precipitates have been reported to be highly dependent on the arsenic pressure, growth and anneal temperature. *In-situ* measurements of growth temperature are usually performed by a calibrated thermocouple. Nevertheless, the determination of the growth temperature is a complex task which depends on many factors and requires an optimal calibration. The growth temperature at which an LT-GaAs sample shows optimal properties suffers very often from unsatisfactory fabrication reproducibility.

For adequately chosen growth conditions, the as-grown sample shows already an excellent carrier trapping time due to the incorporation of excess arsenic in form of  $As_{Ga}$  with typical concentrations of  $\sim 10^{19} \text{cm}^{-3}$  [32] but usually the high hopping conductivity between these defects decreases the material resistivity (to tens of  $\Omega \text{ cm}$  [33]) preventing its use for practical optoelectronic applications.

Gebauer et al. [34] studied the defects in LT GaAs with the positron annihilation technique. The vacancies found in as-grown LT GaAs samples were identified as neutral gallium monovacancies  $V_{Ga}$ . These vacancies behave like acceptors and are ionized when the Fermi level is close to the midgap. Consequently, one should expect that the lattice temperature has a significant influence on the ionization of the  $V_{Ga}$  defects. Nevertheless, the positron annihilation experiments of Gebauer showed no dependence on temperature. The fixed proportion between the concentration of  $V_{Ga}$  with respect to that of ionized arsenic antisites  $As_{Ga}^+$  was 1:3, which coincides with the triple acceptor character of  $V_{Ga}$ , so that the  $V_{Ga}$  vacancies compensate the  $As_{Ga}^+$  antisites. From this fact they concluded that the  $V_{Ga}$  vacancies are not isolated but surrounded by  $As_{Ga}^+$  antisites, building neutral defect  $V_{Ga} - As_{Ga}$  complexes.



At room temperature, practically all  $V_{Ga}$  vacancies are ionized, in contrast to the  $As_{Ga}$  antisites, whose ionization is well below 10% [35]. In fact, the concentration of  $V_{Ga}$  vacancies dictates the concentration of ionized  $As_{Ga}$  antisites. Therefore, although in LT-GaAs the concentration of  $As_{Ga}$  might achieve relatively large values (up to  $10^{20} \text{ cm}^{-3}$  in as-grown LT GaAs, decreasing about one order of magnitude after annealing [35]), since the concentration of  $V_{Ga}$  is rather less than that of  $As_{Ga}$ , only a small fraction of the  $As_{Ga}$  will be electrically active and behave as electron traps. This motivated other groups [36] to dope with beryllium in order to activate the neutral  $As_{Ga}$  antisites, thereby increasing the concentration of electron traps.

By post-growth annealing the LT-GaAs, arsenic atoms from the  $As_{Ga}$  defects rearrange into precipitates of  $\sim 5$  nm radius [37], thereby increasing the material resistivity, carrier lifetime and recovering the mobility to values higher than  $200 \text{ cm}^2/Vs$ . Together with the growth temperature, the anneal temperature has been shown to be critical [25], and small changes of this parameter cause large variations in dark resistance, mobility and carrier trapping-time. This behavior can be clearly seen in figure 3.6.

There exist two competing models to explain the semi-insulating properties of annealed LT GaAs. On the one hand, the point defect model of Look [38], in which the Fermi level is pinned to the  $As_{Ga}$  antisite energy level, i.e. midgap. On the other hand, the precipitate model of Melloch et al. [39], in which the arsenic clusters act as buried Schottky barriers: the Fermi level is pinned close to the midgap at the arsenic clusters interface building regions that are depleted of free carriers around the clusters. As the width of these depletion regions gets comparable or larger than the average cluster spacing, a semi-insulating behavior is expected.

A detailed study of this material and its use for terahertz photomixer applications is presented in chapter 5.

## 3.6 Ion implanted gallium-arsenide

In contrast to LT GaAs, the defects created in ion-implanted GaAs [40], [41] can be tailored by varying the implantation dose and energy. The precise control over these parameters helps to overcome the reproducibility limitations of LT GaAs. By the collision of an ion beam with lattice atoms of a GaAs wafer, vacancies, interstitials and antisites are formed. As mentioned in section 3.3,  $As_{Ga}$  defects act as electron traps, so that if a GaAs wafer is implanted, yielding a similar concentration of this kind of defects one might expect similar carrier-trapping mechanisms as in LT-GaAs.

The implanted GaAs wafers presented in this work were not annealed. In contrast to LTGaAs, due to the identical concentration of arsenic and gallium in the wafers no arsenic clusters were present in the material. Con-

sequently, ultrafast electron trapping was expected to occur only in ionized arsenic antisites  $As_{Ga}^+$ . The point defect model by Look [38] for LT-GaAs might therefore be applicable for ion-implanted GaAs in order to explain its semi-insulating properties.

According to the Monte-Carlo simulations described in chapter 6, the replacement collisions by which the antisites are formed are roughly 3% of the overall displacement collisions (displacements = vacancies + replacements collisions). Due to the equal gallium and arsenic concentration and their similar cross section, under the assumption that both defects have the same thermal stability one should expect that the corresponding vacancy concentrations are the same, i. e.,  $N_{V_{Ga}} = N_{V_{As}}$ . The same applies for the antisites,  $N_{As_{Ga}} = N_{Ga_{As}}$ . From this we conclude that the concentration of  $As_{Ga}$  is 1.5% of the total vacancy concentration (i. e., 3% of the  $V_{Ga}$  concentration,  $\sim 10^{19} cm^{-3}$ ) yielding a value in the range  $10^{17} - 10^{18} cm^{-3}$ . In contrast to LT-GaAs, almost all  $As_{Ga}$  antisites are ionized since the concentration of  $V_{Ga}$  acceptors is much larger than that of  $As_{Ga}$ . Moreover, since as reported by Gebauer et al. [34], the gallium vacancies are quite mobile even at room temperature, they might tend to move to lattice positions of higher stability i. e. next to  $As_{Ga}$  antisites, thereby forming stable  $As_{Ga}-V_{Ga}$  complexes like in LT-GaAs. The gallium vacancies which cannot allocate themselves in a stable position might disappear or diffuse toward the bulk, so that the final concentration of  $V_{Ga}$  will be that strictly necessary to compensate the  $As_{Ga}$  antisites. As a consequence, the electron traps in ion-implanted GaAs will require a minimum concentration of defects and therefore display characteristics superior to LT-GaAs. These mechanisms need experimental confirmation and therefore remain speculative at the time this work was written.

It is important that to ensure that the ions do not change by themselves the properties of the material, i. e. by doping it, but rather that the induced damage by the ion bombardment defines the material properties. To achieve this, the implantation energies can be selected so that the peak of the implantation profile is situated substantially deeper than:

1. the optical absorption length in GaAs so that the implanted atoms do not change considerably the optical properties of the material.
2. the region where the electric field is significant, in order to avoid doping effects of the implanted atoms.

The first condition would lead to implantation peaks deeper than  $1 \mu m$  for wavelengths in the 800 nm range.

The second condition is less restrictive than the first one as will be shown in section 4.3.1.

In this thesis we implanted semi-insulating (100) GaAs samples with the tandem accelerator of the Institute for Nuclear Physics of the University of

Cologne. In a tandem accelerator, a source emits negative ions that are filtered in a magnetic field – in the same way as a mass spectrometer works. The ion beam is accelerated by a very high positive potential (in this case 2 Megavolts) created by a Van-de-Graaff generator. As the ion beam approaches the high voltage terminal, a foil strips some electrons from the ions leaving them positively charged and, consequently, the beam experiences another acceleration away from the positive terminal. The denomination "tandem" comes from the two acceleration processes – toward the terminal and away from it. In order to illuminate homogeneously the wafer area, the 3 mm FWHM ion beam was deflected by different wobble signals in the axes perpendicular to the propagation direction, thereby avoiding the formation of any periodic pattern. A detailed study of ion implanted GaAs and its use for terahertz photomixer applications is presented in chapter 6.



# Chapter 4

## Measurement setup for THz photomixing

### 4.1 Introduction

The optical heterodyning system used for the different photomixing experiments is described in this chapter. Different photomixer designs and electromagnetic simulations with resonant dipole antennas and broadband antennas are presented. The semiconductor structure is simulated and results showing the distribution of electrostatic field and potential are discussed. Special emphasis is given the issue of space charge formation. Last, quasi-optical simulations for antenna-to-free-space coupling and collimation of the THz beam are presented.

### 4.2 Optical system

The scheme for optical heterodyning (figure 4.1) consisted of NIR  $\sim 780$  nm continuous-wave (CW) single-mode lasers in Littman configuration (New Focus, model Velocity 6312). The lasers could be tuned continuously within 10 THz and the mode hopping range was 100 GHz. The output power of the lasers,  $\sim 6$  mW, was insufficient for satisfactory rf power generation in the photomixer, therefore a laser amplifier was included in the system. With a set of mirrors and beam splitters, the laser beams were made collinear to drive a tapered laser amplifier (TOptica TA100, figures 4.3(a) and (b)). Optical isolators at the input and output of the laser amplifier prevented optical feedback to the pump lasers and to the tapered laser amplifier. In addition, they substantially attenuated the contribution of spontaneous emission at the output. This configuration provided up to 0.5 W of combined power. The laser beam, which was mechanically chopped to enable phase-sensitive (lock-in) detection of the THz radiation, was coupled into a single-mode optical fiber ( $>99\%$ ) and to an Anritsu MS9710C

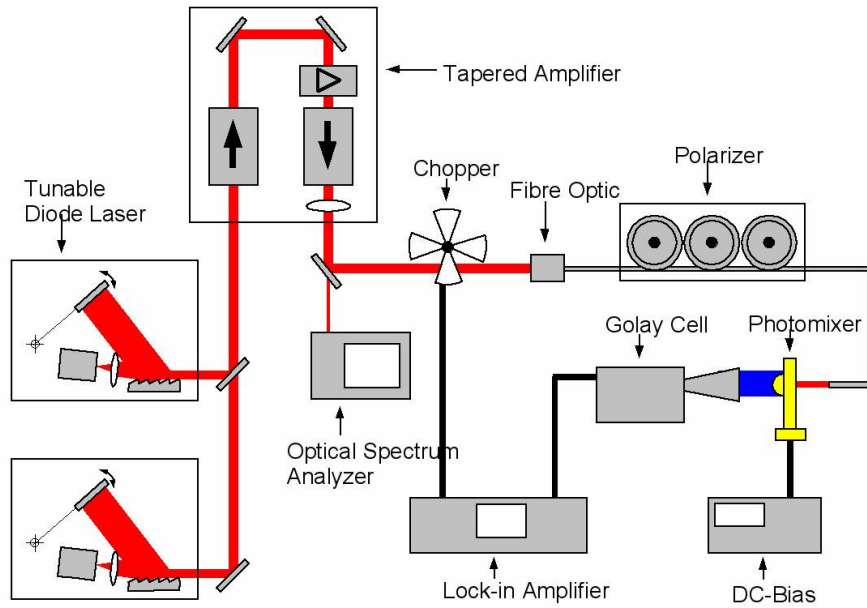


**Fig. 4.1:** Schematic diagram of the measurement setup.

optical spectrum analyzer (with  $<1\%$ ) to monitor frequency difference and to guarantee an equal power distribution between the two laser wavelengths. The coupling into the single-mode fiber optic caused spatial filtering of the multi-mode emission from the laser amplifier. The fiber optics connectors were chosen to be angled polished (APC) in order to minimize the reflection feedback. A fiber polarizer converted the laser polarization of the optical fiber input to a polarization orthogonal to the photomixer interdigitated electrodes (see figure 4.2). This procedure was mandatory to minimize reflection from the photomixer and optimize the absorbed optical power, since the finger structure has dimensions comparable to the laser wavelength and therefore acts as a grid polarizer. To achieve optimal photomixer illumination, the optical fiber was positioned with a piezoelectric element (PI nanocube P-611.3S). Its High Voltage (HV) controller allowed a position control accuracy of 100 nanometers over three orthogonal directions.

The air gap between the optical fiber and photomixer substrate acts as a Fabry-Perot etalon, so we used an optical adhesive <sup>1</sup> with a similar refractive index as the optical fiber core to pigtail the fiber optic to the photomixer. This process also inhibited the negative effects of mechanical vibrations, which potentially could lead to mispositioning of the fiber optic over time thus limiting the reproducibility of the experiments.

The DC bias supply output was previously filtered in an RC low pass filter to protect against voltage peaks, which could damage the photomixer during its connection to the bias supply. The photocurrent and dark current were measured with a precision amperemeter (Keithley 196), which

<sup>1</sup>Norland Optical Adhesive 61

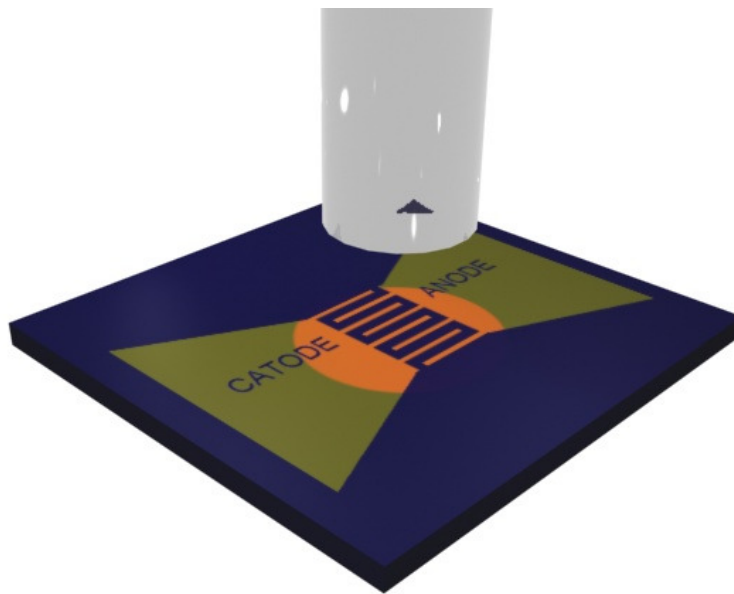


**Fig. 4.2:** Illustration of an illuminated photomixer. A single-mode optical fiber is positioned to illuminate the interdigitated area (only the fiber core is shown). Due to the  $TEM_{00}$  mode exiting the fiber, the intensity follows a Gaussian distribution, whose waist is located at the fiber end. The waist size corresponds to the fiber Mode Field Diameter (MFD, 5 micrometers approx.). Since the fiber and the semiconductor surface are separated several tens of micrometers, a distance significantly less than the Rayleigh-range ( $\sim 100\mu\text{m}$ ), the beam divergence is negligible when reaching the photomixer surface.

enabled measurements in the nA range.

A CCD camera equipped with a microscopic objective (its large working distance of several centimeters allowed placing the objective lens at an angle of 45° with respect to the photomixer surface normal) inspected the photomixer and fiber optic, in order to obtain an optimal illumination of the photoactive area (see figure 4.4).

The terahertz power emitted by the photomixers was collected by a Winston cone with a field of view of 20 degrees. This optical element is an off-axis parabola of revolution which maximizes the collection of radiation by concentrating the incoming rays to the exit aperture. The incoming radiation is funneled by multiple reflections on the parabolic surface [42]. The exit aperture was attached to the input window of our terahertz detector, a Golay cell (Tydex).

The Golay cell is a pneumatic broadband detector<sup>2</sup> in which the radiation to be measured enters a sealed chamber containing a gas –usually xenon, due to its low thermal conductivity– through a transparent window. Inside the chamber an absorber consisting of a thin metallic film –usually Gold– is mounted. As the radiation hits the metallic film, part of its energy is absorbed due to the finite electric conductivity of the metal, thereby heating and transferring heat to the gas. As the gas is heated, it expands and deforms an elastic reflecting exit window. External to the chamber, an optical system measures the deformation of the exit window. A collimated beam coming from a light-emitting diode is reflected on the exit window, with the reflection angle being dependent on the curvature radius of the surface. A photodetector delivers an electrical signal sensitive to the deformation of the window and therefore to the absorbed power. This detector shows acceptable responsivities (typically  $\sim 10^5 V/W$ ). Its response time is slow (millisecond range) when compared to helium cooled detectors but is not bulky and is operated at room temperature.

The material of the Golay cell input window was diamond, which offers an almost constant transmissivity from the NIR to the far infrared (FIR). The Golay detector had a cut-off frequency determined by the dimensions of its input circular window. In order to calculate the minimum operation frequency of the Golay cell, one can consider the input circular aperture as a circular waveguide. From microwave theory it is well-known [43] that the dominant mode is a  $TM_{01}$  mode, with a cut-off wavelength of  $\lambda = 2.61a$ , being  $a=6$  mm the waveguide diameter. From this follows that the minimum frequency the Golay can detect is  $f \approx 25$  GHz, which is well below the range of interest ( $f \gtrsim 100$  GHz). The noise equivalent power (NEP) of the Golay cell was  $100$  pW/ $\sqrt{Hz}$  at a chopping frequency of  $20$  Hz. The signal of the Golay cell was phase-detected in a lock-in amplifier. The detector maximum power was  $10$   $\mu W$  so that a dynamic range of five orders of magnitude was given.

<sup>2</sup>The principle of work reminds somewhat to what happens to the blackened vanes of a light mill (Crooke's radiometer).



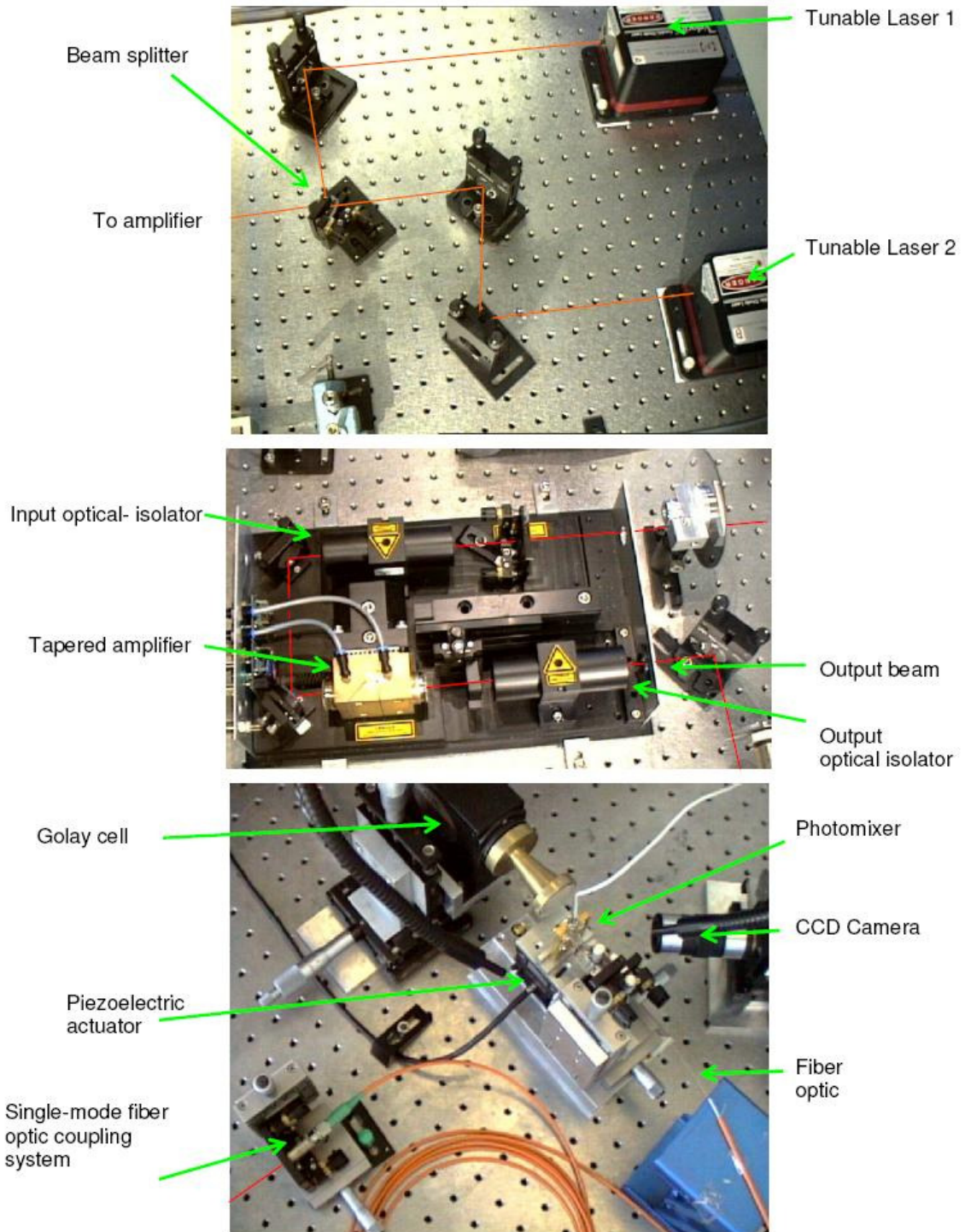


**Fig. 4.3:** Pictures of the two semiconductor tunable lasers (up), amplifier (middle) and fiber positioning stage with the Golay cell detector (down)).

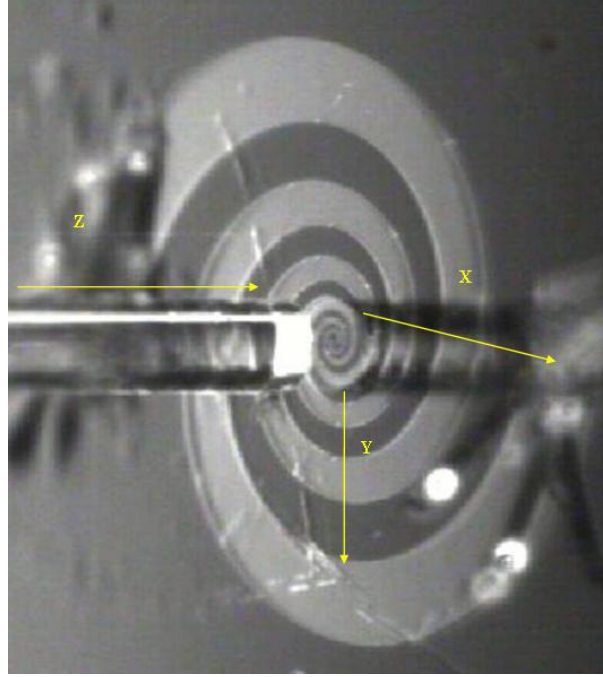


**Fig. 4.4:** Snapshot of the CCD camera. A photomixer with integrated logarithmic spiral antenna is illuminated by a single-mode fiber optic. The specular image of the fiber optic can be seen to the right.

The laser power illuminating the photomixer was absorbed mostly either in the photoactive volume or in the underlying substrate. Nevertheless a non-negligible amount of power (tens of nanowatts for typical illumination conditions) crossed the whole substrate entering the input window of the Golay cell together with the terahertz radiation giving rise to a background signal. In order to avoid this, an NIR filter was placed at the aperture of the Winston cone. Last but not least, for high photocurrents in the photomixer, the heating power of the mixer can reach several hundreds of milliwatts, rising the local temperature of the photoactive region up to 400 K [44]. At these temperatures the blackbody radiation of the photomixer accounts for a further noise contribution –tens of nanowatts typically– to the signal detected by the Golay cell. To get an insight into the order of magnitude of black-body radiation, according to the Stefan-Boltzmann law the energy flux density (energy radiated per unit area per unit time) is:

$$J_u = \sigma T^4 \quad (4.1)$$

with  $\sigma = 5.6710^{-8} \text{Wm}^{-2}\text{K}^{-4}$  being the Stefan-Boltzmann constant. Consequently, the net radiated power is:

$$P = e\sigma A_{\text{photomixer}}(T_{\text{blackbody}}^4 - T_{\text{amb}}^4) \quad (4.2)$$

with  $e$  being the emissivity of the blackbody ( $e=1$  for a perfect blackbody). If we model the photomixer as a perfect blackbody with  $100 \mu\text{m}^2$  active area at a constant temperature of 400 K embedded in a substrate at constant

temperature ( $T_{amb} = 300\text{ K}$ ) we get:  $P \approx 100\text{ nW}$  with an emissivity peak at a wavelength given by Wien's displacement law,  $\lambda_{max} = 2.89 \cdot 10^6 / T = 7.2\ \mu\text{m} \equiv 41.2\ \text{THz}$ , which lies well within the absorption range of the Golay cell. The contribution of this blackbody radiation is of the same order of magnitude as the proper coherent THz radiation from photomixing and must be considered as an additional background noise. Due to the small dimensions of the photomixer, the time constant associated to the heating of the active region is far below –microsecond range– the laser chopping time of 50 milliseconds. Therefore the variations of the photomixer temperature are expected to be modulated nearly with a 100 % modulation efficiency, according to the chopped laser power and consequently the contribution of the blackbody radiation cannot be electrically filtered in the lock-in amplifier. One way to get rid of this contribution is by installing low-pass THz filters. In this work, no filters were included in the detection setup. The reason is that the power contribution of the blackbody radiation can be readily measured and be subtracted from the total power. This was performed by blocking one laser (no photomixing process taking place) and increasing the laser power of the unblocked laser until it achieves the same power as when both laser were unblocked. The power measured by the Golay cell is actually that due to blackbody radiation plus the contribution of the laser power which is not absorbed in the photomixer.

The measurement setup was installed on an optical table with an air-damping based vibration isolation system. The lasers, DC power supply for the photomixer, precision ampere-meter, piezoelectric actuator, lock-in amplifier and optical spectrum analyzer were computer-controlled via GPIB allowing automatized data acquisition. Programmes written in Lab-view enabled to perform different measurements to characterize photomixers.

In order to perform low-temperature measurements, a cryostat was available with a closed-cycle cooling machine. This allowed cooling the devices down to temperatures as low as  $30\text{ K}$ . We installed the pig-tailed photomixers on the Dewar cold finger and the THz radiation was coupled out through a Teflon window.

### 4.3 The Photomixing device

In this work, small-area Metal-Semiconductor-Metal (MSM) photomixers with both integrated resonant and broadband antennas were used. The photomixing area was patterned at the feed point of a resonant or broadband antenna, so that the beat signal was radiated into free space. The high dielectric constant of the GaAs photomixer lens substrate ( $\epsilon_r=12.8$ ) prevented the signal from being radiated backwards to the fiber optic. The hyperhemispherical form of the substrate suppressed surface modes and provided acceptable beam directivity [45], [46] – see section 4.3.2.

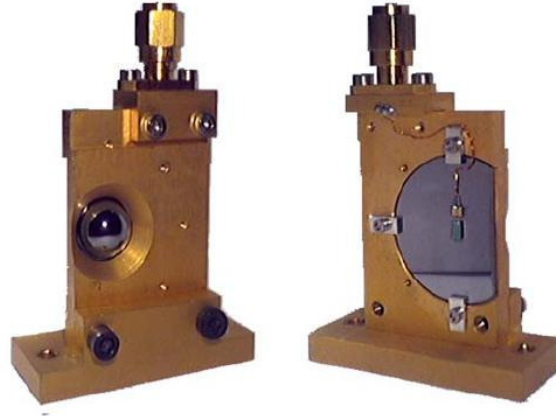


**Fig. 4.5:** Photograph of a photomixer chip glued on a HR silicon substrate with hyperhemispherical form. The bond pads and wires for the DC bias can be seen.

As seen in figure 4.5, a diced substrate with the photomixer, antenna and bond pads was glued on a high resistivity silicon substrate lens which was clamped on a brass holder. For electrical connection, the photomixer was bonded with gold wires to the bond pads, which in turn were soldered to the DC bias cables coming from an SMA connector.

### 4.3.1 The MSM structure

The MSM element consisted of a biased interdigitated finger structure with a typical area of  $8\mu\text{m} \times 8\mu\text{m}$ . The finger width was 200 nm and the gap between fingers varied from 500 nm to  $2\mu\text{m}$ . Chapter 5 presents measurements and optimization of the finger structure parameters.

There are two problems directly associated with the MSM structure: the capacity (typically  $1 - 3fF$  for the used MSM designs), which shorts-out the photomixer at high frequencies and the inhomogeneity of the electric field distribution across the semiconductor.

#### Capacity of the interdigitated structure

A theoretical expression for the interdigitated capacity based on conformal mapping techniques is available [47]:

$$C = \frac{\epsilon_0(1 + \epsilon_r) \cdot A}{2 \cdot (l_e + l_g)} \cdot \frac{K(k)}{K(k')} \quad (4.3)$$

with  $K$  being the Legendre's complete elliptical integral of the first kind

$$K(k) = \int_0^{\pi/2} \frac{1}{\sqrt{1 - k^2 \cdot \sin^2 \phi}} d\phi \quad k = \tan^2 \frac{\pi \cdot l_e}{4(l_e + l_g)}$$

where  $\epsilon_0$  and  $\epsilon_r$  are the vacuum electric permittivity and the substrate relative permittivity,  $A$  is the active area,  $l_e$  and  $l_g$  are the electrode width and gap respectively,  $k = \tan^2 \frac{\pi l_e}{4(l_e + l_g)}$  and  $k'$  its complementary modulus  $k' = \sqrt{1 - k^2}$ . By using the fact:

$$\frac{K(k)}{K(k')} \approx \frac{\pi}{\ln[2(1 + \sqrt{k'})/(1 - \sqrt{k'})]} \quad \text{for } 0 \leq k \leq 1/\sqrt{2} \quad (4.4)$$

for  $L_e < L_g$  we get:

$$C \approx \frac{\pi(1 + \epsilon)\epsilon_0 A}{2(l_e + l_g) \ln[2(1 + \sqrt{k'})/(1\sqrt{k'})]} \quad (4.5)$$

Note that formula 4.5 treats the semiconductor as a perfect dielectric. As will be shown in the next section, the formation of space-charge regions in the semiconductor-metal junction has a critical contribution to the overall capacity of the MSM structure. In addition, at high frequencies the MSM structure is no longer electrically small and the above mentioned lumped element approximation does not hold. For this situation, a Method of Moments simulator accounting for the finite MSM structure dimensions yields more accurate results. The capacity presented by the finger structure shorts-out the photomixer at high frequencies and lowers the resonance frequency for resonant dipole antenna designs. As mentioned in section 2.5, an inductive shunt element can be used to address this problem. In general, the capacity problem becomes more unmanageable at higher frequencies. For the mentioned reasons, formula 4.5 gives only a rough estimation of the MSM capacity.

### Build-up of space-charge regions

When a metal and a semiconductor are brought together, a transfer of charge occurs until the Fermi levels of semiconductor and metal are equal. Since the work functions of semiconductor and metal are usually different, free carriers move in the interface region in order to minimize their potential energy. As a consequence space-charge regions – band bending – are formed at the semiconductor side of the metallurgic junction. In the case of a n-type semiconductor if the metal's work function is larger than that of the semiconductor,  $\phi_M > \phi_S$ , the junction displays a rectifying behavior – the same holds for p-type semiconductor if  $\phi_M < \phi_S$ .

The rectifying properties arise due to the formation of a potential barrier which blocks the transit of majority carriers in a certain direction (electrons

in the metal to semiconductor direction for n-type semiconductors or holes in the case of p-type semiconductors). In case of  $\phi_M < \phi_S$  or  $\phi_M > \phi_S$  for n-type or p-type semiconductors respectively, no potential barriers are formed and the carriers can move freely in either direction: the contact behaves like a resistance. Under these circumstances the contact is called ohmic.

The type of contact plays a major role in the distribution of the electric field within the semiconductor. The doping properties of the materials used for photomixing – LT GaAs and ion-implanted GaAs – are similar to those of SI GaAs, which is slightly n-doped [48].

For the sake of simplicity let us first ignore the role of traps. We shall consider a Schottky contact between semiconductor and metal. As depicted in figure 4.6, a potential barrier is formed at the interface. Its value can be calculated as  $\Phi_{Barrier-semicond} = \phi_M - \phi_S$  on the semiconductor side and  $\Phi_{Barrier-metal} = (\phi_M - \phi_S) + (\phi_S - \chi_S) = \phi_M - \chi_S$  on the metal side. As can be seen, a net positive space-charge region is formed at the interface.

If the semiconductor traps are considered, the physics of metal-semiconductor junction presents interesting properties which can lead to significant changes in the electric field distribution and the space-charge regions (see figure 4.7). A complete analysis accounting for the effects of the multiple type of traps in LT-GaAs and ion-implanted GaAs is beyond the scope of this work, therefore a very simple model to yield qualitative results is presented. We shall first consider donors-like traps in a deep level sub-band,  $E_c - 0.75\text{eV}$  [49], slightly below the Fermi level associated to the  $As_{Ga}$  defect. A sub-band of acceptors accounts for partial compensation of the donors. The dominant acceptors are associated to the  $V_{Ga}$  defect and are situated 0.28 eV [50] above the valence band. Typical concentrations are  $10^{17} - 10^{18}\text{cm}^{-3}$  and  $10^{18} - 10^{20}\text{cm}^{-3}$  [51] for acceptors and donors, respectively.

The occupancy probability of these traps can be calculated using the approach of Simmons and Taylor [52] as:

$$F_n = \frac{v_n \sigma_n + e_p}{v_n \sigma_n + v_p \sigma_p + e_n + e_p} \quad (4.6)$$

for donor-like traps and

$$F_p = \frac{v_p \sigma_p + e_n}{v_n \sigma_n + v_p \sigma_p + e_n + e_p} \quad (4.7)$$

with  $\sigma_n$  and  $\sigma_p$  being the capture cross sections for electrons and holes,  $v_n$ ,  $v_p$ ,  $e_n$  and  $e_p$  the thermal velocities and emission rates for electrons and holes, respectively. The emission rates can be calculated from the energy level of the corresponding trap as:

$$e_n = g_d v_n \sigma_n n_i \exp\left(\frac{E_d - E_i}{KT}\right) \quad (4.8)$$

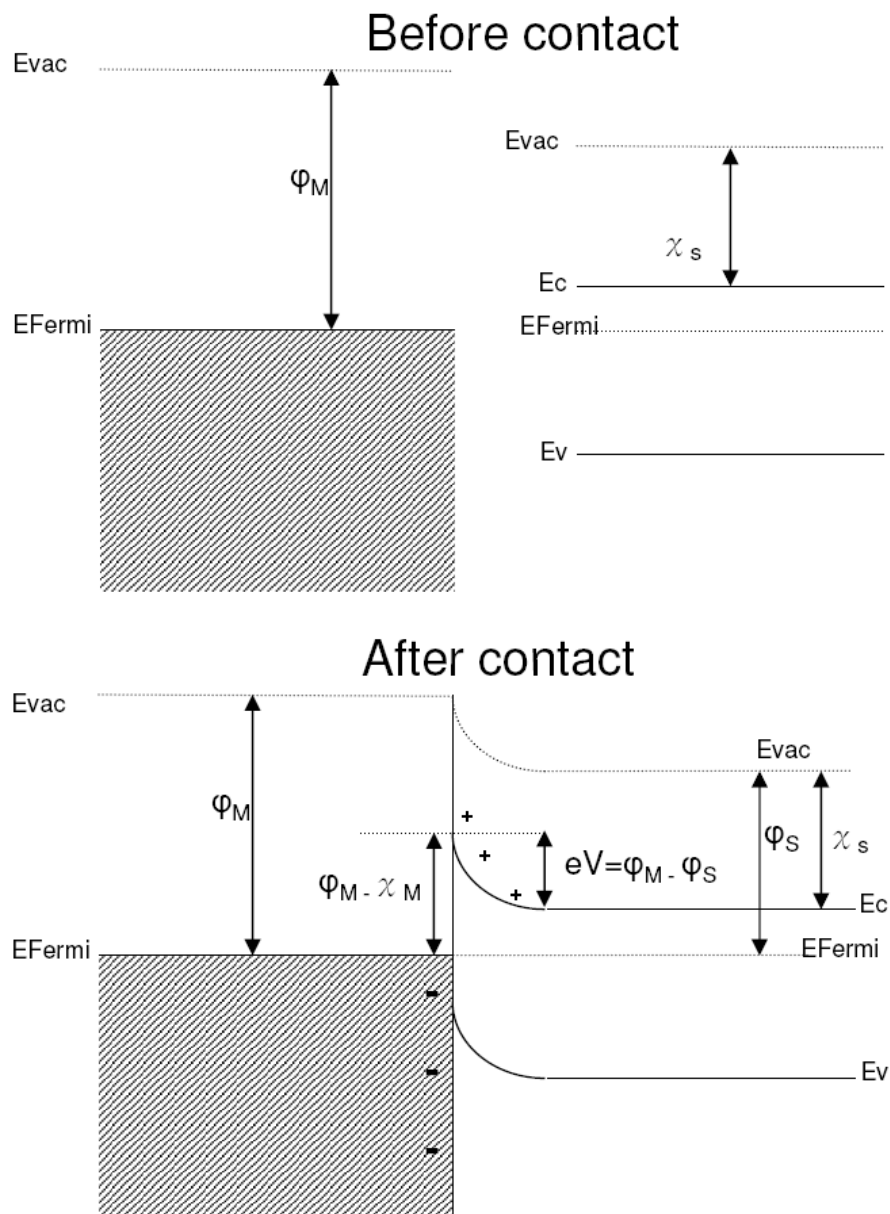


**Fig. 4.6:** (left) Energy diagrams of a metal and a n-type semiconductor before contact (the work function of the metal,  $\phi_M$ , is larger than that of the semiconductor,  $\phi_S$ ). (right) A Schottky contact is formed in the metal-semiconductor junction.

and

$$e_p = g_a v_p \sigma_p n_i \exp\left(\frac{E_i - E_a}{kT}\right) \quad (4.9)$$

where  $g_d$  and  $g_a$  are for the degeneracy factors,  $n_i$  and  $E_i$  for the intrinsic carrier concentration and intrinsic energy level.

Under thermal equilibrium conditions, the Simmons and Taylor formulas reduce to Fermi-Dirac statistics, whereby the Fermi energy  $E_f$  can be calculated by imposing global charge neutrality. The concentrations of ionized defects are given by

$$N_d^+ = \frac{N_d}{1 + g_d e^{(E_f - E_d)/kT}} \quad N_a^- = \frac{N_a}{1 + g_a e^{(E_a - E_f)/kT}} \quad (4.10)$$

where  $N_d^{(+)}$  and  $N_a^{(-)}$  are the (ionized) donor and acceptor concentration,  $g_d$  and  $g_a$  are the corresponding degeneracy factors. The energy levels of acceptor and donor bands are  $E_d$  and  $E_a$ .

According to equations 4.10, most of the acceptors will be ionized at room temperature,  $E_f - E_a \gg kT$ . This holds even for regions in which band bending occurs, i. e., next to the metal-semiconductor interface. In contrast to this, donor-like traps cannot be fully ionized. Their degree of ionization will be sensitive to variations of  $E_d$  ( $E_d \gtrsim E_f$ ) and therefore the trap occupancy will be considerably different in regions with band bending than in the bulk.

The net charge can be calculated as  $N_{net} = N_d^+ - N_a^- - n + p$ . Due to the negligibly small intrinsic carrier concentration,  $n_i \sim 10^7 \text{ cm}^{-3}$ , the net charge will be determined by the defects, i. e.  $N_{net} = N_d^+ - N_a^-$ . Since global charge neutrality must hold, in the bulk semiconductor  $N_{net} = N_d^+ - N_a^- = 0 \Rightarrow N_d^+ = N_a^-$ . This means that despite the larger donor-like traps concentration, the total concentration of ionized donors is not larger than that of ionized acceptors. The reason is that the energetic proximity of the donor band energy to the Fermi level results in a smaller ionization percentage ( $< 10\%$  [35]) than for the acceptor impurities ( $\sim 100\%$ ).

In regions next to the metal-semiconductor interface, the charge neutrality condition can be locally violated ( $N_d^+ \neq N_a^-$ ) on length scales less than the Debye length. As stated before, the ionization of donor-like traps is the one sensitive to band bending and therefore determines mainly the physics of space-charge formation. In these regions, the band bending shifts the energy of both donor and acceptors bands upwards relative to the Fermi level, changing the occupancy of donor-like traps (see figure 4.7). In thermal equilibrium with no applied bias voltage, the energy of the Fermi level is unaltered across the junction, therefore the percentage of ionized donors increases as they get closer to the interface. In contrast, the concentration of ionized acceptors, almost 100%, is practically position-independent and is able to compensate ionized donors in the bulk. Nevertheless, at



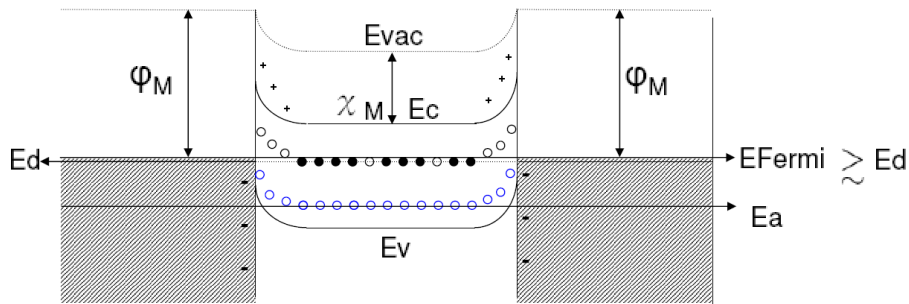


**Fig. 4.7:** Energy diagrams of a metal - GaAs - metal Schottky contact. A deep donor band (black circles) situated slightly above the Fermi level is partially compensated by an acceptor band (blue circles). Defects are represented with solid color when not ionized. The relative concentration of both defects does not have any relation with the number of circles.

the interface regions ionized acceptors are not able to compensate the increasingly larger concentration of ionized donors. As a consequence, the uncompensated ionized donors result in net positive space-charge regions (see figure 4.7).

If a bias voltage is applied to the metal, the situation gets more complicated. A priori one can expect that the formation of space-charge regions at the anode and cathode display different properties. Current transport is due mainly to conduction electrons [53], therefore ambipolar conduction effects will be neglected. Under this assumption, the situation can be qualitatively described as follows: Electrons drifting to the anode are trapped and increase locally the occupancy of donor-like traps, thereby balancing the charge compensation in the opposite direction than in the case without bias voltage. As a consequence, the Schottky barrier at the anode diminishes –the presence of additional trapped negative charge "bends" the bands back. In case of sufficient concentration of trapped electrons next to the anode, the space-charge region can eventually develop into a net-negative space-charge region. In contrast, the cathode experiences a small electron depletion. For semi-insulating GaAs this depletion is small [54]: as electrons escape out of the cathode space-charge region, new electrons are injected from the metal. The injection of electrons is rather efficient due to the sufficiently low Schottky barrier. As a result, the space-charge region at the cathode decreases.

In general, the distribution of electrostatic potential and space-charge regions across the MSM structure are strongly dependent on the concentrations of donor and acceptors, carrier lifetime of holes and electrons and illumination conditions. The variations of the electrostatic potential across an MSM structure on semi-insulating GaAs has been experimentally observed [54]. After Grischkowsky, the potential drops rapidly next to the anode. Responsible for this mechanism, – called trap-enhanced-fields (TEF)

– is the above mentioned accumulation of electrons in electron traps near the anode which cannot be compensated by the ionized acceptors. Ibbetson et al. reported on the determining role of traps to understand the I-V characteristics in non-stoichiometric GaAs [53]. Nevertheless, a qualitative extrapolation of these results (semi-insulating GaAs) to LT GaAs is not justified. The differences in concentration of defects and trapping times between both materials makes a detailed analysis essential in order to extract relevant conclusions.

Several experiments with multilayered structures demonstrate both depletion of electrons [55], [56] or accumulation [56] in LT-GaAs, depending on the layer design and type of doping in the neighboring layers. For example, in the interesting work of Brunkov [56], experiments were reported with a 100 nm thick LT-GaAs layer sandwiched between two heavily doped layers, –i. e.  $n^+GaAs - LTGaAs - n^+GaAs$  and  $p^+GaAs - LTGaAs - p^+GaAs$ . From capacitance-voltage (C-V) measurements the concentration of the majority carriers accumulated in the LT-GaAs layer was determined. When a reverse voltage was applied in order to deplete the LT-GaAs layer from the accumulated carriers, the rate of hole emission was much lower than that of electrons. Using Kelvin probe force microscopy (KFM) the surface potential of a MESFET LT GaAs cap layer has been measured [57]. In conclusion, large drops of potential and high electric fields across thin sandwiched defect-rich GaAs layers have been observed.

### Simulations of the photomixing device

Since our laboratory equipment did not include any instrumentation to image the potential distribution as electric force microscopy (EFM) or surface potential (SP) imaging, a commercial semiconductor simulator was used to analyze the build-up of space-charge regions next to the electrodes. Prior to simulating the LT-GaAs or ion-implanted photomixer structures, the software was tested by comparing its results with published data. Phenomena as trap-enhanced-fields (TEF) [54] in SI-GaAs and depletion [55] or accumulation [56] of electrons in LT-GaAs were satisfactorily predicted.

A two-dimensional simulation of the photomixing device was performed with the commercial software ATLAS (Silvaco Data Systems Inc.). The simulation allowed to solve self-consistently the current density and the continuity equations as well as the Poisson equations from section 2.4 for the two- and three-dimensional cases. A field-dependent mobility model was included to account for velocity saturation. In order to model the recombination dynamics via deep donor traps, the Shockley-Read-Hall model was integrated. The parameters of crystalline GaAs, which are included in the simulator material database, were modified to model LT-GaAs/implanted-GaAs as shown in table 4.1. With the present simulation it was not intended to perform an accurate device modeling but rather to shed some light into some of the MSM structure physics, especially those

Parameter	Value
Electron mobility	$400\text{cm}^2/\text{Vs}$ [58]
Hole mobility	$100\text{cm}^2/\text{Vs}$ [58]
Electron saturation velocity	$4 \cdot 10^6\text{cm/s}$ [58]
Hole saturation velocity	$1 \cdot 10^6\text{cm/s}$ [58]
Concentration of donor-like traps	$10^{18}\text{cm}^{-3}$ and $10^{19}\text{cm}^{-3}$ [51]
Energy level of donor-like traps	$0.75\text{eV}$ below conduction band [49]
Electron lifetime in donor-like traps	200 femtoseconds [58]
Electron lifetime in donor-like traps	700 femtoseconds [59]
Concentration of acceptor-like traps	$10^{18}\text{cm}^{-3}$ and $10^{17}\text{cm}^{-3}$ [51]
Energy level of acceptor-like traps	$0.28\text{eV}$ above valence band [50]

**Tab. 4.1:** Parameters chosen for the simulation of the MSM structure

concerning the electric field distribution, carrier transport and recombination dynamics.

The definition of the electrodes work function was necessary to account for the Schottky barrier which is formed in the metal-semiconductor interface, otherwise this contact would be treated as ohmic by the simulator. Very often the experimental value for the Schottky barrier differs considerably from the theoretical one. The microscopic structure of the metal-semiconductor interface plays a determining role – surface defects, interfacial layers due to chemical reactions between metal and semiconductor, surface oxidation in the semiconductor prior to metal deposition, etc. For this reason an intentionally larger value for the work function of the titanium electrode was defined (4.87 eV instead of 4.35 eV), so that the simulator calculation yielded a more realistic value for the Schottky barrier height (0.8 eV) [60].

It is important to remark that as reported by Yamamoto et al. [60], the main carrier transport mechanism in the semiconductor-metal interface for non-stoichiometric GaAs is via tunnel emission from the metal to the donor band and vice-versa. This transport process is much more efficient than that of conduction-band electrons. The reason lies in the reduced potential barrier that trapped electrons (0.15 eV) have to overcome – in comparison to the Schottky barrier (0.8 eV) for conduction band electrons. This explains the remarkably low contact resistances ( $10^{-3}\Omega\text{cm}^2$ ) found in LT-GaAs. The specific contact resistance is therefore mainly determined by the defect concentration of the LT-GaAs/implanted-GaAs being of secondary importance the contact electrode material. Unfortunately, this model of transport could not be incorporated into the simulations. In any case, the effect of tunnel contacts via traps is to reduce the contact resistance resulting in almost Ohmic contacts. For this reason, the Ohmic contact case as well as the Schottky contact case were simulated to study their relevant differences.

In order to model the ultrafast trapping centers –  $A_{\text{S}_{\text{Ga}}}$  antisites – a donor-

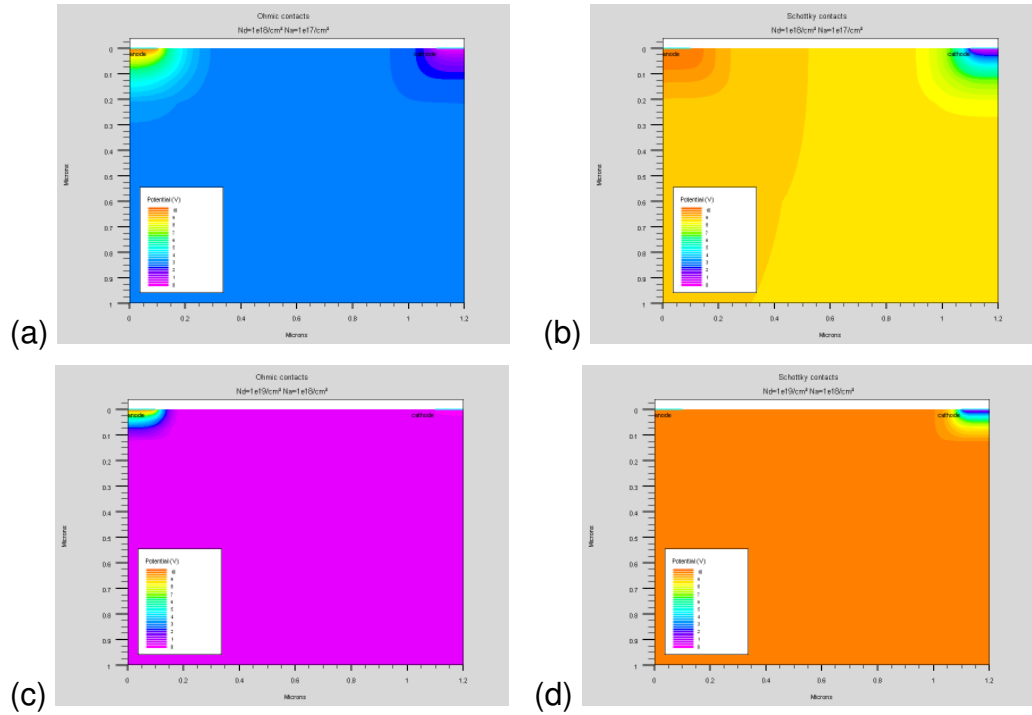


**Fig. 4.8:** Electrostatic potential distribution for different metal-semiconductor contact conditions and defect concentrations. The applied bias voltage was 10 volts without illumination. The top graphs were simulated for a donor density  $N_d = 10^{18} \text{cm}^{-3}$  and an acceptor density  $N_a = 10^{17} \text{cm}^{-3}$ . The bottom graphs were simulated for a donor density  $N_d = 10^{19} \text{cm}^{-3}$  and an acceptor density  $N_a = 10^{18} \text{cm}^{-3}$ . The graphs to the left were simulated with ohmic contacts whereas the graphs to the right were simulated with Schottky contacts.

like trap subband was defined as well as acceptor shallow band – i. e.,  $V_{Ga}$  vacancies. The actual concentration, energetic position of the bands and other relevant parameters – see table 4.1 – were chosen from the literature.

First of all, the case of no illumination was analyzed for different contact designs and a bias voltage of 10 volts. The donor and acceptor concentration were set to the values  $N_d = 10^{18} \text{cm}^{-3}$ ,  $N_d = 10^{19} \text{cm}^{-3}$  and  $N_a = 10^{17} \text{cm}^{-3}$ ,  $N_a = 10^{18} \text{cm}^{-3}$ . The applied voltage was 10 volts. By inspecting figure 4.8, a rapid drop of the potential next to the electrodes is found.

Interestingly, depending on the type of contact, the potential drop takes place close to the anode – ohmic case, figure 4.8 (a) – or next to the cathode (b)– Schottky contact case. In general, structures with a larger defect concentration exhibit a stronger confinement of the potential drop – compare figure 4.8(a) with (c) and figure 4.8(b) with (d). These differences can be understood using the full depletion approximation and will be discussed later.

As a consequence of the abrupt potential drop, large electric fields of the

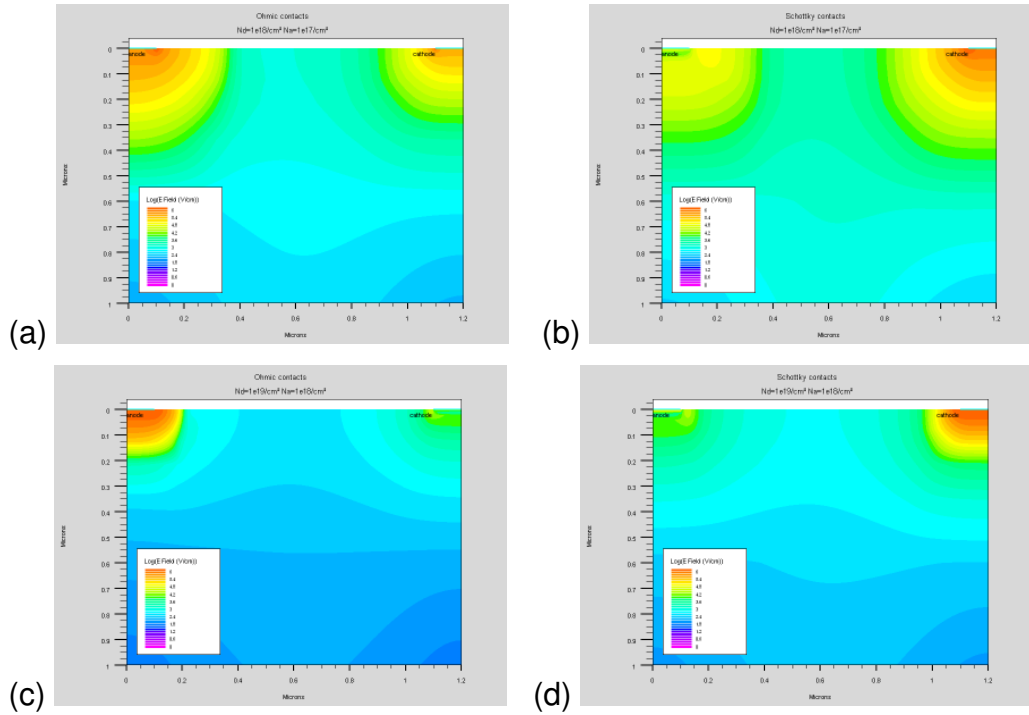


**Fig. 4.9:** Same as figure 4.8 illustrating the electric field distribution. Due to the large dynamic range of the  $E$ -field, a logarithmic scale has been chosen. Next to the electrodes, regions with electric fields up to  $10^6 V/cm$  build up.

order of  $10^6 Vcm^{-1}$  build up – see figure 4.9. These electric fields vanish abruptly both toward the bulk and toward the counterpart electrode. The presence of high electric fields next to the electrodes might trigger electromigration processes, causing irreversible damage in the photomixer. Furthermore, impact ionization, band-to-band and trap-assisted tunneling processes might occur. Note that at these large electric fields the lowering of the Schottky barrier due to image-charges begins to gain importance. As an example, for the electric fields obtained in the simulation, the Schottky barrier and dipole lowering can be calculated according to the expression:  $\Delta\phi_B = \sqrt{\frac{qE_{max}}{4\pi\epsilon}} + \alpha E_{max}$ , where  $E_{max}$  is the electric field at the interface and the parameter  $\alpha$  is 4 nm [61]. For  $E_{max} = 10^6 Vcm^{-1}$  the expression yields  $\Delta\phi_B = 500mV$ .

The reason for the observed differences depending on the type of electrode configuration lies again in the accumulation or depletion of electrons.

The simulation results with ohmic contacts are in agreement with the phenomena exposed in section 4.3.1: electrons are accumulated in the electron traps close to the anode. The concentration of ionized donors diminishes, so that ionized acceptors cannot be compensated anymore. This leads to the built-up of a net negative space-charge region at sufficiently high bias voltage. Since the contacts are ohmic, in general, the cathode suffers a small depletion of electrons: as electrons drift out of the region

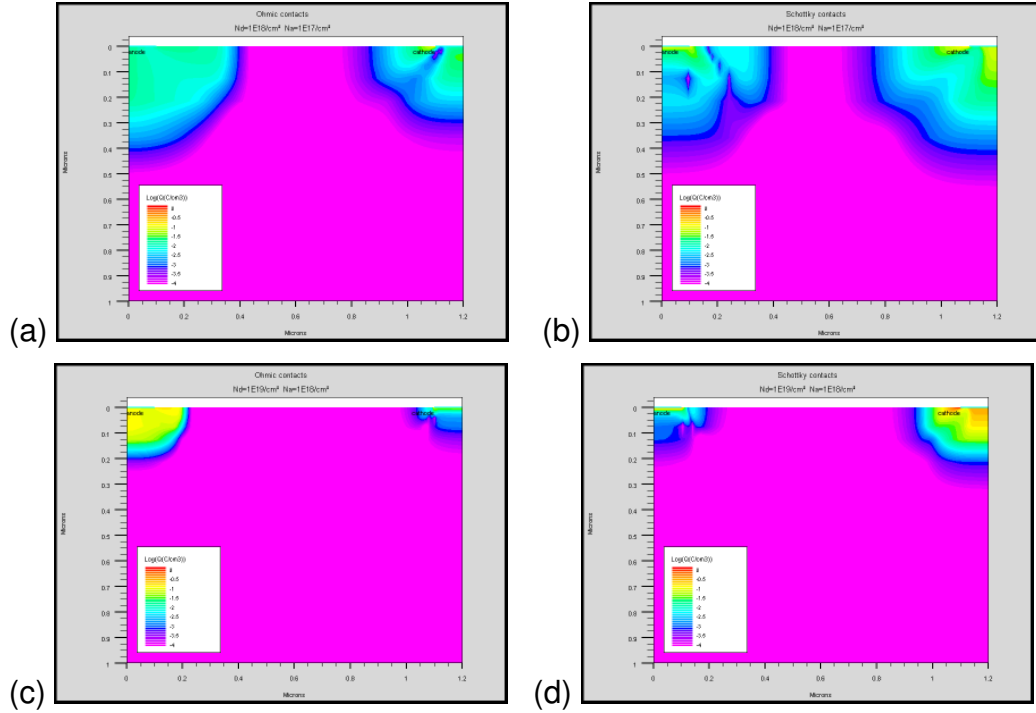


**Fig. 4.10:** Same as figure 4.8 illustrating charge density. Note that due to the logarithmic scale the sign of charge could not be represented. Negative charges are located adjacent to the anode and the positive ones next to the cathode. Fine structures arising from the extreme band bending next to the electrodes can be observed.

adjacent to the cathode, new electrons from the metal are injected. The mentioned space-charge formation due to the accumulation of electrons next to the anode is more evident at higher defect concentration. This can be seen comparing figures 4.10(a) and (c). This negative charge accumulation – up to  $0.01C/cm^3$  and  $0.1C/cm^3$  for figures 4.10(a) and (c) respectively – is in the form of trapped charge and results in a drastic reduction of the ionized donors concentration. Note that the value of charge accumulation next to the anode is approximately  $N_a^- \simeq N_a$  since almost all donors are neutral and therefore the electrical properties are determined by the acceptor concentration. These simulation results are shown in figures 4.11(a) and (c).

At a first glance, the abrupt voltage drop next to the electrode and the consequent extreme electric fields predicted by the simulation might seem unrealistic. At this point we are able to understand qualitatively these results using the full depletion approximation. It states that for a biased metal-semiconductor junction, the length of the space-charge region equals:

$$x_d = \sqrt{\frac{2\epsilon(\phi_B - eV_a)}{e^2 N_{ionized}}} \quad (4.11)$$

where  $\epsilon$  is the dielectric constant,  $\phi_B$  the Schottky barrier seen by the semiconductor towards the metal ( $\phi_B = \phi_M - \phi_S$ ) and  $V_a$  is the potential drop

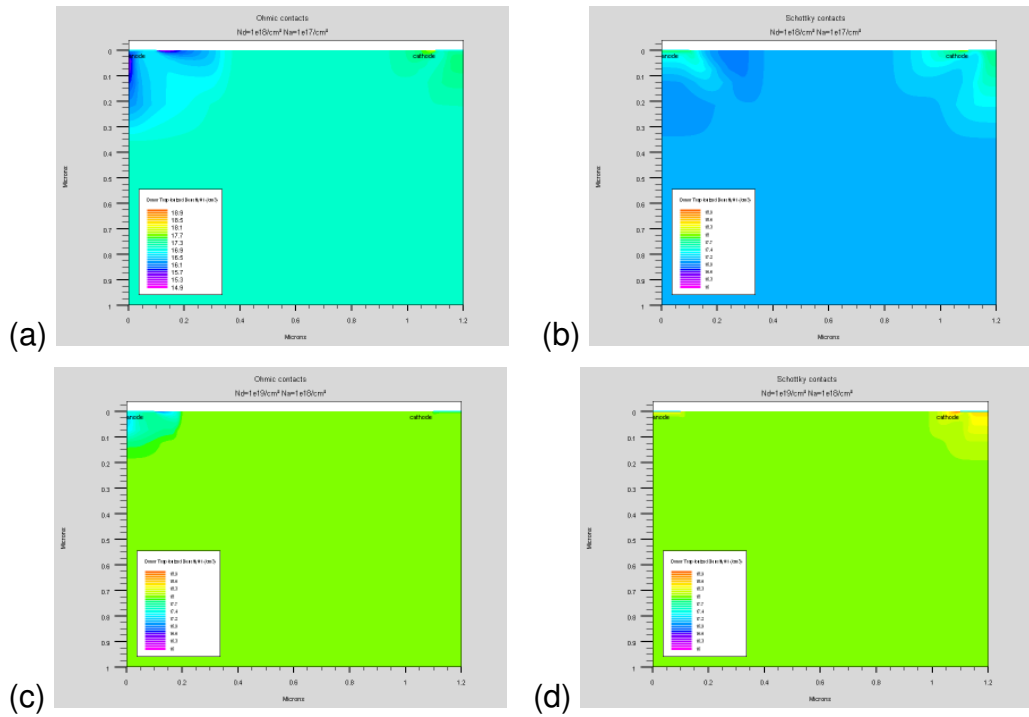


**Fig. 4.11:** Same as figure 4.8 illustrating the ionized donor density.

across the junction considered due to the external bias voltage.  $N_{ionized}$  is the net ionized charge, which can originate from donors or acceptors; in the present case it represents approximately the ionized acceptors next to the anode,  $N_{ionized} = |N_d^+ - N_a^-| \simeq N_a^-$ . Substituting in equation 4.11 yields  $x_d \approx 380nm$  (for  $N_a = 10^{17}cm^{-3}$ ) and  $x_d \approx 120nm$  ( $N_a = 10^{18}cm^{-3}$ ), which matches quite well with the simulation results of figures 4.10(a) and (c).

The case of Schottky contacts from figure 4.8(b) deserves some attention. First let us consider that the MSM structure is suddenly biased. In addition let us assume that before steady-state establishes the electric field between electrodes is roughly constant. The only space-charges result from the available Schottky contacts. Under these circumstances, electrons drifting toward the anode accumulate there and diminish band bending from the Schottky barrier similarly to the case of ohmic contacts. As electrons leave the region adjacent to the cathode, new electrons must be injected from the cathode. Nevertheless, in contrast to the ohmic case, the injected electrons from the metal must overcome a Schottky barrier. This barrier height,  $\Phi_{Barrier-metal} = \phi_M - \chi_S$  is practically unaltered<sup>3</sup> by the bias voltage and induces in the non-stationary situation that more electrons escape from the region adjacent to the cathode than electrons are injected from the metal. As a result, the region experiences a depletion of electrons. Consequently, the band bending in the cathode Schottky contact becomes more pronounced. In the stationary state the integral of the cur-

<sup>3</sup>ignoring barrier lowering by image charges.

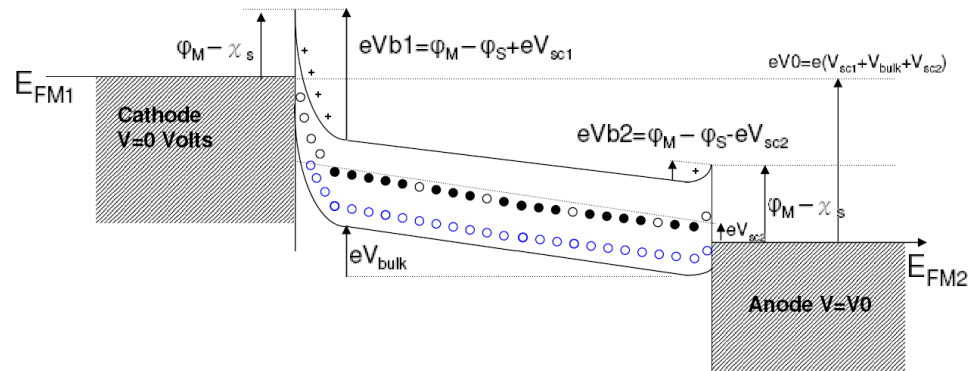


**Fig. 4.12:** Energy diagrams of a biased metal – non-stoichiometric GaAs – metal structure with Schottky contacts. The potential drops in three regions: cathode space-charge region  $V_{sc1}$ , bulk  $V_{bulk}$  and anode space-charge region  $V_{sc2}$ . The relative potential drop within these regions is not represented at scale since it depends on the actual defects concentration and metal properties. The lowering of the space-charge region in the anode is due to the applied bias voltage and due to the ionized acceptors, which cannot be compensated by donors. Electrons drifting toward the anode get trapped by empty donors, thereby reducing the concentration of ionized donors which are to compensate the fully ionized acceptors. The space-charge region at the cathode builds up due to a depletion of electrons.

rent density at the anode must be equal to that at the cathode – otherwise an increasing charge depletion/ accumulation would occur. As already stated, the barrier at the anode diminishes as the electron concentration, i. e., electron current density, increases. All these conditions imply that the main voltage drop must take place in the region adjacent to the cathode. Only so the integral of the current density at the cathode can be equal to that at the anode. The situation is analogous to that of two diodes connected in series. The diode next to the anode is forward biased whereas the other one is placed next to cathode and reversed biased. Clearly the potential drops on the reversed biased diode, i. e. the one placed next to the cathode.

Figure 4.12 illustrates the energy band diagram for a generic Schottky contact MSM structure showing space-charge regions next to anode and cathode. Note that a realistic contact would be almost ohmic due to the mentioned tunneling process to/ from the donor band.

In conclusion, the large gradient of the potential next to the electrodes is due to the large defect concentration in the semiconductor. Of course, this space charge modifies the capacitance of the MSM structure. Hence, the calculations of capacity, which use conformal-mapping techniques like those presented in section 4.3.1, give inaccurate results since they treat the semiconductor as a perfect dielectric and ignore the crucial role of space-charges. This is explicitly observed in figure 4.13, where the ca-



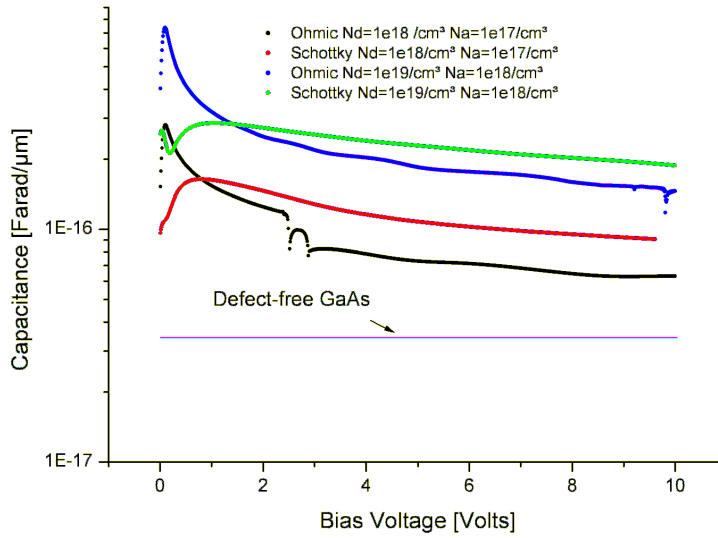


**Fig. 4.13:** Quasi-static capacitance simulation of MSM structures with ohmic and Schottky contacts at different defect concentrations. The fine structures results from large variations of electrode charge with voltage – Recall that the quasi-static capacity is calculated as  $C = \frac{dQ}{dV}$ . Similar structures in C-V curves have been observed in real measurements [56].

capacitance for Schottky and ohmic contacts is compared at different defect concentrations. The case of pure crystalline GaAs is shown as well. At larger defect concentrations the characteristic length of the space-charge region diminishes, thereby increasing the capacitance. Comparing these results with those from the full depletion approximation we get for the capacity per micrometer:

$$C/\mu m = \epsilon_0 \epsilon_r \frac{100 \cdot 10^{-9} 10^{-6}}{x_d} F/\mu m \quad (4.12)$$

(note that the electrode cross section was 100 nanometers). Substituting  $x_d$  for both defect concentrations ( $x_d = 380nm$  and  $x_d = 120nm$ ) yields  $\approx 3 \cdot 10^{-17} F/\mu m$  and  $\approx 10^{-16} F/\mu m$  which is roughly the half of the values from the simulation. The inaccuracy is due to the border effects: the dimensions of the space-charge region should be much less than those of the electrode in order to determine the capacity with a parallel-plate approximation. In any case, the calculated values give an excellent estimate for the order of magnitude at which the capacitance is expected.

When the sample is illuminated (with typical irradiances  $\sim 1mW/\mu m^2$ ), the space-charge region builds up only in the region adjacent to the cathode, regardless of type of contact and defect concentration. Responsible for this effect is the optical injection of carriers in the space-charge regions. For the irradiances used in this work,  $I = 1mW/\mu m^2$ , supposing a reflection

coefficient of 30% at the air-GaAs interface, the average photoelectron concentration in the first micrometer below the surface is:

$$n_{opt} = \frac{I}{h\nu} \tau_{trapping} = \frac{10^{-3} \cdot 0.7 \cdot 200 \cdot 10^{-15}}{10^{-12} h\nu} = 5.5 \cdot 10^{14} \text{cm}^{-3} \quad (4.13)$$

Note that the excess photogenerated charge is several orders of magnitude larger than the free carrier density of the unilluminated MSM structure ( $\sim 10^6 \text{cm}^{-3}$ ). Therefore, the optically injected carriers will determine the electrostatic properties of the MSM structure. Due to the electrode dimensions ( $\sim 100 \text{nm}$ ) relative to the optical wavelength ( $\sim 780 \text{nm}$ ), diffraction will enable illumination of regions underneath the electrodes. It is important to remark that in order to observe saturation of traps, the concentration of photoelectrons should be comparable to that of ionized donors, which is not the case. Investigations on LT GaAs layers report on trap saturation [62] effects under illumination with femtosecond-lasers. The irradiance required for trap saturation effects to occur is around three orders of magnitude larger than that used in the present work. Furthermore, such irradiances would destroy the photomixer in case of CW operation.

The drop of potential next to the cathode for both contact types is caused by the depletion of electrodes in the regions adjacent to the cathode. Of course, accumulation of electrons takes place in the region close to the anode as well, nevertheless, from both competing processes the former one determines the built-up of charge. The reason lies in the fact that as an electron-hole plasma is generated by the impinging light, the higher mobility and saturation velocity of electrons cause a net shift of negative charge towards the anode direction. If we consider first the region adjacent to the anode, as electrons drift towards this electrode they leave a net positively charged region behind, which counteracts the further built-up of space-charge by screening out the external bias field. In contrast, next to the cathode the depletion of electrons and the consequent built-up of a positive space-charge region enhances the local electric field and causes further electron depletion until equilibrium establishes. This process can be additionally explained from the perspective of imposing the equilibrium condition: the current density integrated over the anode and cathode are equal. In this situation the electron and hole current are dominant at the anode and cathode, respectively. For both current densities to be equal, the largest potential drop must necessarily occur at the electrode whose majority carriers exhibit the smallest mobility, i. e. the holes next to the cathode.

### 4.3.2 Quasi-optics

When a planar antenna is placed in the interface between two dielectrics, the radiation is emitted preferentially toward the dielectric medium with higher dielectric constant. This is a consequence of the Lorentz reciprocity

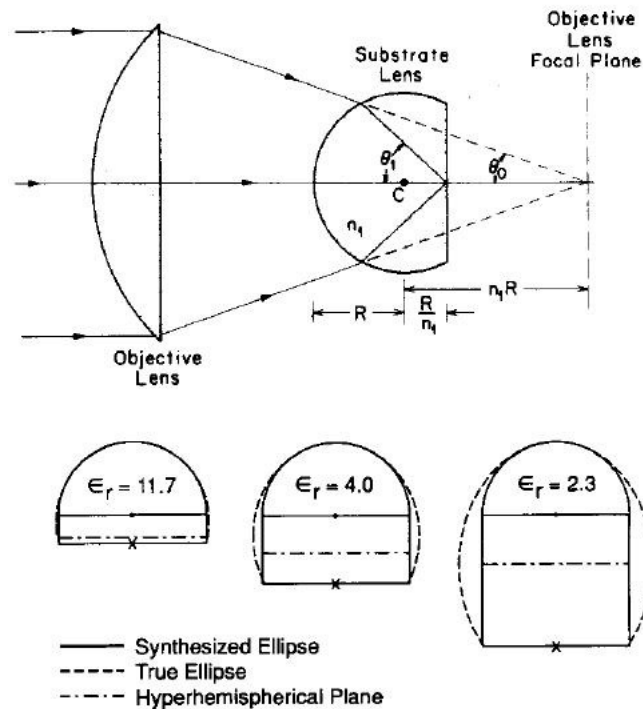


**Fig. 4.14:** (Upper) Imaging system formed by a hyperhemispherical and objective lens. (Lower) Comparison between dimensions of synthetic-hyperhemispherical, synthetic-elliptical and elliptical lens. From [63].

theorem. In fact the use of this theorem circumvents the necessity of solving boundary-value problem for the determination of far-field patterns from radiating structures.

After Rutledge [45], the power radiated towards the substrate by a dipole or slot antenna placed in the interface air-dielectric is  $\epsilon_r$  (dipole) and  $\epsilon_r^{3/2}$  (slot) times higher than that radiated into the air. Since the dielectric is semi-infinite no power is lost in the excitation of substrate modes.

This semi-infinite substrate can be simulated by attaching a lens to a (finite) antenna substrate. If correctly designed, the coma and spherical aberration can be eliminated. The dimensions of the substrate lens antenna can be chosen to form a hemispherical lens or an extended hemispherical lens, which consists of a hemisphere attached to a wafer. For certain wafer thicknesses, hyperhemispherical and elliptical lenses can be synthesized. An anti-reflection (AR) coating on the hemispherical lens avoids reflection losses from the dielectric-air interface. The hyperhemispherical form increases the antenna gain by a factor  $\epsilon_r$  [63], giving a slightly diverging beam. The hyperhemispherical geometry can be realized for  $\sin(\theta_1)/\sin(\theta_0) = n_1$  (figure 4.14 (upper)). In case of using an elliptical lens, the antenna is placed at the second focal point of the ellipse, so that the lens transforms the diverging radiation to a paraxial beam. The far-field

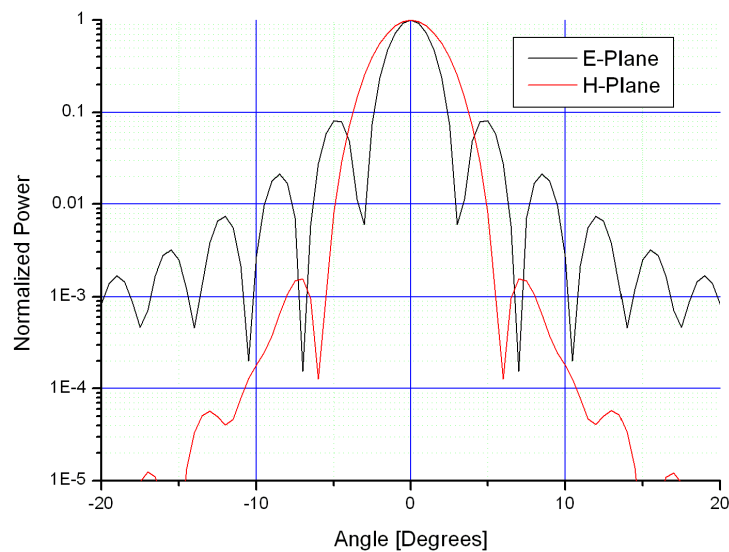


**Fig. 4.15:** Simulation of the radiation diagram of a (resonant) slot antenna at 460 GHz. The dimensions of the high resistivity silicon hemispherical lens (radius 5 mm) + extension substrate (length 1.85 mm) yield optimal directivity and minimize sidelobes.

pattern of the main beam is then diffraction limited by the substrate lens. It is easy to synthesize the aforementioned lenses by combining commercially available hemispheres and plane substrates (figure 4.14 (lower)).

Unfortunately, the calculated dimensions for the set hemisphere + extension length do not always yield an optimum directivity, since the antenna structure and its current distribution plays a major role. Therefore electromagnetic simulations (Prof. Dr. Hansen, University of Wuppertal) with a method of moments program were performed. The simulation bases on calculating first the antenna current distribution and the electric field on the lens surface. Once these parameters are calculated, the determination of the far-field antenna pattern is trivial by a Fourier transformation. The reason for this is that the equivalence principle in electromagnetic theory, which is based on the uniqueness theorem, states that a field in a region is uniquely specified by the sources in that region plus the tangential components of the electric field over the region's boundary. Therefore, the tangential electric fields over the lens surface are sufficient to univocally determine the far field antenna pattern.

Although in principle every different photomixer antenna design used during this work required individual lens substrate designs regarding the operation frequency and current distribution, for the sake of simplicity and due to the fact that our terahertz detector integrates practically all the incoming radiation in its Winston cone, only one substrate lens design was used.

This design was calculated for a resonant slot antenna at 460 GHz (figure 4.15). We glued the photomixer GaAs chips (0.35 mm thickness) on a high resistivity (HR) silicon planar substrate (1.5 mm thickness), which on turn was glued to a hemispherical lens (5 mm radius).

Since the dielectric constants of silicon and GaAs are similar, we expected negligible reflection losses in the interface GaAs chip – Silicon substrate. The thicknesses of the glue layer in all interfaces were examined and it was found that they were far below  $10\mu m$ , from which Fabry-Perot resonance effects were discarded<sup>4</sup> in the frequency band of interest (0.1 – 2 THz).

### 4.3.3 Antenna designs

The terahertz electromagnetic energy in the photomixer structure has to be efficiently coupled to free space. This is not an easy task and usually the high impedance of the small area recombination time limited photomixers (the DC resistance is of order of several tens of  $k\Omega$ ) makes conjugate impedance matching between generator (photomixer) and load (antenna) impractical. Due to its high internal resistance, one can consider the photomixer as a perfect current generator.

Since the photomixer structure is DC biased, one should minimize rf power leakage through the bias circuitry. Apart from this, other design criteria as wide-bandwidth, nearly gaussian beam profile, low cross-polarization must be considered.

Of course it is impossible to fulfill all aforementioned considerations in one design. As an example, a full-wave dipole antenna offers relatively good impedance matching and low cross-polarization, but the bandwidth can be insufficient for many applications. On the contrary, a spiral logarithmic antenna offers large bandwidths but poor impedance matching and the cross-polarization is significantly larger than that of a linear antenna.

The electrical model of a photomixer with an integrated antenna is depicted in figure 4.16. In the small signal limit, the photomixing structure is a current source with a constant internal resistance  $R_{photomixer}$ , which depends on many factors like the finger geometry, absorbed optical power, carrier lifetime, contact resistance etc. The finger structure behaves as a capacity  $C_p$  (usually of several fF) in shunt with the photomixer structure and antenna  $Z_{antenna}$ , supposing no electrically significant length between antenna and photomixer. The DC bias connection is modeled by the impedance  $Z_{bias}$ . For small bandwidth applications, an rf choke is advantageous to increase the impedance seen by the photomixer in the direction of the DC bias connection.

<sup>4</sup>For a thickness of  $10\mu m$ , a free-spectral-range of approx.  $20THz$  is obtained.

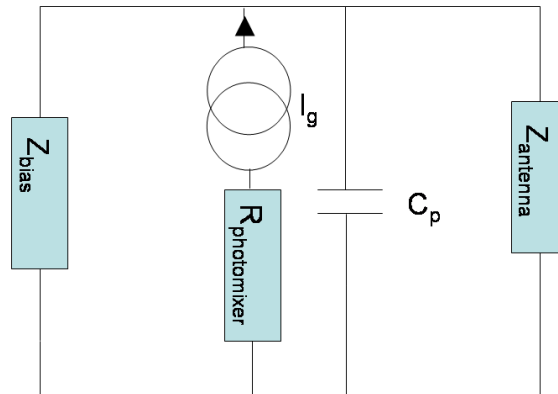


**Fig. 4.16:** Small signal model of a photomixer integrated with an antenna and rf choke.

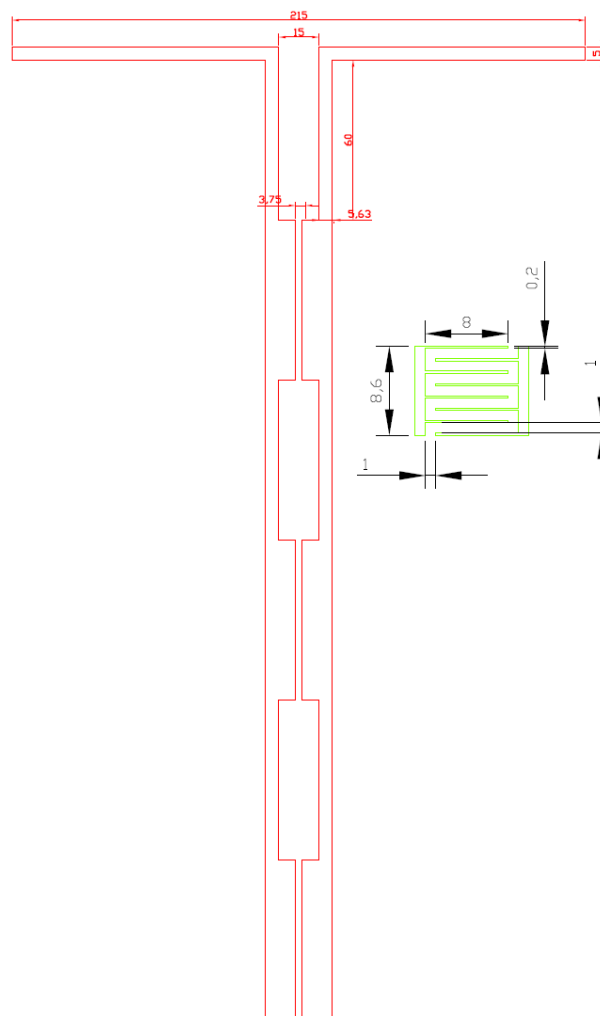
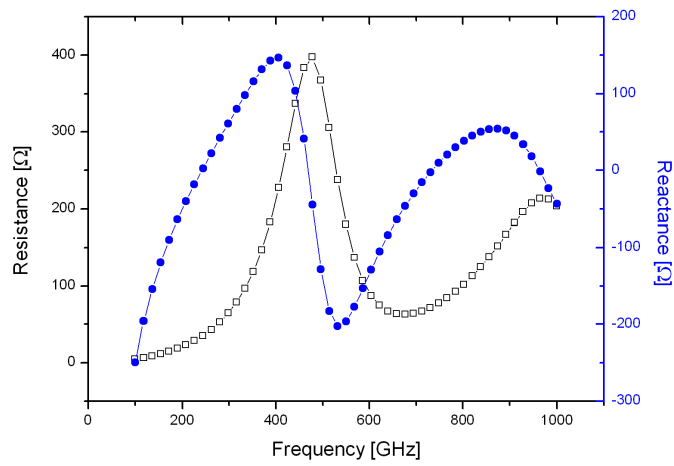
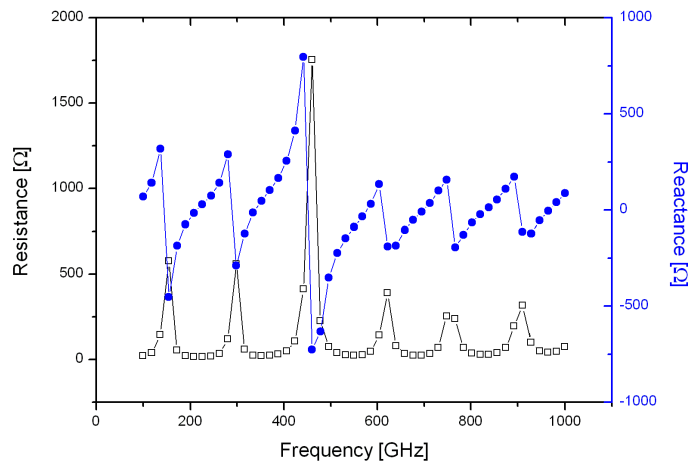


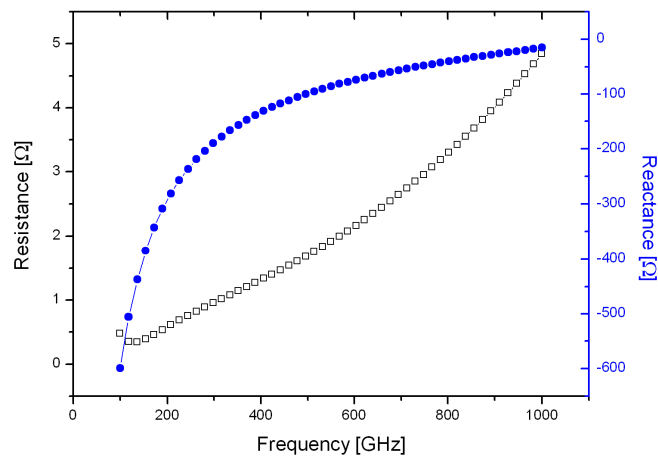
**Fig. 4.17:** Design of a resonant structure at 460 GHz. The inset shows the dimensions of a finger structure widely used during this work.



(a)



(b)



(c)

**Fig. 4.18:** Impedance of a resonant dipole antenna (a), the rf choke (b) and finger structure with eight 200 nm wide fingers separated by a 1  $\mu\text{m}$  gap(c). Simulation performed with IE3D (Zeland)

## Resonant designs

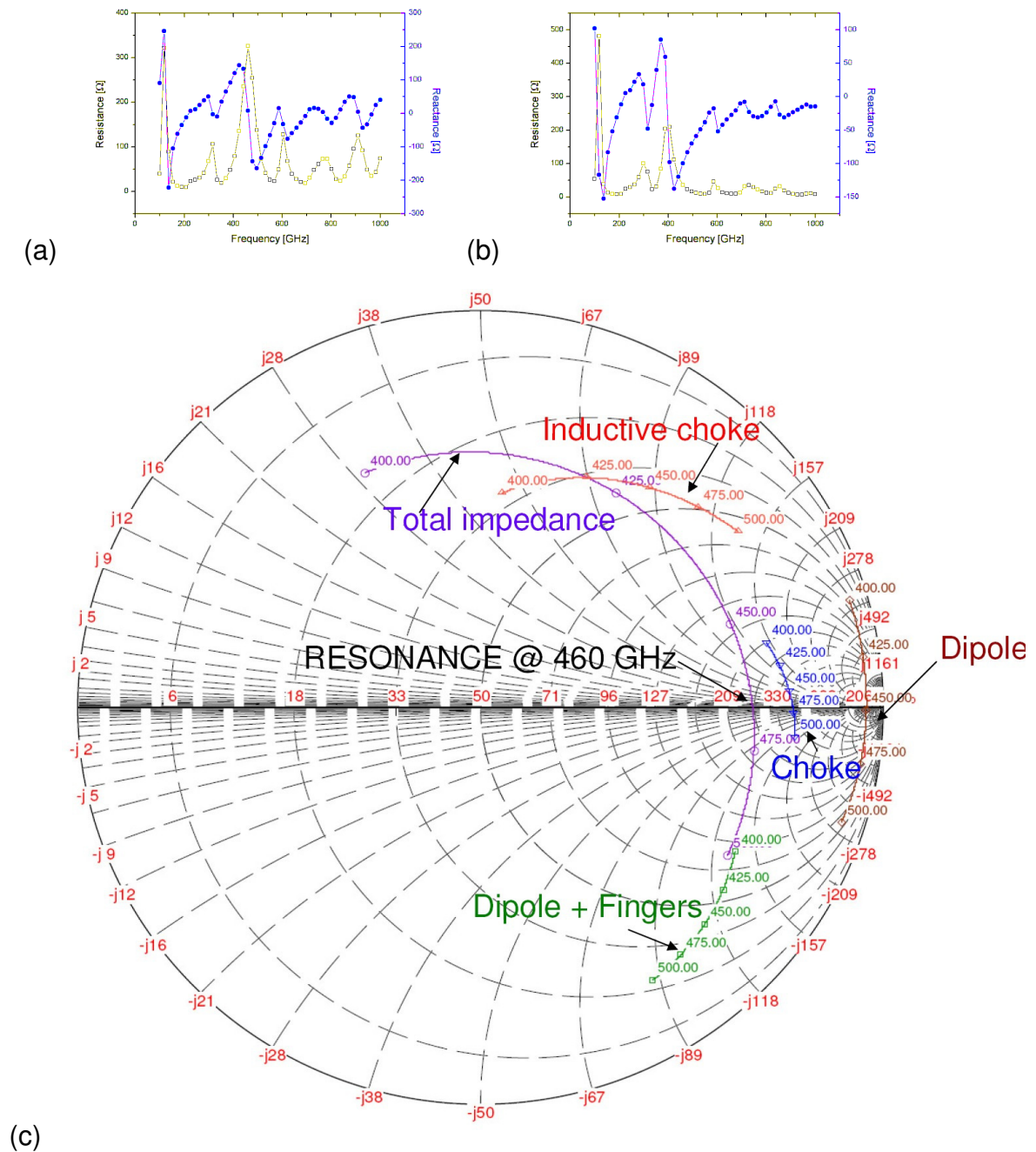
In this work, resonant designs at 460 GHz (figure 4.17) and 1.05 THz corresponding to atmospheric transmission windows of astronomical interest were performed. Figure 4.18(a), shows the impedance of the dipole antenna against frequency. The first half-wave (low impedance) and full-wave (high impedance) resonances can be seen. The antenna is operated at the full-wave resonance due to its higher impedance (higher radiation resistance) and therefore increased power transfer from the generator.

The influence of the DC bias connection can be minimized by including an rf choke consisting of alternating  $\lambda/4$  sections of high and low characteristic impedance. After  $n$ -sections, the resulting input impedance is:  $Z_{in} = (Z_{high}/Z_{low})^{2n} \cdot Z_{bias}$ , where  $Z_{high}$  and  $Z_{low}$  refer to the characteristic impedance of the  $\lambda/4$  sections and  $Z_{bias}$  is the input impedance seen after the rf choke filter. By this technique, even small impedances at the DC connection port can be increased substantially after several  $\lambda/4$  sections so that the rf power is mainly delivered to the antenna. Figure 4.18(b) shows the input impedance of an rf choke consisting of three  $\lambda/4$  high/low impedance sections, which is designed to present a high input impedance at the resonant frequency of the dipole antenna. The photomixer sees the shunt impedance of antenna and rf choke, which is almost one order of magnitude larger than that of the dipole in resonance; therefore negligible rf power leakage through the bias connection is expected.

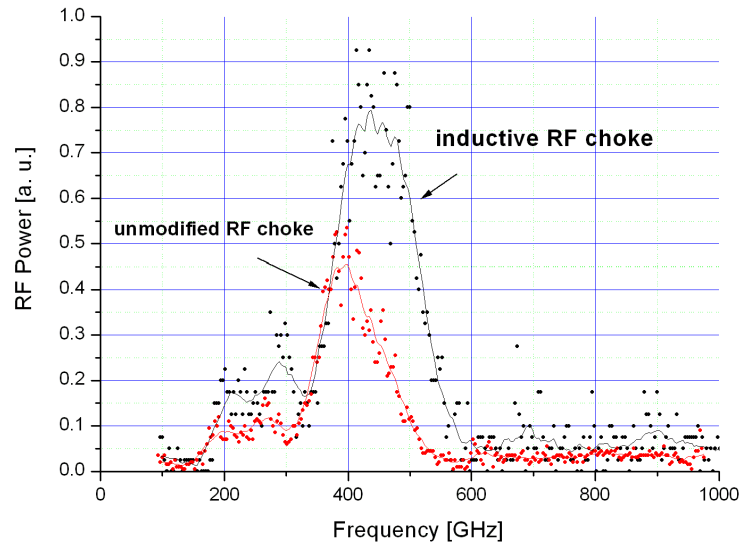
For the eight finger structure of figure 4.17 (finger gap 1  $\mu\text{m}$ , finger width 200 nm), the capacity yields approximately 1.5 fF using equation 4.5.

The negative reactance of the finger structure has mainly two negative effects: the resonance frequency of the calculated antenna gets lower and the real part of the total impedance seen by the photomixer diminishes. The impedance seen by the photomixer port due to the shunt connection of antenna + choke (figure 4.19(a)) has a resonance at the expected frequency. Nevertheless, when the finger capacity is taken into account (figure 4.19(b)), the resonance frequency lowers to 400 GHz. An inductive canceling out of the finger capacitive structure is possible [19] by reducing the length of the first  $\lambda/4$  section. Nevertheless, the amount of capacity that can be compensated by this technique is limited. Figure 4.19(c) shows the impedance of a dipole antenna with and without finger structure. As can be seen, the negative reactance added by the finger structure translates the position of the finger impedance curve toward the lower (capacitive) part of the Smith chart. The impedance curve (green) of the unaltered rf choke structure displays a resonance at the design frequency of 460 GHz and translates to the red curve when modified to show an inductive behavior (upper part of Smith chart) to cancel out the capacity of the finger structure. In the current design, the length of the first  $\lambda/4$  section had to be reduced by 60% to display an equal magnitude of admittance as the finger structure. The experimental results can be examined in





**Fig. 4.19:** Real and imaginary impedance of a resonant dipole antenna (a), the rf choke (b) and finger structure with eight 200 nm wide fingers separated by a 1 μm gap(c). Simulation performed with IE3D (Zeland)



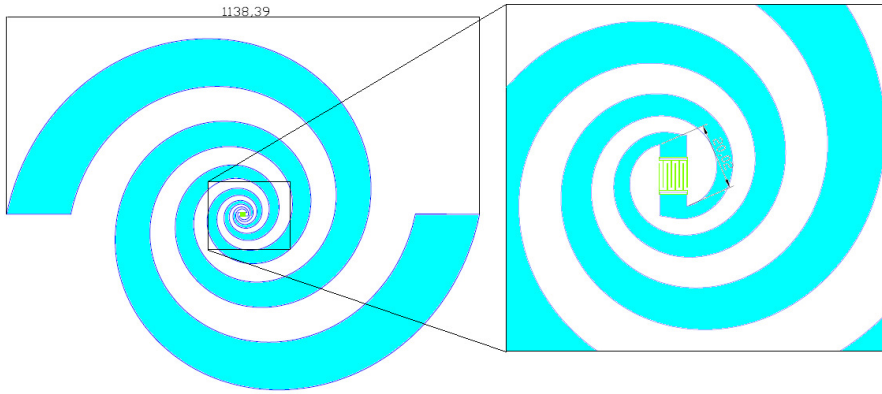
**Fig. 4.20:** Experimental results of a photomixer design with and without inductive canceling of finger capacity. The dimensions and finger structure correspond to those of figure 4.19.

figure 4.20. At higher frequencies, the finger capacity problem can only be addressed by reducing the number of fingers, thereby inevitably reducing the quantum efficiency of the photomixer.

### Broadband designs

Bow-tie and logarithmic-spiral planar antenna are useful for terahertz photomixing applications requiring a broad bandwidth. Furthermore a photomixer integrated with a broadband antenna is a very elegant approach to measure indirectly the effective carrier lifetime and does not suffer from the complexity of the methods described in section 3.4. In this work, we mainly focused on the logarithmic spiral antenna and systematically used photomixers based on this antenna design to extract the carrier lifetime by fitting the expression from section 2.5,  $P_{rf} = \frac{R}{2} \frac{(V_b G_0)^2}{\sqrt{1+\omega^2 \tau^2}} \cdot \frac{1}{\sqrt{1+\omega^2 (RC)^2}}$  to the measured data.

One arm of the logarithmic-spiral antenna is delimited by the curves given in polar coordinates by  $r_{internal} = r_0 e^{a(\phi)}$ ,  $r_{outer} = r_0 e^{a(\phi+\phi_0)}$ . The other arm has the same delimiting curves but rotated over 180 degrees. If  $\phi_0 = 90$  degrees, then the structure displays rotation symmetry and is self-complementary (i. e. the form of the antenna and its complementary are identical). Such an antenna displays a constant resistance within a relatively large range of frequencies. The theoretical calculation of the input resistance is astonishingly simple and elegant when using the extension of



**Fig. 4.21:** Design of a logarithmic spiral antenna.

the Babinet's principle made by Brooker [64], which states that the relation between the terminal impedances of a screen ( $Z_s$ ) and its complementary ( $Z_c$ ) are:

$$Z_s \cdot Z_c = \eta^2/4 \quad (4.14)$$

where both structures are embedded in a medium with intrinsic impedance  $\eta$ .

If an antenna is self-complementary, then one should expect  $Z_s = Z_c$ , and according to equation 4.14,  $Z_s = Z_c = \eta/2 = 60\pi/\sqrt{\epsilon_{eff}}$ . In our case, as the antenna is in the interface between two media (air-GaAs), the effective dielectric constant equals  $\epsilon_{eff} = (1 + \epsilon_r)/2$ . Substituting one gets  $R_{spiral} = 73\Omega$ .

Since the structure is broad-band, one might argue that the problem associated with the rf power leakage through the DC bias connection would be difficult to solve since the rf choke is a resonant structure and therefore is not of use for this type of antennas. Fortunately, if the spiral antenna has sufficient turns, most of the electromagnetic energy will be radiated before reaching the DC bias circuitry. This can be seen in the average current simulations at different frequencies from figure 4.22, where the average current density at the wide bonding position is attenuated at least 40 dB with respect to the center of the spiral antenna.

The radiation of the spiral antenna has circular polarization for the range of frequencies in which the photomixer structure is electrically small. As the frequency approaches higher frequencies, the finger structure begins to radiate more efficiently and its contribution to the overall polarization begins to be significant. The polarization of the radiation emitted by the fingers is linear, which, combined with the circular polarization of the spiral antenna, leads to an elliptical ( $f \sim 1THz$ ) polarization. As the frequency increases further, practically all the THz electromagnetic energy is radiated by the finger structure, from which follows a linear polarization ( $f \gg 1THz$ ).

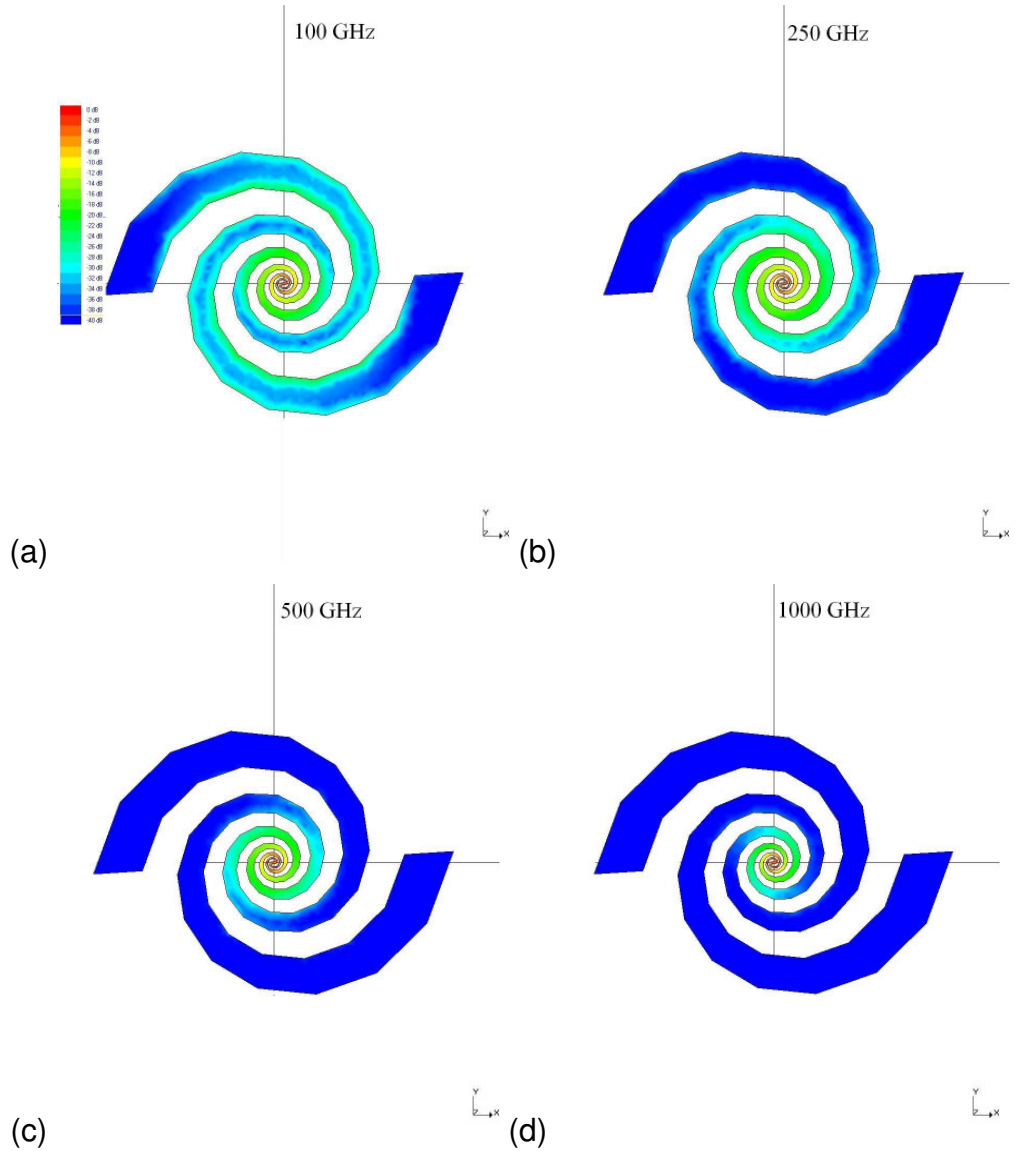


**Fig. 4.22:** Average current density in the spiral antenna with dimensions corresponding to 4.21. As the frequency increases, the current density remains closer to the generator (photomixer). Simulation performed with IE3D (Zeland)

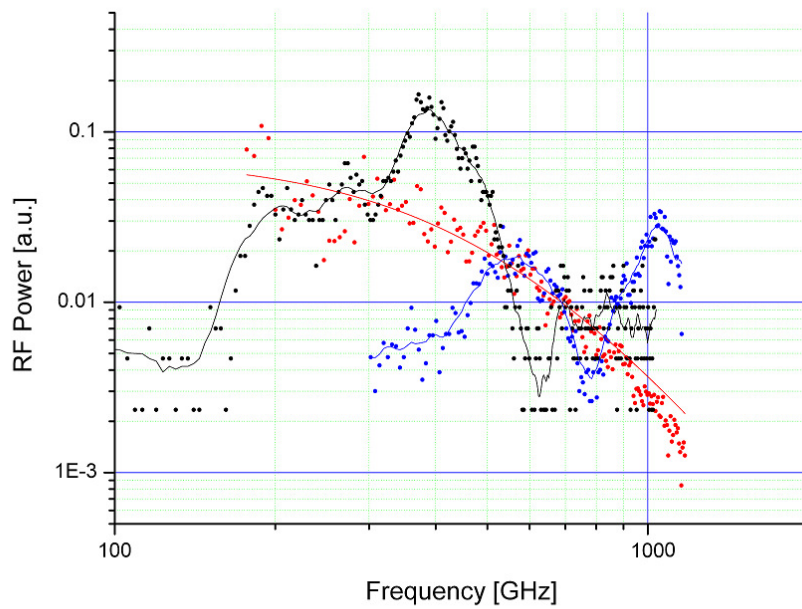


**Fig. 4.23:** Power vs. frequency dependence of a 460 GHz resonant dipole antenna (black), spiral antenna (red) and a 1050 GHz resonant dipole antenna (blue).



# Chapter 5

## Measurements with LT-GaAs photomixers

### 5.1 Introduction

In this chapter, published in [65], a study of LT-GaAs based photomixers, conducted with the goals to optimize the rf power, is presented. Part of the experiments were done with photomixers integrated with broadband spiral antenna designed for frequencies up to 1 THz. The LTGaAs photomixers were fabricated at Forschungszentrum Jülich. The MBE growth conditions of the material were optimized by comparing the performance of photomixers growth and annealed at different temperatures. Once the material with best performance was determined (growth temperature = 300 °C), the metallization and finger geometry were optimized (structures with eight interdigitated fingers, finger gap = 1 micron, finger width = 200 nanometers). The results presented in this chapter were obtained with the optimum material and metallization parameters. Measurements at 30 K have been performed by attaching pigtailed photomixers to the cold finger of a closed-cycle cooling machine. Comparative measurements between room temperature and 30 K are discussed later at the end of this chapter.

### 5.2 Measurements

The terahertz power depends quadratically on the product bias voltage x photoconductivity (i. e. photocurrent). Keeping the risk of photomixer burnout in mind, for a given material, the following possibilities were considered to increase the rf power:

- higher bias voltage
- higher photoconductance: higher laser power

- better thermal management: Cryogenic operation

We studied the effect and limits of the described parameters on the photomixer performance by conducting a series of different measurements.

### 5.2.1 The effect of bias voltage

The effect of the bias voltage on the photomixer performance was first studied via rf power vs. voltage/ photocurrent curves. Of course, during the measurements it is necessary that the two laser frequencies and optical power remain unchanged. The free-running lasers used for the experiment drift slightly in frequency ( $\sim 500\text{MHz}$ ) during the measurement timescale (several minutes). The relative frequency variation is therefore negligible<sup>1</sup> and the difference frequency can be considered as constant. Unfortunately, as can be seen in figure 5.1, the separation between fiber optic and photomixer surface is critical and behaves like a Fabry-Perot cavity. Minimal changes in the separation of the fiber optic lead to large transmitted laser power (photocurrent) variations. A rough estimation of the finesse of the Fabry-Perot cavity is  $F_R = \frac{\pi \sqrt{R_f R_p}}{1 - \sqrt{R_f R_p}} \sim 1.6$ , with  $R_f$  and  $R_p$  being the reflectivity at fiber-air and air-GaAs interfaces, respectively. This finesse explains photocurrent variations up to 50%. The larger observed – up to 66% – photocurrent variations are probably caused by the presence of the reflecting metallic fingers, which increase the overall reflectivity of the photomixer surface. The position of the fiber optic, which is controlled by a piezoelectric actuator, displays very slight variations (several hundreds of nanometers on the typical timescale of a measurement, which is several tens of seconds). However, these are sufficient for photocurrent variations to occur. For these reasons, when plotting the rf power against bias voltage, some scatter in rf power data points originates due to the different illumination conditions for every voltage data point.

The dependence of photocurrent with optical power is linear and only shows a saturation component for very large optical powers (>150 mW), for which phonon scattering might be responsible. Although the illumination conditions were not completely constant during the measurements (10% variations observed for a typical measurement timescale), these variations are contained in the photocurrent data. Therefore, if the rf power is plotted against the photocurrent rather than against the bias voltage, the scatter in the data points disappears, making it possible to analyze in detail the rf power saturation from the measurement curves.

Graph 5.2 (left) shows a typical rf power vs. photocurrent (voltage) dependence. For low frequencies the theoretical quadratic dependence holds

<sup>1</sup>The frequency variations may potentially translate into power variations since the radiating structure is frequency dependent. Nevertheless, for the typical relative frequency variations – one per mil in minutes timescales –, this effect is insignificant.



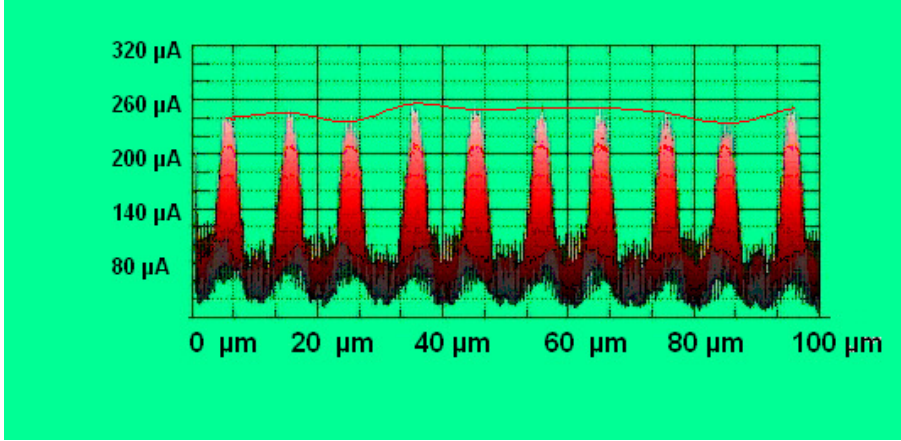


**Fig. 5.1:** Photocurrent variations with the fiber optic distance relative to the photomixer surface. The variations result from the Fabry-Perot cavity that develops between fiber output facet and photomixer surface. From [66]

even at high voltages (photocurrents). As the frequency increases, a saturation mechanism degrades the rf power at high photocurrents. The onset of the saturation component occurs at lower photocurrents the higher the frequency. In the extreme case of  $1THz$ , the rf power has no longer quadratic a dependence on photocurrent. The photocurrent-bias voltage curve displays three regimes of operation: sub-linear (probably due to velocity saturation [53]), linear and over-linear, which as we shall see at the end of this section is intimately connected with the increase of the effective carrier lifetime.

To gain some insight into the physics of rf power saturation, rf power vs. frequency scans were performed for different bias voltages 5.3. By fitting the theoretical curve

$$P_{rf} = \frac{R}{2} \frac{(V_b G_0)^2}{\sqrt{1 + \omega^2 \tau^2}} \cdot \frac{1}{\sqrt{1 + \omega^2 (RC)^2}}$$

to the measured data points – considering an antenna impedance of  $\sim 73\Omega$  and interdigitated capacity of  $1.5fF$  –, the effective carrier lifetime can be extracted for the individual bias voltages (see figure 5.4). It is remarkable that the effective carrier lifetime grows monotonically up to an average electric field of  $100KV/cm$  and above this value it increases abruptly. This behavior remains practically unchanged for all laser powers in the graph.

According to equation 2.12

$$\begin{aligned} \mathbf{J}_x(z, t) \approx G_0(z) \cdot e \left[ (\tau_n v_n + \tau_p v_p) + \left( \frac{\tau_n v_n}{\sqrt{1 + (\omega \tau_n)^2} \sqrt{1 + (\omega RC)^2}} \right. \right. \\ \left. \left. + \frac{\tau_p v_p}{\sqrt{1 + (\omega \tau_p)^2} \sqrt{1 + (\omega RC)^2}} \right) \cos(\omega t + kz) \right] \end{aligned} \quad (5.1)$$

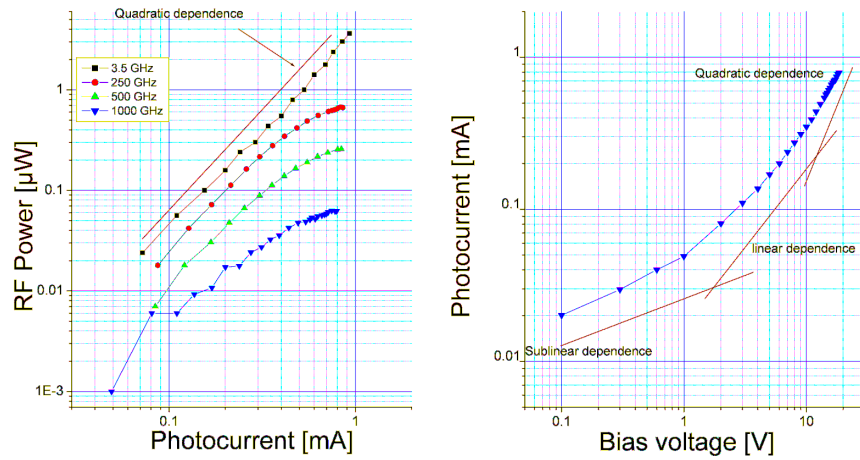


**Fig. 5.2:** (left) rf power vs. photocurrent for different frequencies and a laser power of 80 mW. (right) photocurrent vs. bias voltage for a laser power of 80 mW. The device was an eight finger photomixer integrated with a logarithmic spiral antenna –design from figure 4.21. The 3.5 GHz data were measured with a calibrated microwave power meter connected to the photomixer via a bias-tee.

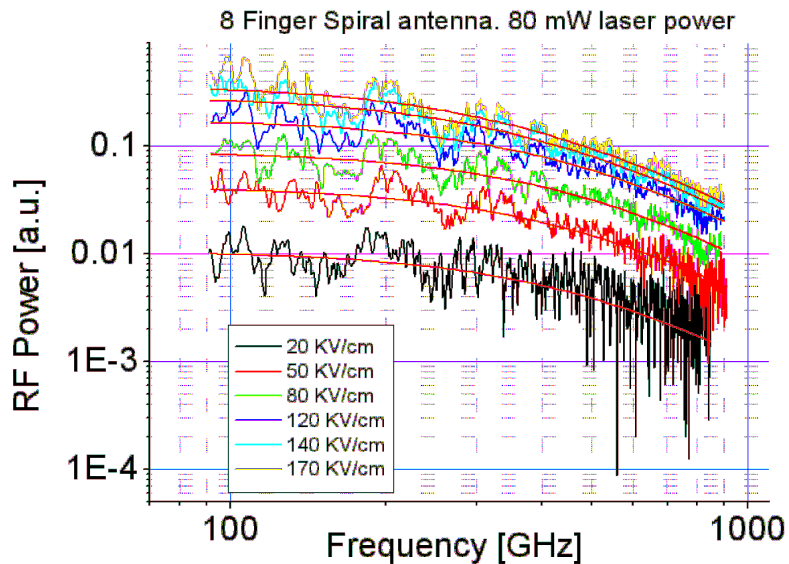


**Fig. 5.3:** rf power vs. frequency for different bias voltages and a laser power of 80 mW. The device was an eight finger photomixer integrated with a logarithmic spiral antenna –design from figure 4.21. The average electric field values in the legend are calculated using a parallel plate approximation. The power variations arise from standing waves in the measurement setup.

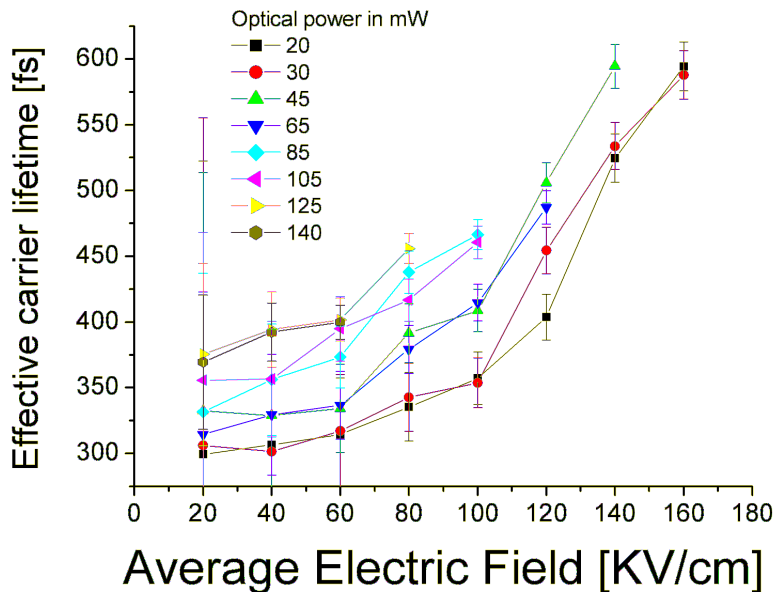


**Fig. 5.4:** Carrier lifetime dependence on the electrical field for different laser powers. The effective carrier lifetime was extracted by fitting the theoretical rf power vs. frequency roll-off curve to the measured data. The device was an eight finger photomixer integrated with a logarithmic spiral antenna –design from figure 4.21.

the DC photocurrent depends linearly on the effective carrier lifetime. As seen in the measurements, the effective carrier lifetime increases substantially above average electric fields of 100 KV/cm. Consequently, the DC photocurrent should increase in the same fashion as the effective carrier lifetime. This is in agreement with the observed over-linear photocurrent dependence on bias voltage; see graph 5.2 (right).

Zamdmer et al. [59] studied the increase of electron lifetime at high electric fields in LT-GaAs and concluded that it was caused by a decrease in the cross section of attractive Coulomb donor states. From the results shown in figure 5.4 it is clear that the photomixer should be operated at a bias voltage for which the electron lifetime is maintained within an acceptable range. Further increase of bias voltage to achieve larger photocurrents is pointless, and therefore it is much more convenient to increase the photocurrent via laser power.

### 5.2.2 The effect of laser power

When using higher laser powers to increase the photocurrent, a saturation behavior is also present as can be seen in figure 5.5. Likewise, saturation with bias voltage, the effect of rf power saturation with laser power is frequency dependent, having a more negative effect at higher frequencies.

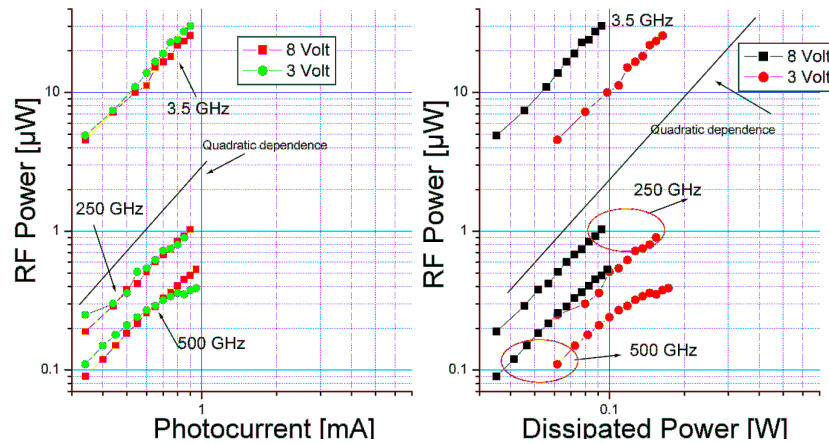


**Fig. 5.5:** (right) rf power dependence on photocurrent for fixed bias voltages (3 and 8 volts) at different frequencies. The photocurrent increases with laser power in a range from 5mW up to 140mW. (left) rf power dependence on total dissipated power (laser power + Joule power) calculated from measurements from the graph to the left. The device was an eight finger photomixer integrated with a logarithmic spiral antenna – design from figure 4.21.

Nevertheless it seems to be less severe than the voltage saturation and shown in next section, cryogenic operation alleviates the saturation effect.

A possible explanation for saturation with optical power is that under high input optical power densities, the amount of unoccupied electron traps, which are responsible for the fast response component of LT-GaAs, diminishes [67], [68]. The electrons would need a longer time to find a free electron trap and consequently the electron lifetime would increase and the expected quadratic power dependence would reach a saturation regime. If this effect were the reason for the observed saturation, the longer carrier lifetime would lead to an increase in the DC photocurrent, i. e. the DC photocurrent vs. laser power dependence should display an over-linear behavior above a certain laser power. This is in disagreement with the observed linear photocurrent-laser power dependence and therefore we can discard this effect as an explanation for the frequency dependent saturation. Furthermore, in order to see saturation of traps, optical intensities of three orders of magnitude larger than those used in this work are required.

A detailed analysis of the underlying physical phenomena involved in the observed saturation behaviors is out of the scope of this work. However, an attempt to understand these phenomena qualitatively from the available measurements is made in the following.

Figure 5.6 shows the effective carrier lifetime dependence on photocurrent for increasing bias voltage and laser power. A total of 46 rf power vs. frequency measurements were performed for laser powers from 20 to

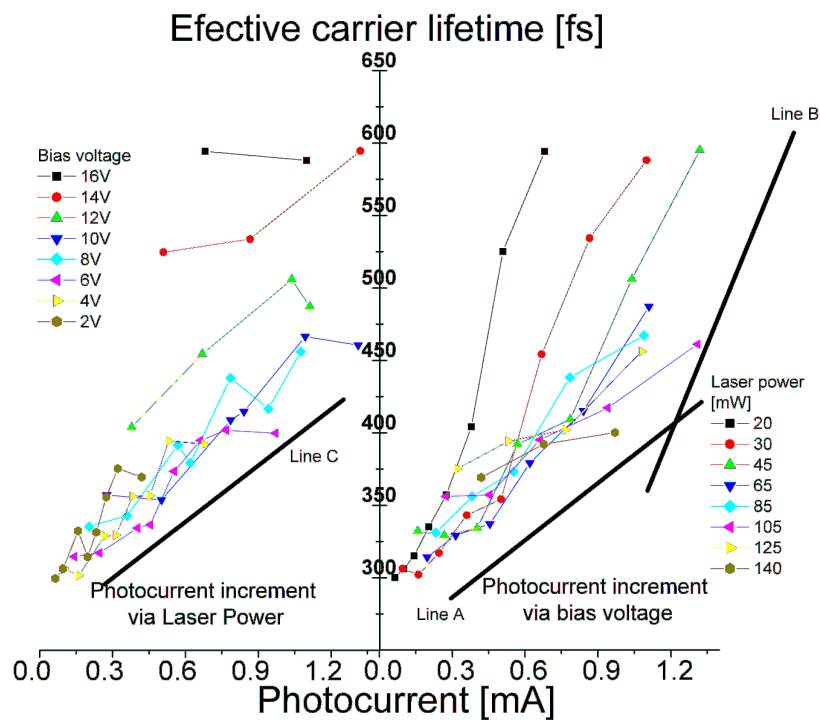


**Fig. 5.6:** Carrier lifetime dependence on the photocurrent for increasing laser power (left) and increasing bias voltage (right). Error bars are not shown to avoid confusion due to the large information density in the graph. The device was an eight finger photomixer integrated with a logarithmic spiral antenna – design from figure 4.21.

140 mW and bias voltages from 2 up to 16 Volts. The effective carrier lifetime gives very useful information about the influence of laser power and voltage on the device bandwidth and its saturation behavior.

The black lines in the right and left graphs of figure 5.6 indicate qualitatively <sup>2</sup> the evolution regimes of effective carrier lifetime with bias voltage and laser power controlled photocurrent. The slope of line A coincides suspiciously with that of the line C in the left graph. This could be interpreted as a similar physical mechanism acting on the effective carrier lifetime in both curves. Since independently on how the photocurrent is increased, Joule heating happens, a mechanism derived from the device heating as phonon scattering could explain the observed results (this hypothesis will be further tested in section 5.2.3). Line B displays a higher slope and results from the mentioned decrease in the cross section of attractive Coulomb donor states at higher voltages and therefore is not present in the laser power controlled photocurrent curve. If we compare curves at 20, 30 and 45mW laser power, the onset of line B takes place at different photocurrent values. The reason for this is that the electric field (i. e., bias voltage) – and not the photocurrent – is the parameter which determines the onset of line B (this can be better seen in graph 5.4). Since the photocurrent depends both on laser power and bias voltage, and the measurements were performed at different laser powers, the onset of line B is shifted accordingly to the used laser power of every curve.

In summary, the rf power saturation is more sensitive to photocurrent increase via bias voltage than via laser power. The main advantage of operating the photomixer at higher laser powers is that the onset of the most severe saturation component – line B in figure 5.6 –, takes place at higher photocurrents. Figure 5.7 illustrates clearly this fact at 1THz.

### 5.2.3 Cryogenic operation

The room temperature (RT) thermal conductivity of GaAs ( $0.46Wcm^{-1}K^{-1}$  <sup>3</sup>) is improved at lower temperatures ( $3.1Wcm^{-1}K^{-1}$  at 77K) [23]). The lower thermal impedance of the photomixer allows operation at higher optical powers and/or bias voltages.

When using a cryostat, the installation of the CCD camera and piezoelectric actuator for fiber optic positioning are problematic. In this case it is convenient to pigtail<sup>4</sup> the fiber optic. The adhesive NOA 61 A (Norland adhesive) was used, which is nearly transparent for the NIR range and can be either thermally or cured by ultraviolet light. We deposited a drop

<sup>2</sup>except for the two measurement points of the left graph at 16 V, which are not sufficient to define an overall trend.

<sup>3</sup>For non-stoichiometric GaAs this value gets as low as a quarter [44] of the stoichiometric GaAs value.

<sup>4</sup>i. e., to glue the fiber optic to the photomixer by using an optical cement.

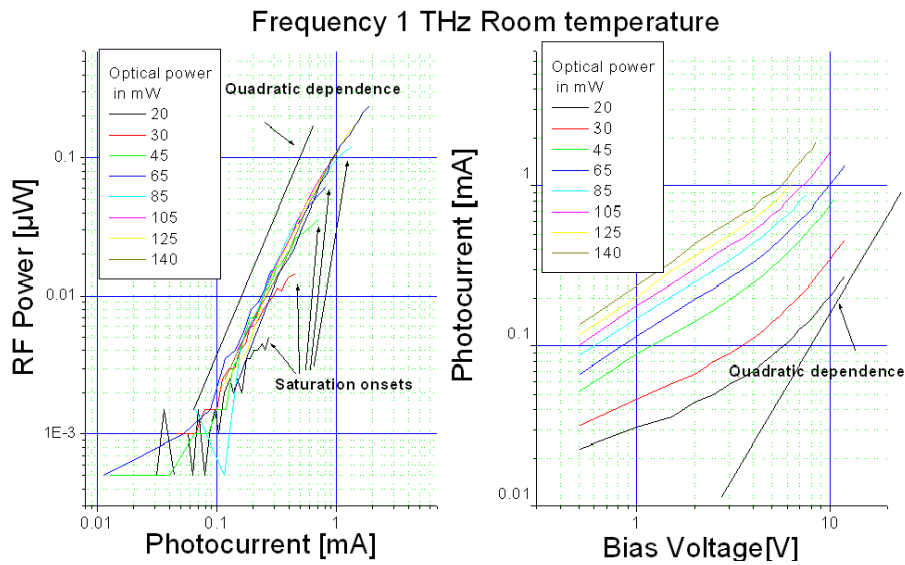


**Fig. 5.7:** (right) rf power dependence on photocurrent for different laser powers at 1 THz. The photocurrent increases via bias voltage from 2 to 16 Volts. The rf power scales sub-quadratically with photocurrent and saturates at higher photocurrent the higher the optical power. (left) I-V dependence for the different laser powers. The device was an eight finger photomixer integrated with a logarithmic spiral antenna –design from figure 4.21.

( $\sim 125$  microns diameter) of the adhesive on the tip of the fiber optic and approached the fiber to the photomixer surface by about 100 microns. At this distance, the adhesive flew by capillary action and covered a surface of around 300 microns diameter. The viscosity of the adhesive was optimal since once deposited, it did not spread over the surface and allowed the position of the fiber to be easily adjusted with the piezoelectric actuator. The pigtailed photomixer was mounted on a cold plate attached to the cold finger of a closed-cycle cooling machine. The rf beam was coupled out of the dewar through a Teflon window.

Graph 5.8 (left) shows the rf power vs. photocurrent (voltage) dependence at a temperature of  $30\text{K}$  at different laser powers for  $1\text{THz}$ . In contrast to RT – see graph 5.7 – the onset of saturation occurs at higher photocurrents and the rf power dependence over photocurrent is almost quadratic. Due to the increased thermal conductivity at low temperatures, the device can withstand higher photocurrents. Graph 5.8 (right) shows a similar non-linear I-V characteristic as in the RT case, from which one can deduce that the effective carrier lifetime increase with bias voltage is still present at low temperatures.

In order to complete our comparative study at low temperatures, we performed rf power vs. frequency measurements at different bias voltages and laser powers like those presented in section 5.2.1. From the curves the effective carrier lifetime was extracted. Graph 5.9 shows the results.

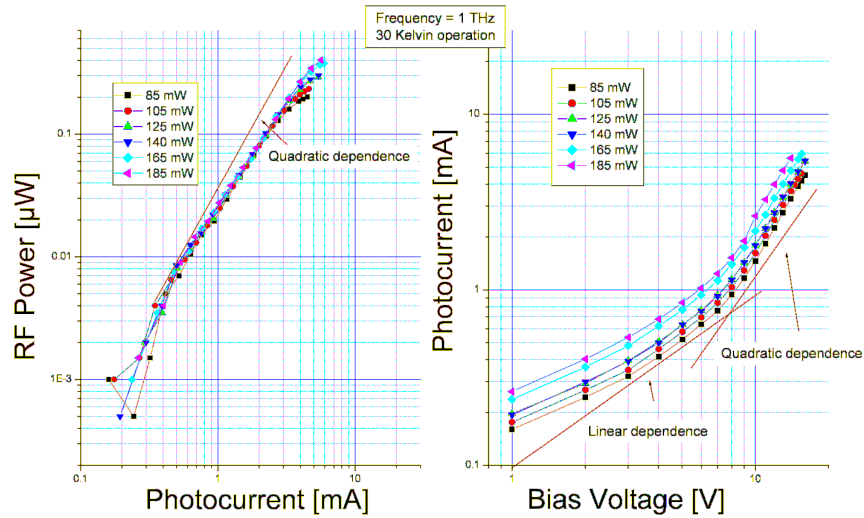


**Fig. 5.8:** (right) rf power dependence on photocurrent for different laser powers at a temperature of 30 K and a frequency of 1 THz. The photocurrent increases via bias voltage from 2 to 16 Volts. The rf power scales sub-quadratically (power of 1.65) with photocurrent. The better thermal conductivity of GaAs at 30 K allows to use higher optical powers without damaging the device. (left) I-V characteristic curves. The device was an eight finger photomixer integrated with a logarithmic spiral antenna – design from figure 4.21.

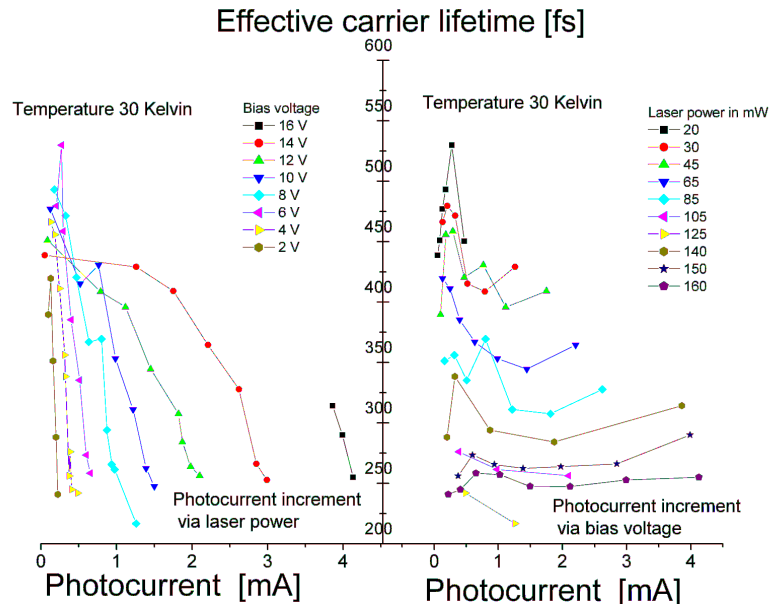


**Fig. 5.9:** Carrier lifetime dependence on the photocurrent at 30 Kelvin for increasing laser power (left) and increasing bias voltage (right). The device was an eight finger photomixer integrated with a logarithmic spiral antenna – design from figure 4.21.



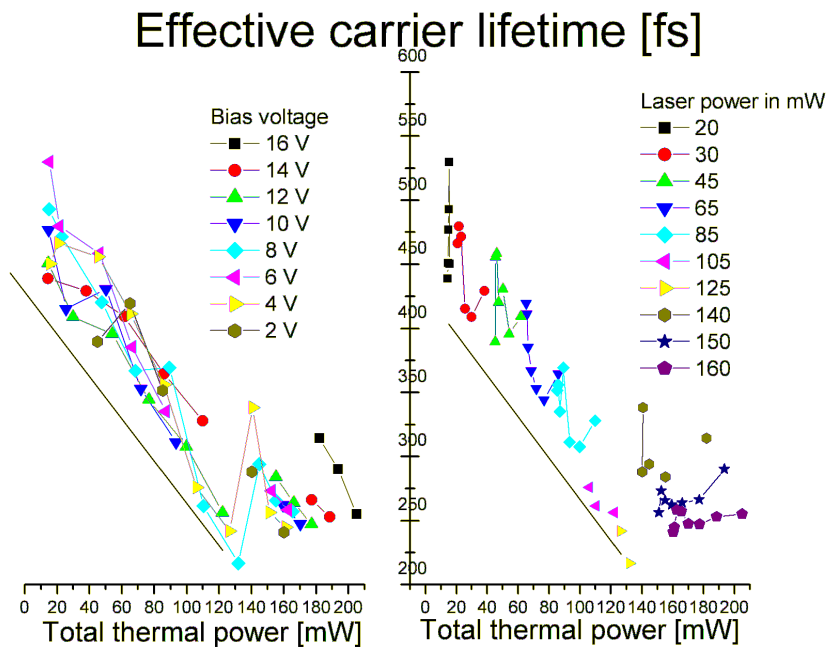


**Fig. 5.10:** Carrier lifetime dependence on the photocurrent at 30 Kelvin for increasing laser power (left) and increasing bias voltage (right). The device was an eight finger photomixer integrated with a logarithmic spiral antenna – design from figure 4.21.

For the photocurrent increment via laser power the trend is inverse to the RT case: for higher laser power the effective carrier lifetime decreases! This effect is more accentuated at lower bias voltages since a small increment in the laser power leads to a drastic reduction of the effective carrier lifetime. At high voltages, the reduction of effective carrier lifetime gets more gradual. Regarding the dependence of the effective carrier lifetime over bias voltage – graph 5.9 (right) –, it is harder to define an overall trend. For small photocurrents, the effective carrier lifetime is determined by the laser power: the higher the laser power, the lower the effective carrier lifetime. The effect of the bias voltage is to increase slightly the carrier lifetime. In this case, this increment is significantly smaller than for the RT case.

A consistent explanation of the observed phenomena would be that the effective carrier lifetime is temperature dependent. In order to test this hypothesis let us consider that the photomixer can be modeled as a lumped thermal resistance with a thermal power consisting of two factors:  $P_{thermal} = P_{optical} + P_{Joule}$ . Since the electron-hole recombination takes place mainly via recombination centers, we can ignore radiative recombination and therefore the absorbed optical power is transformed into lattice heating (phonons). It is important to remark that the given values of laser power refer to incident power and therefore the Fresnel reflection coefficient ( $R \sim 32\%$ ) must be considered to calculate the absorbed power.

The  $P_{Joule}$  term is the ohmic power (i. e. photocurrent x bias voltage) and is well below the absorbed optical power (by a factor of two the most). Therefore, one can assume that the main contribution to the thermal power comes from the  $P_{optical}$  factor.

If the x-axis of graph 5.9 is changed to thermal power a grosso modo  $-1.6 fs/mW$  dependence is obtained for the effective carrier lifetime vs. thermal power; see graph 5.10.

A possible explanation for the observed dependence of lifetime with thermal power is that at low temperature, freezing of electron traps might arise. As mentioned in chapter 4, the ionization probability of defects follows a Fermi-Dirac distribution. This distribution "freezes out" at low temperatures increasing the effective carrier lifetime. The thermal power is then of critical importance in a certain temperature range since it determines the local semiconductor temperature and therefore the concentration of ionized traps.

# Chapter 6

## Measurements with ion-implanted GaAs photomixers

### 6.1 Introduction

The experimental study of defect-rich GaAs is widened in this chapter with ion-implanted GaAs. Although this material is fabricated in a rather different way than its counterpart LT-GaAs, both share similar structural and electrical features. The fabrication steps of this material are first presented. A comparative study of the photomixing measurements analyzes the effect of dose, energy and spicing aiming at a power performance optimization. The results presented in this chapter were published in [69].

### 6.2 Motivation

In contrast to LT GaAs, the defects created in ion-implanted GaAs [70], [71], [72], [73] can be tailored by varying the implantation dose and energy. The precise control over these parameters helps to overcome the reproducibility limitations of LT GaAs. Collision of incoming ions with the lattice atoms forms vacancies, interstitials, antisites and other defects, so that the material can exhibit similar carrier-trapping mechanisms as LT-GaAs. It is important that the ions do not change by themselves the properties of the material but rather that the material properties be defined by the bombardment through the ion beam. To achieve this, the implantation energies can be selected so that the peak of implantation profile is situated substantially deeper than the optical absorption length in GaAs, which is  $\sim 1\mu\text{m}$ .

As seen in figure 6.1(a), the ion-simulated concentration peak is located deeper than the photoactive volume for the energies and species used. The defect concentration shows an almost linear increase in the first  $\mu\text{m}$  –

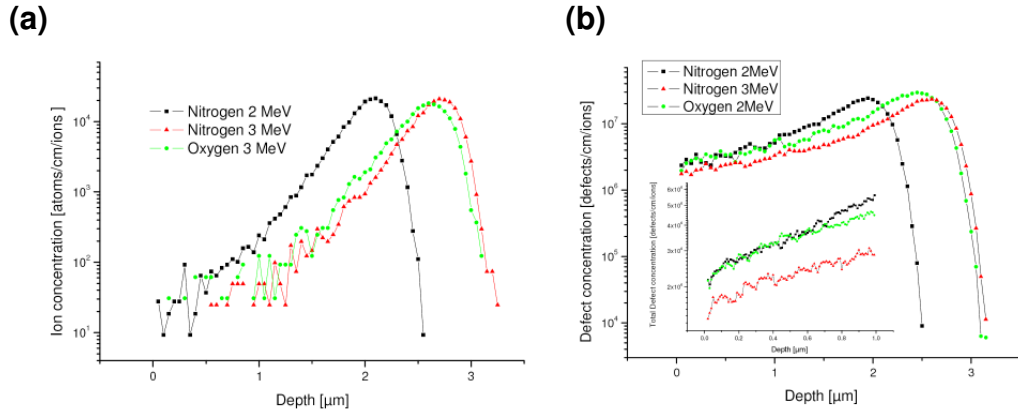


**Fig. 6.1:** (a): Concentration of ions vs. depth. If multiplied by the dose in  $\text{ions}/\text{cm}^2$ , this yields the ion concentration in  $\text{ions}/\text{cm}^3$ . In all cases the peak is situated deeper than the optical absorption length. (b): Concentration of defects vs. depth in same units as (a). The peak coincides with that of the ion concentration. Note that the defect concentration is around three orders of magnitude larger than the ion concentration in the first  $\mu\text{m}$ . The ion and defect concentrations were computed by Stopping and Range of Ions in Matter (SRIM), where a Monte-Carlo simulation of  $10^5$  ions was performed.

see inset of figure 6.1(b) – from which one should expect similar behavior for the samples implanted with nitrogen at 2 MeV and oxygen at 3 MeV.

### 6.3 Fabrication

We implanted a set of semi-insulating (100) GaAs wafers with  $\text{N}^{3+}$  and  $\text{O}^{4+}$  with doses varying from  $3 \cdot 10^{11} \text{cm}^{-2}$  to  $3 \cdot 10^{13} \text{cm}^{-2}$  at 2 MeV and 3 MeV ion energies; details can be found in Table 6.1. The ion implantation was performed at the tandem accelerator of the Institute for Nuclear

dose(ions/cm <sup>2</sup> )	3 MeV Oxygen	3 MeV Nitrogen	2 MeV Nitrogen
$3 \cdot 10^{11}$			✓
$5.6 \cdot 10^{11}$		✓	
$1.8 \cdot 10^{12}$	✓		
$3 \cdot 10^{12}$			✓
$5.6 \cdot 10^{12}$	✓	✓	
$10 \cdot 10^{13}$		✓	
$1.8 \cdot 10^{13}$	✓	✓	
$3 \cdot 10^{13}$	✓		

**Tab. 6.1:** Matrix of implantation energy and dose. The marked cells represent the processed and measured photomixers.

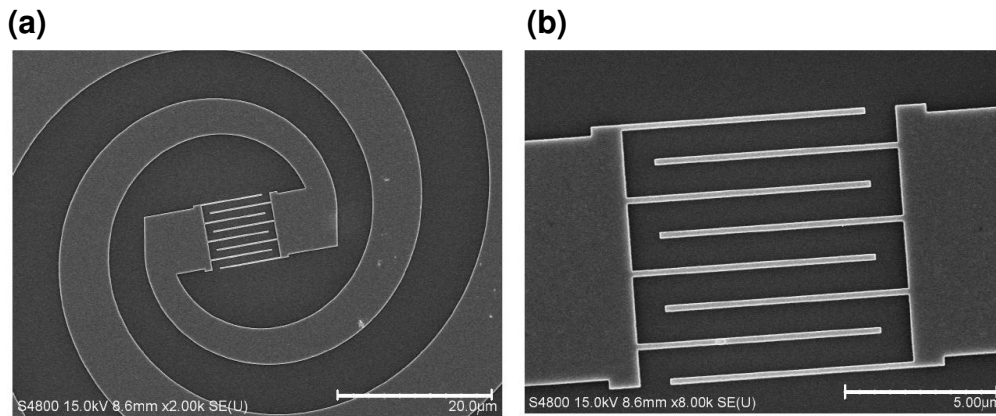


**Fig. 6.2:** (a) Scanning electron microscope (SEM) picture of the feed point of the log periodic spiral antenna. The interdigitated area is shown in (b).

Physics, University of Cologne. Since the lowest energy available from the accelerator was 15 MeV, aluminum foils were fabricated with different thicknesses to diminish the ion beam energies to 2 MeV and 3 MeV for the oxygen and nitrogen ions. The ion FWHM energy dispersion after the foils was calculated to be less than 10 % for all cases. To illuminate homogeneously the GaAs sample area, which was a quarter of a 2" wafer, the 3 mm FWHM ion beam was deflected by different wobble signals in the x and y axes, thereby avoiding the formation of any periodic pattern. No sample annealing was performed after implantation, so that the primary trapping mechanism is expected to be the point defect  $As_{Ga}^+$ , in contrast to annealed LT-GaAs where both  $As_{Ga}^+$  and As precipitates are present.

After the ion implantation, photomixer structures were processed on the different wafers - see figures 6.2 (a) and (b) - at the MC2 microstructure facility of Chalmers Technical University, Gothenburg, Sweden using standard e-beam lithography. The metallization consisted of a 10/200 nm thick Ti/Au layer and the metal-semiconductor-metal (MSM) photomixing area with dimensions  $\sim 9 \mu\text{m} \times 9 \mu\text{m}$  was composed of eight fingers with 200 nm width and 1  $\mu\text{m}$  gap. The patterned antennae were self-complementary log-periodic spirals with three turns to exhibit a nearly constant impedance in the range of study (100 GHz to 1 THz). Each individual photomixer was cleaved and mounted on a high resistivity silicon hyperhemispherical lens whose dimensions were calculated to collimate the terahertz radiation from the planar antenna. We bonded the outer spiral antenna arms to bias the photomixer structure.

## 6.4 Measurements

Three different measurements to study the implanted materials were performed: a) DC curves relating photocurrent to applied voltage for 80 mW laser power, b) terahertz power curves at 300 GHz, 500 GHz and 1 THz versus bias voltage for the same laser power and c) terahertz power versus frequency curves for constant bias voltage and DC photocurrent, thereby varying the laser power up to 80 mW. From the last set of curves, the effective photocarrier lifetime was estimated by fitting the equation (see section 2.5):

$$P_{rf} = \frac{R}{2} \frac{(V_b G_0)^2}{\sqrt{1 + \omega^2 \tau^2}} \cdot \frac{1}{\sqrt{1 + \omega^2 (RC)^2}} \quad (6.1)$$

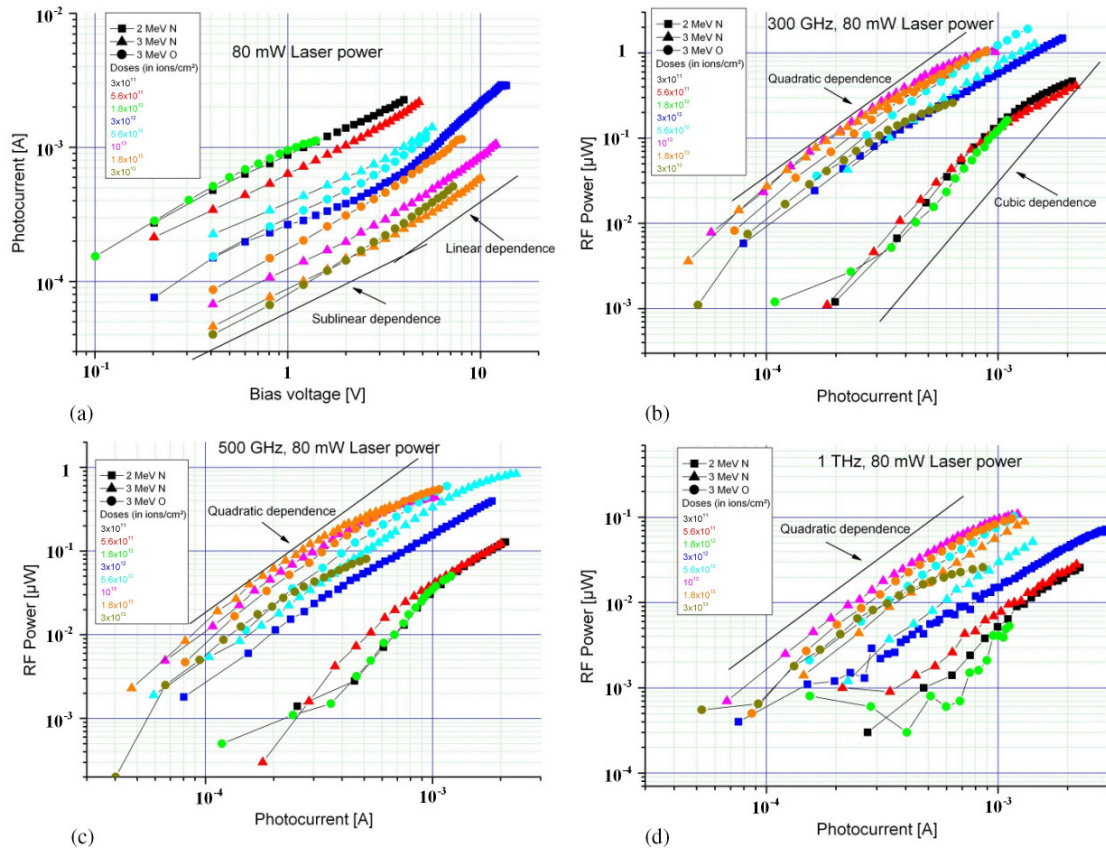
to the measurements.

Figure 6.3(a) represents the photocurrent as a function of bias voltage for photomixers on different implanted materials where the laser power was set to 80 mW. The I-V characteristic begins with a sub-linear dependence which becomes linear and super-linear at higher voltages (this is especially evident in the sample with a dose of  $3 \cdot 10^{12} \text{ cm}^{-2}$ ). Drift velocity saturation explains [74] the sub-linear range whereas at higher voltages, the well known [59] increase of carrier lifetime with voltage would increase the photoconductance and consequently the photocurrent. Other effects like impact ionization may play a role as well.

In contrast to PIN photodiodes, no plateau was found in the I-V curve since the electric field was not uniform, so that the regions next to the electrodes showed velocity saturation first whereas the regions located deeper into the substrate and in the middle of the electrodes needed higher voltages for velocity saturation to occur. As a result, the saturation mechanism is smeared out in the I-V characteristic. There was an evident reduction of DC photocurrent at higher implantation doses since the presence of defects reduces the carrier lifetime, and consequently, the steady-state carrier concentration in accordance with

$$J_{DC}(E) \propto \tau_p(E) v_{pdrift}(\mu_p, E) + \tau_n(E) v_{ndrift}(\mu_n, E)$$

where  $\tau_{n,p}$ ,  $\mu_{n,p}$  and  $v_{n,pdrift}$  are the carrier lifetime, mobility and drift velocity for holes and electrons. At implantation doses above  $1.8 \cdot 10^{13} \text{ cm}^{-2}$ , the dark current increased drastically and was comparable to the photocurrent. The increased hopping conductivity [75], [76] due to the larger point defect concentration could be responsible for this behavior. The family of curves in figures 6.3(b), (c) and (d) relates the terahertz power to the photocurrent for a constant laser power. For doses higher than  $1.8 \cdot 10^{12} \text{ cm}^{-2}$  there was a quadratic dependence, as expected from formula 6.1, followed by a saturation component which appeared at lower photocurrents as the frequency increased.



**Fig. 6.3:** (a) I-V curves at different implantation energies and doses measured at RT. The photocurrent has been calculated from the measured current under illumination by subtracting the dark current. This operation was necessary only for samples with doses above  $10^{13}$  ions/cm<sup>2</sup> since, for lower doses, the dark current was negligible (under  $10 \mu$ A for all bias voltage conditions). In (b), (c) and (d) the terahertz power as a function of the photocurrent is represented. NOTE: the noise floor of our terahertz power detector was  $\sim 0.4$  nW.

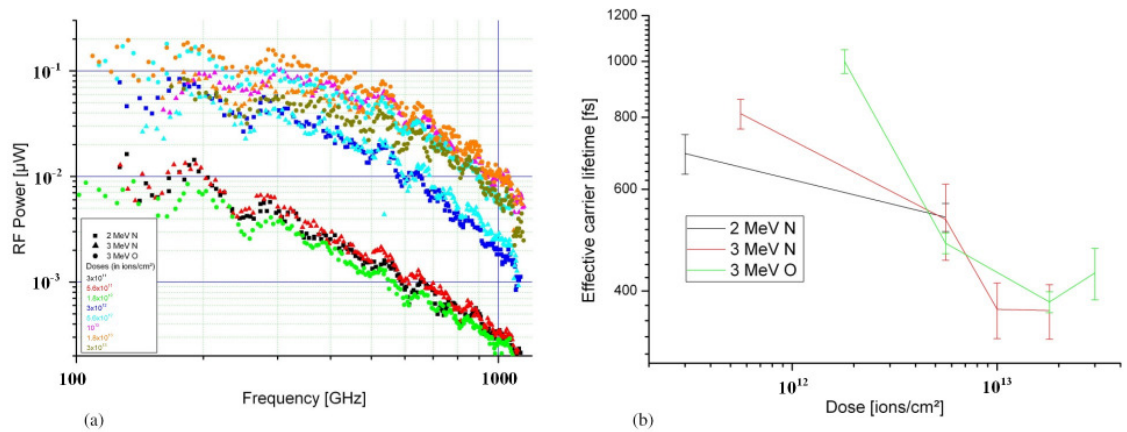


**Fig. 6.4:** (a): rf power versus frequency for different doses and energies. The bias voltage was 3 volts and the photocurrent  $250\mu A$ . (b): By fitting the theoretical curve 6.1 to the data from (a), the effective carrier lifetime was estimated. The fits were calculated for a MSM structure capacity of  $1.5fF$  yielding a 3 dB bandwidth of 1.45 THz for the RC constant.

According to Reklaitis et al. [77] an electron saturation velocity enhancement is expected for samples with smaller electron lifetime. This effect would explain why the super-linear increase in DC photocurrent with voltage (due to both electrons and holes) does not lead to a super-quadratic increase of terahertz power, which is mainly due to electron photocurrent: the increased electron lifetime was counter-acted by a reduced electron saturation velocity, so that the net effect was a saturation of the electron photocurrent. Higher frequencies are affected by the saturation mechanism at lower photocurrents because the influence of the carrier lifetime in the power-attenuating factor from formula 6.1 is frequency dependent. Thus, for high frequencies and low currents, even small changes in the carrier lifetime due to the increase of carrier lifetime with voltage may attenuate considerably the power.

For the high average electric field conditions (up to  $100KV/cm$ ) in the interdigitated region, electron scattering into the L and X valleys might occur. Nevertheless, scattering with electron traps and other defects probably occurs before electrons reach enough kinetic energy for inter-valley scattering.

The frequency response (fig 6.4(a)) of photomixers for a constant bias voltage of 3 volts was measured and the laser power was adjusted so that the photocurrent was similar in all photomixers ( $250\mu A$ ). By this procedure we held the numerator of Eq. 6.1 constant for all samples so that we could directly compare the terahertz power between different doses and extract the recombination lifetime by a fit to the measured data (fig 6.4(b)).

Note that adjusting the voltage instead of laser power to achieve the same



photocurrent in all photomixers have allowed comparison of curves but would not be representative since the carrier lifetime of every individual photomixer would have been altered according to the applied voltage. The trend shows that the higher the dose, the higher the terahertz power for the same DC photocurrent, which is related to the reduced carrier lifetime. Nevertheless there is a limit to the maximum implantation dose since above  $10^{13} \text{ cm}^{-2}$  the dark current increased dramatically whereas, due to the reduced mobility and lifetime, the photocurrent diminished. For example, the dark current at a dose equal to  $3 \cdot 10^{13} \text{ cm}^{-2}$  accounted for  $\sim 30\%$  of the total current and we had to raise the optical power to 100 mW, which was the device burn-out point, to maintain the same photocurrent as for the rest of the samples.

From these measurements we conclude that implanting nitrogen and oxygen ions at energies of 3 MeV and doses around  $10^{13} \text{ cm}^{-2}$  achieves a compromise between dark current, photoconductivity and bandwidth. The carrier lifetime and rf power have been shown to be slowly varying functions of the fabrication conditions, without showing any abrupt dependencies as occurs with of LT-GaAs. This, combined with the excellent control of energy and dose during implantation allows to fabricate a highly reproducible photoconductive material. The reported THz power performance of ion-implanted photomixers is comparable and even superior to the best results achieved with LT-GaAs [78]. Currently devices showing an rf power exceeding  $1 \mu W$  at 1 THz could be demonstrated.



# Chapter 7

## Terahertz photonic mixers as local oscillators for SIS and HEB receivers.

### 7.1 Introduction

A successful pump experiment of two astronomical heterodyne receivers, a superconductor-insulator-superconductor (SIS) receiver at 450 GHz and a hot-electron-bolometer (HEB) receiver at 750 GHz has been reported [78]. A low-temperature-grown GaAs<sup>1</sup> (LT-GaAs) metal-semiconductor-metal (MSM) photonic local oscillator (LO) was illuminated by two NIR semiconductor lasers, generating a beat frequency in the sub mm range. I-V junction characteristics for different LO pump power levels demonstrate that the power delivered by the photomixer is sufficient to pump an SIS and a HEB mixer. SIS receiver noise temperatures were compared using a conventional solid-state LO and a photonic LO. In both cases, the best receiver noise temperature was identical ( $T_{receiver} = 170K$ ), confirming that no excess noise has been added by the photonic LO. The results presented in this chapter were published in [78].

### 7.2 Motivation

Photomixing has been used for several years as a technique for signal generation in the mm and sub mm range [79]. The huge bandwidth offered by

---

<sup>1</sup>Chronologically, ion-implanted GaAs was developed posteriorly to the experiments shown in this chapter. Due to the superior performance of this material, all posterior experiments for pumping astronomical receivers were performed exclusively with photomixers on ion-implanted GaAs.

a single photomixing device (from DC to several THz) has tremendous potential for various applications such as radio astronomy, THz imaging, high-resolution spectroscopy, medicine, security and defense. The progress made in the fabrication of LT-GaAs has led to carrier trapping times below 1 ps at moderate bias voltages, which is essential for fabrication of photomixers in the THz range. In this chapter we report on photomixing as a LO source for heterodyne detection in radio astronomy. The development is aimed at the integration of a photonic LO in:

- GREAT (the German Receiver for Astronomy at Terahertz Frequencies), which will be a first-generation dual-channel heterodyne instrument for high-resolution spectroscopy aboard SOFIA (Stratospheric Observatory For Infrared Astronomy).
- the high-frequency heterodyne receivers at APEX, the Atacama Pathfinder Experiment.

### 7.3 Mixing experiment with an SIS receiver at 450 GHz

The power performance and noise temperature of our photomixers were verified first with an SIS mixer. Similar pump [80], [81], [82] and noise temperature [82] experiments have already been reported.

It is well known that photomixers have a high internal resistance [83] and thus impedance matching is difficult. For this reason, high radiation resistance antennas are needed. Full-wave dipole antennas show a higher resistance ( $\sim 210\Omega$  on a GaAs substrate) than broadband logarithmic spiral antennas ( $\sim 73\Omega$  on a GaAs substrate). The polarization of a dipole is linear, having the same orientation as the dipole itself, whereas the polarization of a spiral is circular (supposing a photomixer area with dimensions much smaller than the wavelength of the THz signal). Furthermore, the Gaussicity of a dipole is better than that of a spiral antenna. Our SIS mixer was sensitive only to linearly-polarized signals, further favoring the use of a dipole antenna.

In our first experiment, an SIS mixer was pumped with a dipole antenna photomixer (fig. 7.1). Amplitude measurements across the E and H planes showed good Gaussicity and low sidelobes (fig. 7.2).

The SIS junction I-V characteristic of an astronomical heterodyne receiver at 450 GHz is shown in Figure 7.3 for two different LO power pump levels.

With a photocurrent of 0.6 mA and a NIR optical power of 70 mW, the rf power generated was  $0.8\ \mu\text{W}$ , which is a factor three below device burnout at room temperature, so that an acceptable safety margin is available to

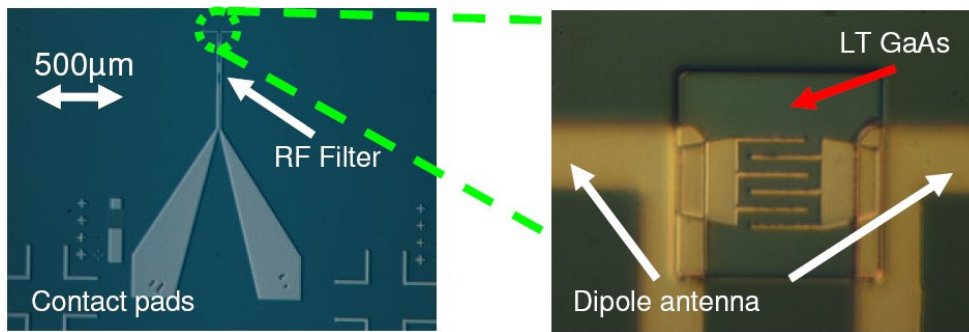


**Fig. 7.1:** Microphotograph of the dipole antenna and finger structure of the photoactive area.

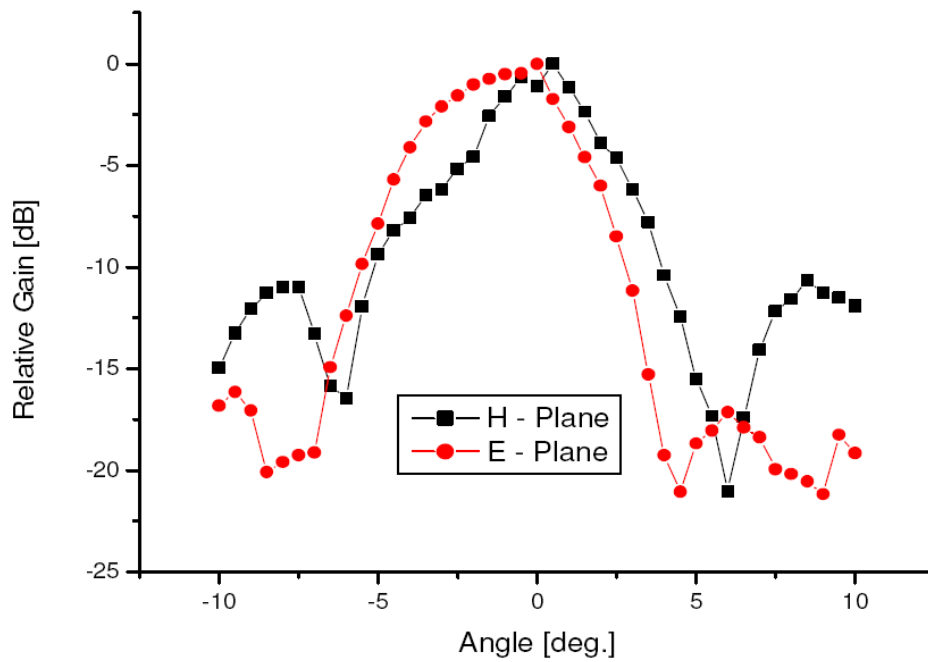


**Fig. 7.2:** E-plane and H-plane power patterns measured for a full wave dipole in resonance at 450 GHz. The high-resistivity Si substrate has a hyperhemispherical form to reduce the divergence of the beam.

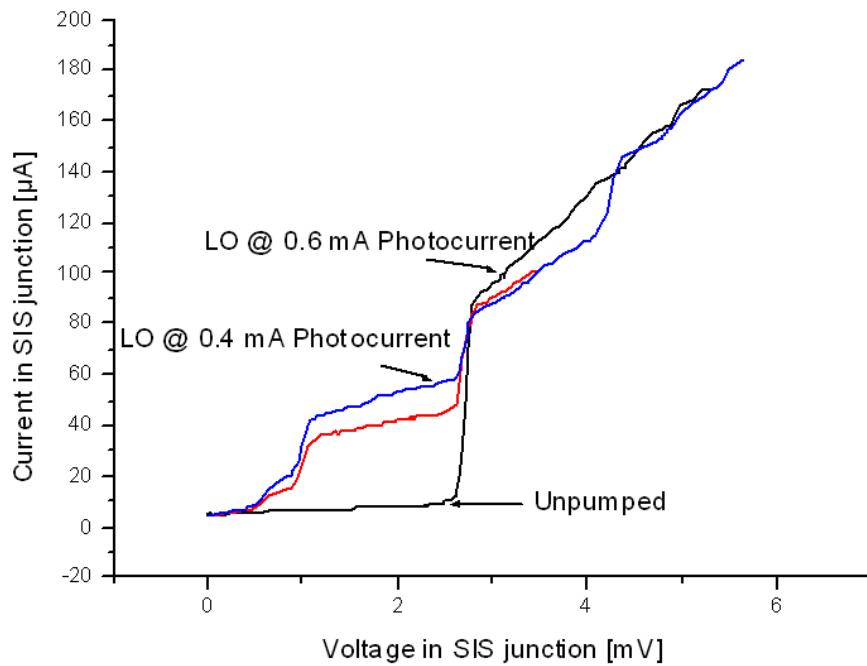


**Fig. 7.3:** The I/V curve of the SIS mixer in absence of LO signal and pumped by a photonic LO signal at 450 GHz for two different LO power levels.

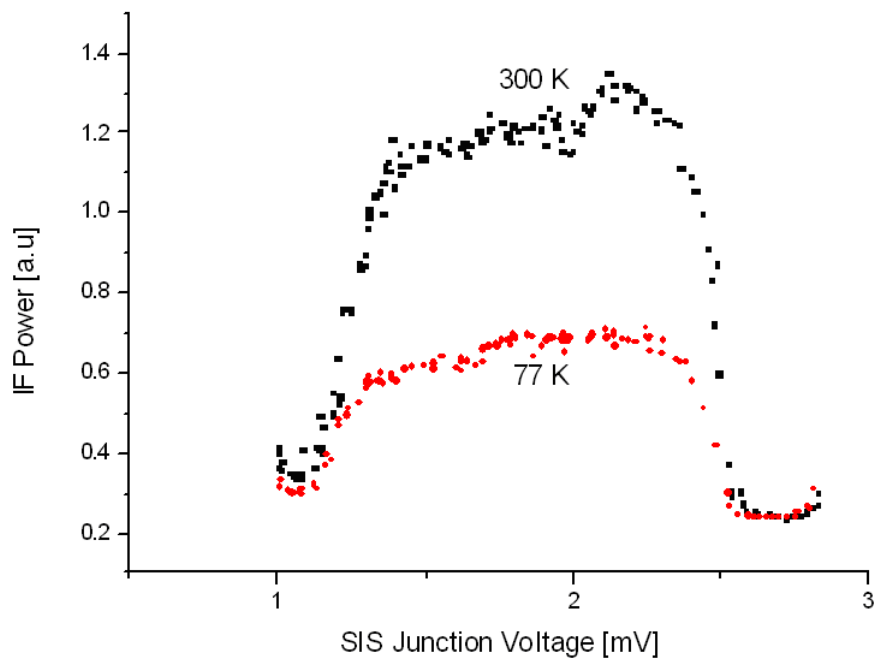


**Fig. 7.4:** Corresponding IF power performance for hot and cold blackbodies.

operate the photonic LO. To investigate whether the photonic LO adds significant internal noise to the mixer, we compared receiver noise temperatures derived from hot and cold measurements using a conventional solid-state LO and the photonic LO. A Martin-Puplett (MP) diplexer was used to inject the LO signal into the signal path. The divergent beam from the MP diplexer output was transformed to a convergent beam with a plane-convex Teflon lens. The double sideband (DSB) noise temperature of the astronomical receiver pumped by the photomixer and by the solid state LO (both measured at an intermediate frequency band of 2 GHz to 4 GHz) were identical ( $T_{receiver} = 170$  K). In contrast to cascading multipliers, the noise contribution of a photonic LO is not expected to increase with frequency because the THz signal is directly generated by optical mixing of two laser signals, a process which is frequency independent.

## 7.4 Mixing experiment with a HEB at 750 GHz

The HEB consisted of a  $NbTiN$  bridge on a  $Si_3N_4$  membrane with dimensions approximately  $4 \times 0.4 \times 0.004 \mu m^3$ . The design frequency was 750 GHz. At this frequency no resonant antenna photomixer device was available, so a photomixer with an integrated logarithmic spiral antenna was used.

The membrane waveguide HEB mixer used for the experiment was sensitive to vertical polarization. The beam waist position was located at the dewar window. To optimize the design of the quasi-optical coupling, the beam parameters of the photomixer beam were determined previously. For this purpose, a power detector (Golay Cell) was installed on a computer-controlled motorized translation stage. The THz beam was scanned bidimensionally, varying the position of the Golay cell over a matrix of  $30 \times 30$  pixels. This process was repeated at different positions to obtain the beam diameter dependence on distance. By fitting the experimental beam diameters to a theoretical Gaussian-beam propagation, the beam waist,  $\omega_0$ , was determined to be 3.3 mm (see fig. 7.5). The beam waist of the HEB mixer was similar to the photomixer beam waist, avoiding the need of a Gaussian-beam telescope for matching the HEB and photomixer beam waists.

The immediate problem associated with the use of a spiral antenna is the need of transforming its circular polarization to vertical to match the polarization of the HEB mixer. For this purpose, two MP diplexers were used in the quasi-optical setup (figure 7.6). The first transformed the polarization from circular to linear. The second MP diplexer was used to inject the hot and cold loads for noise temperature measurements. An off-axis paraboloidal mirror with a focal length of 250 mm was positioned at the center of the quasi-optical setup to image the photomixer beam waist into

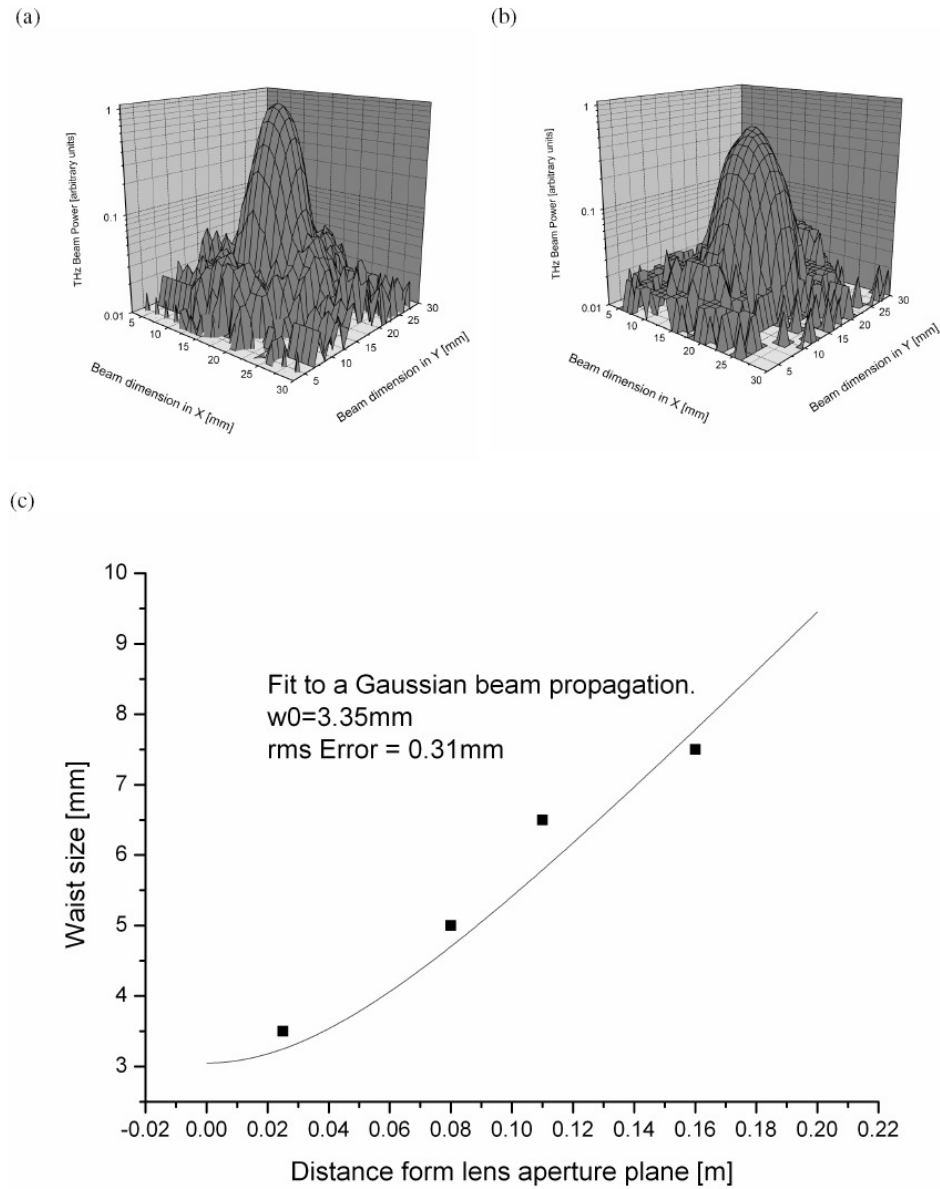


**Fig. 7.5:** (a) and (b) Beam characterization at 50 mm and 110 mm from the lens aperture plane. (c) The waist size of the propagating LO beam was measured at different distances from the photomixer lens aperture plane. The data points were fitted to a Gaussian beam propagation curve. From the fit, the minimum waist (beam waist)  $w_0$  was extracted. The dimensions of the photomixer substrate lens were calculated to synthesize an ellipse. The position of the beam waist coincides with the lens-to-air interface.



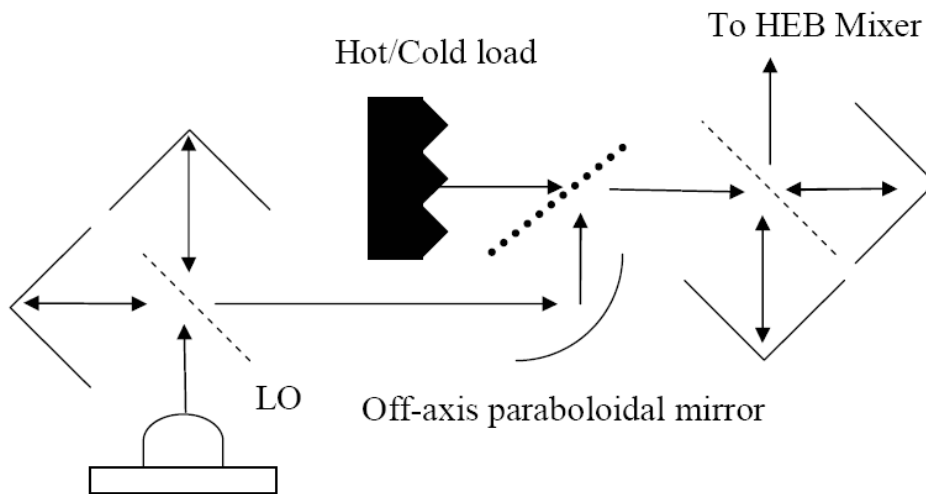


**Fig. 7.6:** Schematic of the quasi-optical setup. A first MP diplexer transforms the circular polarization from the log-spiral antenna photomixer to vertical. The paraboloidal mirror makes the diverging LO beam convergent. The second MP diplexer injects the hot and cold load signal.

the HEB beam waist. The calculated object and image distances were 485 mm.

To assure that beam truncation in the MP diplexers did not play a major role, the ratio between the beam and aperture diameters at the output and input of the MP diplexers was computed and found to be in the worst case  $1/3$ , which represents <sup>2</sup> negligible spillover losses.

Figure 7.7 represents the I-V characteristic of the HEB mixer with and without photonic LO power. The noise temperature measurements were not reproducible due to the standing waves and microphony. Usually HEBs are much more sensitive than SIS mixers to these effects. The photomixer was illuminated by 70 mW of NIR power and the photocurrent was 1.7 mA, generating 450 nW of rf power at 750 GHz, which is near the photomixer burnout point at room temperature. At the output of the quasi-optical system, the rf power was 375 nW, which implies 20 % quasi-optical and water absorption losses. The absorbed rf power in the HEB was calculated using the isothermal method to be 300 nW, which is consistent with the measured power at the input of the HEB dewar.

The same HEB mixer was used in a different experiment pumped with a conventional (frequency-multiplied Gunn oscillator) local oscillator source and showed good heterodyne response ( $T_{receiver}$  as low as 500 K at 750 GHz). The direct detection effects (e.g. by thermal broadband emission)

<sup>2</sup>The edge taper  $Te(dB) = 8.686(r_a/\omega_a)^2 = 78$  dB, where  $r_a$  and  $\omega_a$  represent the aperture radius and beam radius at the aperture plane respectively, describes the truncation of a fundamental mode Gaussian beam. [84]

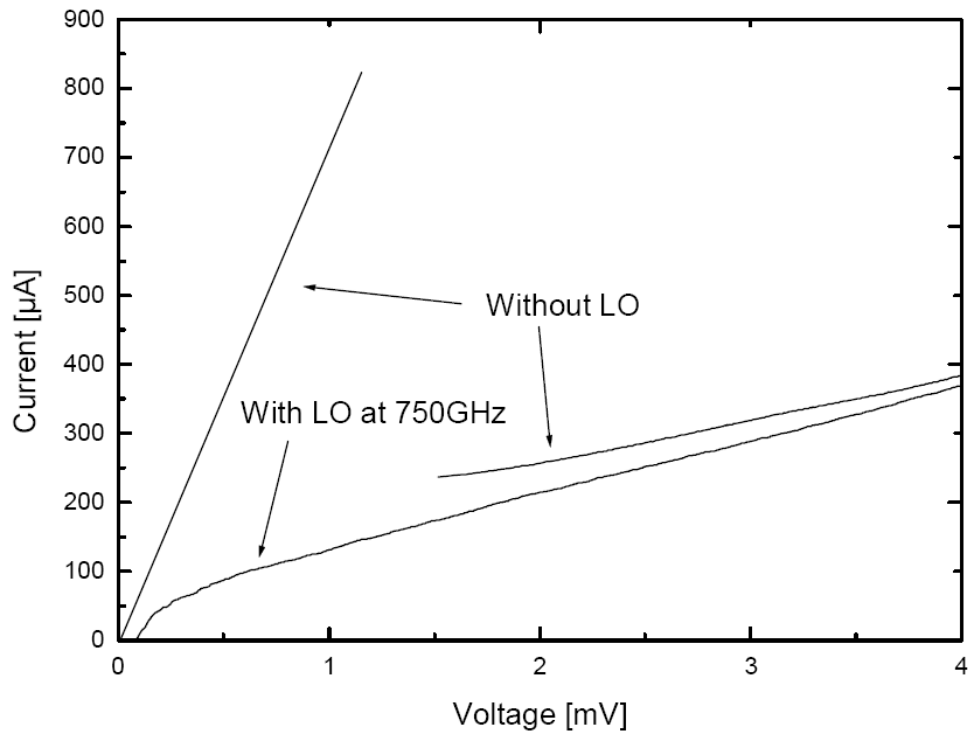


**Fig. 7.7:** The I/V curve of the HEB without LO power and pumped by the photomixer at 750 GHz. The pumped curve has been averaged to eliminate the scatter which resulted from standing waves and microphony. Due to the hysteretic HEB I/V characteristic in the unpumped case, the superconducting branch and the normal conducting branch of the I/V curve are separated. The resistance in the superconducting branch (straight line at left) comes from a series resistance in the bias circuit. When irradiated by the local oscillator power, the HEB I/V becomes non-hysteretic as shown in the lower curve. The difference in current at a given bias voltage between the two curves is proportional to the absorbed local oscillator power.

in this relatively large ( $4 \times 0.4 \times 0.004 \mu\text{m}^3$ ) device embedded in a waveguide are negligibly small compared to the effect seen by the photomixer pumping. The blackbody radiation power of a 300 K source in a 200 GHz bandwidth (which is roughly the rf bandwidth of the mixer) would be only 0.8 nW. This has to be compared to the 300 nW seen as the absorbed rf power of the photomixer in the device.

There is room for rf power improvement by using a full-wave dipole antenna photomixer. In that case, the expected output power would be higher by a factor of three, due to its higher radiation resistance. Also its better Gaussicity and linear polarization would simplify considerably the quasi-optical setup.



# Chapter 8

## Conclusions and future work

The extensive and systematic study carried out on the course of this thesis for the material properties of LTGaAs and ion-implanted GaAs has led to a qualitative advance in the fabrication reproducibility and in the reliability and performance of photomixers. The experience and knowledge gained from the initial material research phase of this work was of prime importance. Optimized photomixers are able to fulfill the demanding requirements of a local oscillator in radio astronomy applications.

This work reports on the first experiment in which a photonic local oscillator has pumped a hot-electron-bolometer receiver. In addition the LO frequency is the highest reported frequency (750 GHz) at which a photonic local oscillator has pumped an astronomical receiver. Noise temperature measurements performed with an SIS receiver at 450 GHz showed a best system noise temperature of 170 K for, both the photonic LO and the solid state LO pumping.

Next, we will push our experiments to even higher frequencies using SIS and HEB mixers operated at 1.05 THz and 2.7 THz respectively. For this purpose, dipole-antenna based photomixers on ion-implanted GaAs were processed with inductive canceling of the finger capacity and with novel MSM structure designs. Measurements performed with these new devices show an rf power exceeding  $1 \mu W$  at 1 THz, which can be further improved ( $\sim 30\%$ ) by using an anti-reflection coating for the high-resistivity substrate lens. A further rf power increase is expected by power combining – photomixer arrays – in cryogenic operation. We expect to push the photomixer breakdown conditions allowing photomixer illumination to higher laser power and bias voltages.

A pioneering experiment is planned using the technology developed in this thesis for the very near future. The photomixer including a laser stabilized setup (see Appendix A) is being integrated in a compact design delivering a local oscillator signal at 1.05 THz. The experiment will be performed at the APEX radio telescope in the Atacama desert, Chile. This novel system will be the first direct photonic local oscillator system for radio astronomical heterodyne receivers in the THz range.



# Appendix A

## Relative frequency stabilization of free-running lasers.

### A.1 Introduction

In order to integrate a photomixer as local oscillator in an astronomical heterodyne receiver, it must fulfil demanding requirements regarding phase noise, linewidth, frequency and power stability. For astronomical applications, when observing atomic/molecular emission lines, it is necessary to obtain velocity resolutions of 100 m/s. Since the velocity distribution of the observed source translates into a frequency distribution due to the Doppler effect, the velocity resolution imposes a limit to the maximum linewidth of the local oscillator signal. As an example, for observations at 1 THz, the linewidth of the local oscillator must not exceed the value:  $\Delta\nu_{LOmax} = V_{resolution}/\lambda_{LO} \simeq 333$  kHz. Consequently, since the photonic local oscillator signal is generated by the beat of two laser modes, these must be stabilized relative to each other. In this chapter special attention is paid to the issue of the frequency stabilization and the available techniques. The concept of a comb generator is described as well as its application for relative frequency stabilization of free running lasers.

### A.2 Motivation for the frequency stabilization of free-running lasers

The emission wavelength of semiconductor lasers is mainly determined by the gain medium and the resonator length. The resonator behaves like a periodic band-pass filter with a transmission function given by the Airy formula. Of course not all wavelengths corresponding to the transmission maxima will be lasing: only those coinciding with the maximum of the laser's gain generate enough stimulated radiation a) to compensate

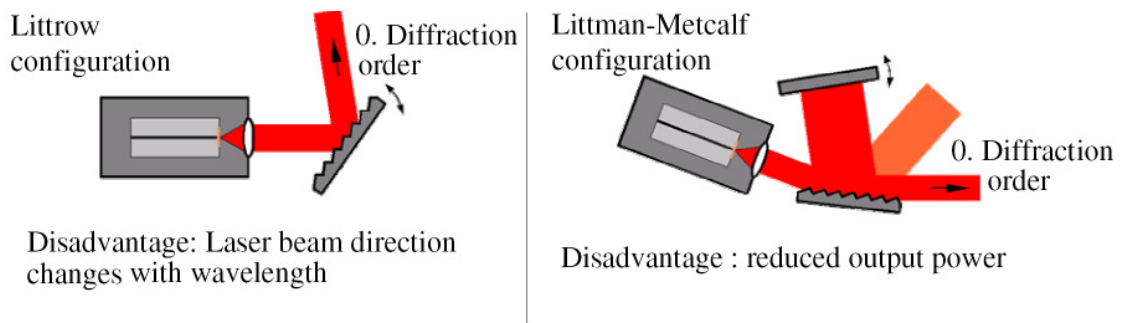


**Fig. A.1:** Schematic of Littman-Metcalf and Littrow external cavity configurations. Taken from [85].

for the round trip losses and b) to compete for the gain of the medium with the other excited modes. In general, semiconductor lasers excite several longitudinal and/or lateral modes simultaneously leading to multi-mode emission. In order to allow single-mode emission, the length of the active medium can be selected so that the variation of the gain curve within one free-spectral range is large enough that one mode gets sufficient gain to suppress the emission of the other modes by mode competition. Another approach to achieve single-mode operation is the use of intra-cavity filters like diffraction gratings. The frequency selective element can be either built coinciding with the active medium – distributed-feedback lasers (DFB) –, attached to the gain medium – distributed Bragg reflector (DBR) – or separated from the laser diode – external cavity configuration. The latter type of configuration allows narrower linewidths. The linewidth of external cavity lasers is dominated by acoustic disturbances on a timescale of seconds whereas the contribution of injection current noise determines the linewidth on milliseconds timescales. There are two widespread external cavity designs, the Littmann-Metcalf and Littrow configurations (see figure A.1). Typical<sup>1</sup> linewidth values of Littmann-Metcalf configurations are  $\lesssim 300$  kHz and  $\lesssim 5$  MHz for 50 milliseconds and 5 seconds timescales respectively. In case of the Littrow configuration<sup>2</sup> the linewidth values for the same timescales were  $\lesssim 1$  MHz and  $\lesssim 10$  MHz respectively.

Since for optical heterodyning, two laser frequencies with their corresponding linewidths are mixed in the photomixer, the spectrum of the mixing signal is the convolution of the impinging laser spectra. A Lorentzian line-shape fits reasonably well to the optical spectrum of the laser signals. Using the convolution theorem, one finds that the beat of two Lorentzian curves is a Lorentzian curve with a linewidth equal to the sum of the original linewidths. This beat signal corresponds to the photocurrent developed at the photomixer (see chapter 2) and, consequently, the linewidth of the photocurrent signal is equal to the sum of the linewidths of both lasers.

<sup>1</sup>Values taken from operation manual of laser model 6312, New Focus

<sup>2</sup>Values for laser model DL100, Toptica. The measurements were performed with a Hfase Burleigh scanning Fabry-Perot etalon



Note that in the far-field the electric field of the local oscillator signal is proportional to the photocurrent. Consequently, the linewidth of the local oscillator signal is the sum of the linewidths of both lasers. Therefore, if we consider the velocity resolution requirement mentioned in the introductory section, the sum of the linewidths of both laser must not be larger than  $333\text{ kHz}$  on the timescale of typical astronomical observations, i. e., minutes or even hours.

Free-running lasers can achieve these linewidths if locked to a reference. The reference can be either a high finesse Fabry-Perot resonator [86] or an optical comb generator. Optical comb generators delivering an absolute frequency reference have been reported [87]. It is important to remark that the linewidth of the mixing signal achieved by two lasers stabilized in frequency relatively to each other is similar to that achieved by two lasers stabilized to an absolute frequency reference. In this work, a relative frequency stabilization scheme based on Kourogi et al.'s comb generator [88] was implemented due to its flexibility, integrability and low cost.

A promising alternative is to generate both optical frequencies within one laser diode. According to the Common-Mode Rejection Effect (CMRE) [89], modes generated inside the same laser cavity are correlated in the way their absolute frequency shifts due to mechanical vibrations, variations of temperature, air pressure, etc. Since in photomixing the relative frequency stability of the laser modes is the linewidth determining parameter, laser systems using this principle benefit from an intrinsic linewidth reduction of the beat signal. This configuration was successfully tested and characterized in the diploma theses of Schmitz [85] at MPIfR and Friedrich [90] (University of Ruhr-Bochum). This concept is currently being optimized for on-field application. Photos from a prototype are shown in figures A.2 and A.3. A similar approach to achieve dual-mode operation with titanium-sapphire lasers was implemented in our group at MPIfR [91] and in collaboration with the University of Leeds [92].

### A.3 The optical comb generator

A comb generator is a device which allows the generation of a set of equally spaced phase coherent sidebands. The optical comb generator conceived by Kourogi et al. consists on a high-finesse Fabry-Perot cavity with an intracavity electro-optic modulator. As photons are coupled into the cavity, they make approximately as many round trips as the value of finesse. If an electro-optic modulator is placed inside the cavity, sidebands are generated. These, in turn circulate and generate additional sidebands. For sufficiently high finesse, the process repeats hundreds of times, giving rise to a comb of optical frequencies (see figure A.4). Since every sideband receives the contribution from many modulated sidebands, a phase condition must hold in order for the interference to be constructive: the

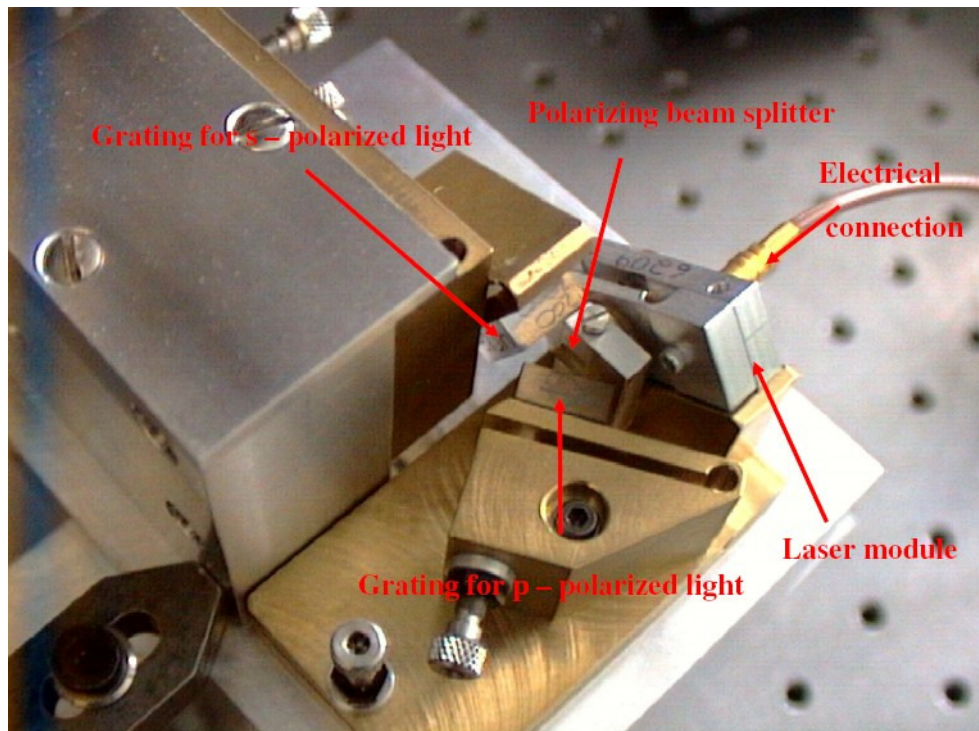


**Fig. A.2:** Photograph of a dual-color laser system prototype. The resonator consists of two cavities -one for the TE and one for the TM mode. A polarizing beam splitter and two blazed diffraction gratings with 1200 lines/mm in a Littrow configuration complete the system. One grating is maintained fixed whereas the other is rotated to generate the frequency difference.

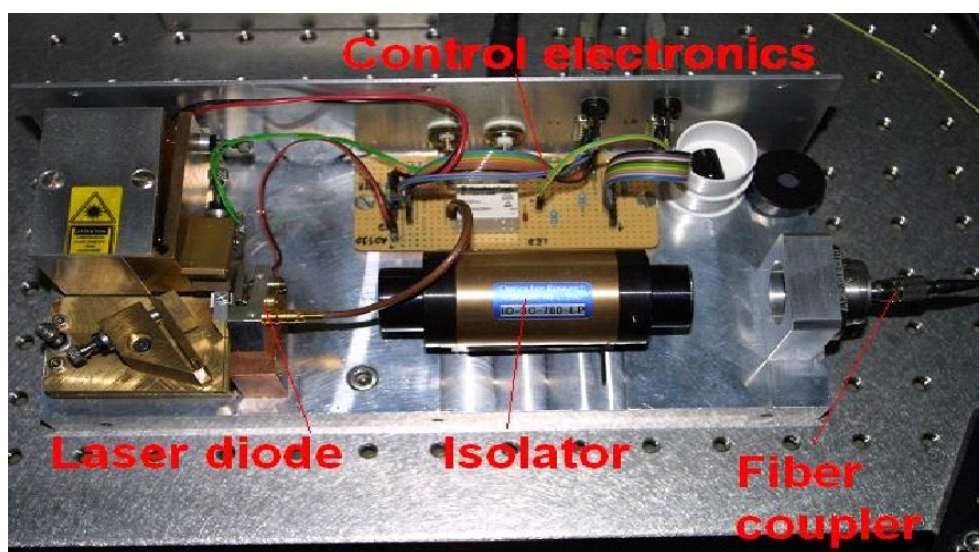


**Fig. A.3:** Photograph of a dual-color laser system prototype. The control electronics, optical isolator and optical fiber coupler are shown.

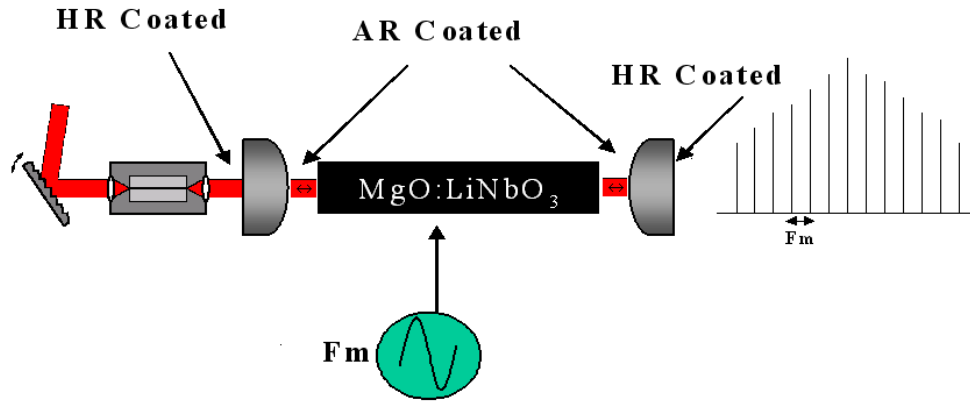


**Fig. A.4:** Schematic view of an optical comb generator. A laser source delivers a single frequency component to a Fabry-Perot resonator with an intracavity phase modulator. As the laser light circulates within the cavity the phase modulator generates a comb of optical frequencies.

free-spectral range of the cavity must be a multiple integer of the modulating frequency. In an optical comb generator, the output power of the  $k$ th comb component is given by [88]:

$$P_k = \eta_{FP} \left( \frac{\pi}{2\beta F} \right)^2 e^{-\frac{|k|\pi}{\beta F}} P_i \quad (\text{A.1})$$

where  $\beta$  is the index of modulation,  $F$  the finesse,  $\eta_{FP}$  the efficiency of the cavity and  $P_i$  the input power.

It is of interest to maximize the comb width, therefore the finesse and index of modulation should be as high as possible. It should be mentioned that the ultimate comb width is determined by the dispersion of the electro-optic material. According to calculations the maximum material dispersion limited comb width is 7.6 THz [93]. The drawback of a high finesse is that the coupling efficiency diminishes. A large index of modulation means a high microwave power. Microwave powers of several watts can be applied, nevertheless due to the loss tangent of the electro-optic crystal at the modulation frequency, part of the applied power is converted into heat, which cause thermal expansion of both the crystal and modulator. This modifies:

- the effective length of the Fabry-Perot cavity. This can be overcome by the use of an active stabilization loop.
- the dimensions of the resonant microwave cavity. This leads to impedance mismatch between the microwave amplifier and the modulator. As a consequence, the power delivered to the modulator diminishes and so does the heating power. As the heating power is reduced, the dimensions of the microwave cavity change again: a cyclic process is established. It is helpful to build a passive temperature stabilization system of the microwave cavity in order to overcome this issue.

## A.4 The electro-optic modulator

In an electro-optic modulator, an external electric field induces a variation in the refraction index of a medium. This process is caused by the second-order non-linear susceptibility,  $\chi^{(2)}$ , and is known as the Pockels effect or linear electro-optic effect. For a given electric field,  $E$ , the variation of the refraction index is given by:

$$\Delta n = 0.5n_e^3 r_{33} E \quad (\text{A.2})$$

where  $n_e$  is the extraordinary index of refraction and  $r_{33}$  is the corresponding element of the third-rank electro-optic tensor.

In case an optical signal passes through a crystal of length  $l$  it experiences a phase shift given by the expression:

$$\Delta\phi = \frac{2\pi}{\lambda} (0.5n_e^3 r_{33}) El \quad (\text{A.3})$$

If both the polarization of the optical signal and microwave signal coincide with the z-axis of the crystal, the index of modulation is maximum. In case that the optical polarization and z-axis are not correctly aligned, the phase modulator might impose a rotation of the polarization which can eventually lead to undesirable amplitude modulation by the optical components next to the comb generator.

The electric field is usually applied by coupling a microwave signal into the electro-optic medium via an electric probe. The time-dependent electric field causes a time-dependent refraction index and when an optical signal passes through the crystal it experiences a time-dependent retardance. In other words, the optical signal suffers a phase modulation.

A widespread design of an electro-optic modulator consists on a non-centrosymmetric crystal like lithium niobate ( $\text{LiNbO}_3$ ) mounted within a resonant microwave cavity. The large frequency difference between the microwave and optical signals leads to considerably different phase velocities. This means that the crystal length cannot be made indefinitely large in order to achieve an acceptable modulation index. In fact, the maximum interaction length for a  $\text{Li:NbO}_3$  phase modulator is approximately 2 mm [94]. This difficulty can be circumvented by using a cut-off waveguide coupled resonator [95]. From microwave theory it is well known that the dispersion curve of a waveguide next to the cutoff frequency the phase velocity displays large variations with frequency [43]. For a certain band of frequencies matching of the microwave and optical phase velocities can be achieved, enabling larger interaction lengths between microwave and optical signals. In addition, the use of a resonant cavity with a high Q factor enhances the microwave electric field, so that a lower input microwave power is sufficient to operate the phase modulator.

A self-made phase modulator was built with a  $\text{MgO:LiNbO}_3$  crystal. In order to avoid reflections at the input and output facets, an antireflection

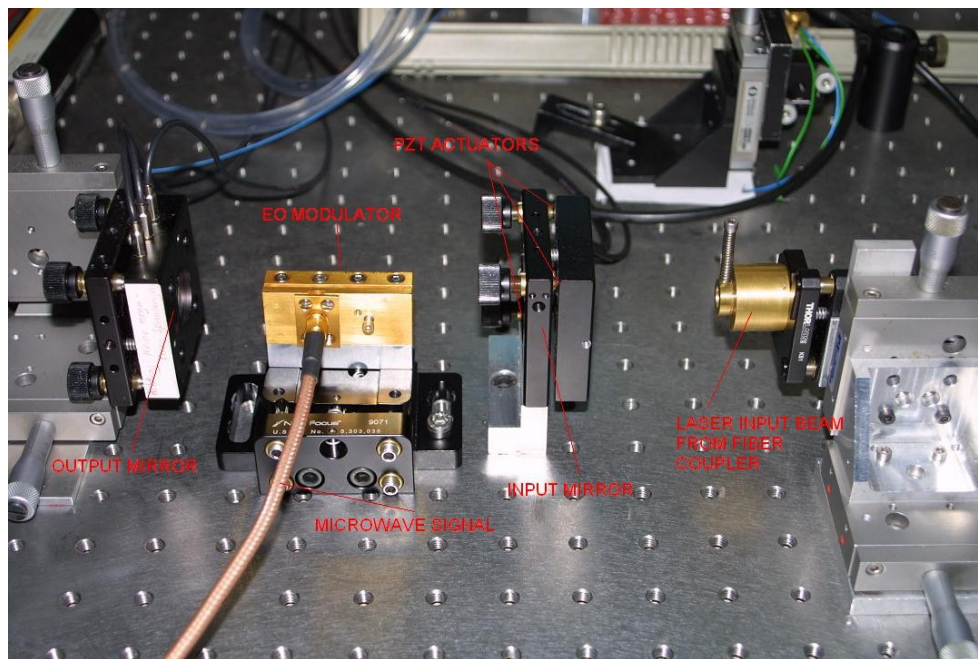


**Fig. A.5:** Photograph of the comb generator. A collimated beam from a fiber-optic is coupled into a high finesse Fabry-Perot cavity. The lenses and piezoelectric actuators can be seen. An SMA cable delivers the microwave power to the phase modulator.

coating was evaporated on both of them. Because of its high thermal conductivity copper was chosen for the microwave resonant cavity. In addition a thin gold layer was evaporated to minimize the surface resistance. Water cooling channels were machined into the copper microwave cavity. This step minimized noticeably the thermally induced instabilities in the complete comb generator system. The crystal was a cuboid filling the center of the rectangular resonant microwave cavity. The dimensions of crystal and cavity were chosen so that the mode  $TE_{106}$  was excited. A microwave oscillator and power amplifier delivered a 9.2 GHz signal with power up to 20 Watt to the phase modulator. A circulator enabled monitoring the reflected power from the cavity. The reflection losses were roughly 20 dB.

## A.5 Measurements with the optical comb

A symmetric Fabry-Perot cavity consisting of plano-convex lenses was built (Figure A.5 shows a photograph with the comb generator). The lenses were coated so that the planar facet had a high-reflective coating, whereas the curved facet was anti-reflection coated. These positive lenses corrected the divergence of the laser beam<sup>3</sup>. The lenses had a focal length of

<sup>3</sup>Due to the length and finesse of the FP cavity, the laser beam travels distances around hundreds of meters. If no divergence correcting element would be placed in the

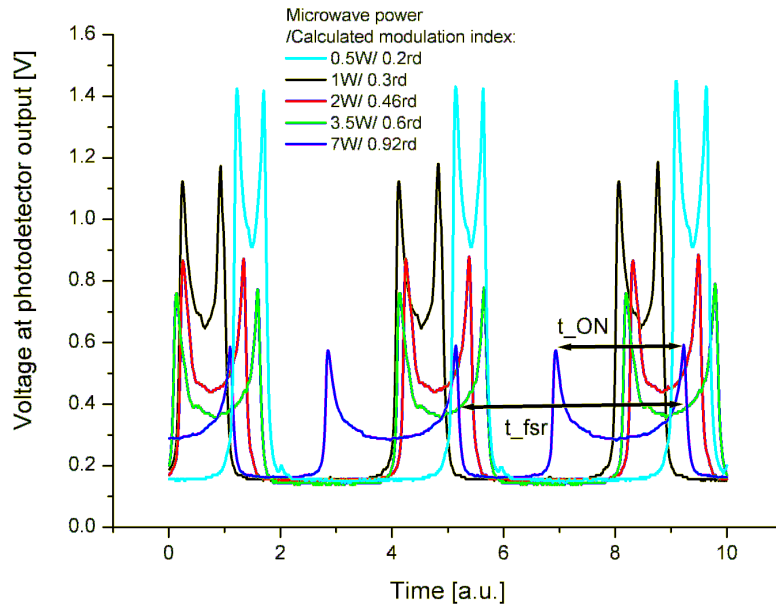


**Fig. A.6:** Scanning Fabry-Perot curve with the phase modulator operating at different microwave powers. The corresponding modulation index is calculated with formula A.6

300 mm and were installed on piezoelectric mounts. The input laser beam was practically  $TEM_{00}$  since it was coupled out of a single-mode fiber optic and beam-matched to the Fabry-Perot cavity with a set of lenses. The laser spot size was around 500 micrometers. A photodetector placed at the output of the cavity delivered a signal proportional to the transmissivity of the F-P cavity, i. e. the Airy function. The length of the Fabry-Perot cavity was 200 mm and the finesse was measured to be 70 and 50 for lenses with reflectivities  $R=98.7\%$  and  $R=96.5\%$  respectively. By scanning the piezo-actuators, the FP resonator transmission curve was visualized in an oscilloscope and the lens mounts were manually adjusted until the lateral modes were suppressed.

The insertion of the modulator in the cavity had no appreciable effect on the finesse. As microwave power was delivered to the modulator, the shape of the signal changed from the Airy function shape, becoming broad and displaying two peaks at both extremes of the curve<sup>4</sup> Figure A.6 shows this signal for different microwave powers.

The reason for the observed shape of the curve is not trivial but can be completely elucidated using the steady-state mode-coupled solution for the "FM laser" [96]. The output electric field of the comb generator can be

cavity the laser beam could not interfere correctly reducing the overall cavity finesse.

<sup>4</sup>Anecdotic comment: Due to the similarity between the shape of the signal and the Cologne cathedral, the signal was named "das Kölsche Signal", "the Cologne signal".

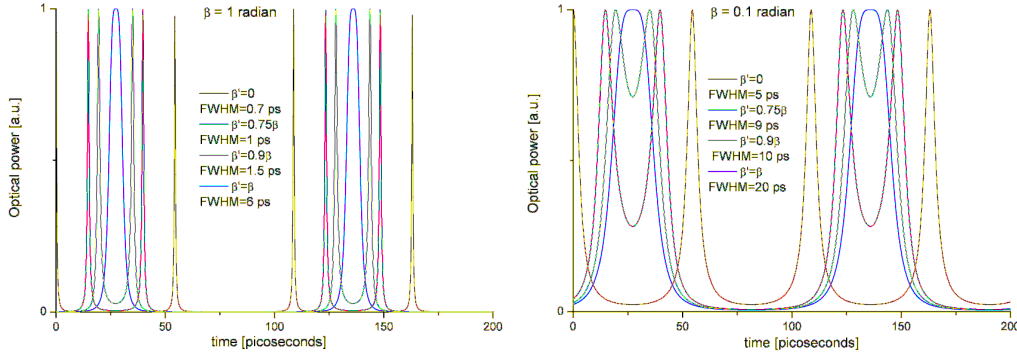


**Fig. A.7:** Calculated time dependent optical power at the output of the comb generator for two different modulation indexes. For the same detuning parameter  $\beta'$  pulses in the graph with larger modulation index display smaller pulse width. As the detuning parameter  $\beta'$  gets larger the pulse width increases and neighboring pulses begin to merge. Formula A.4 was used for calculations. In the curves only the "slowly" varying part of the optical power is represented, i. e. the envelope of the optical power variations. The modulating frequency was 9.2 GHz

expressed as [93]:

$$E_0(t) = \Re e \left[ \sqrt{\eta_{FP}} \frac{E_i \exp(i2\pi\nu_{carrier}t)}{1 + i2\beta'F/\pi + i2\beta F/\sin(\omega_m t)\pi} \right] \quad (\text{A.4})$$

where  $E_i$  and  $\nu_{carrier}$  are the amplitude and frequency of the input electric field,  $\omega_m$  is the modulating angular frequency,  $\beta$  is the single pass modulation index of the phase modulator and  $\beta'$  is the detuning parameter, which is related to the relative frequency detuning between optical carrier and nearest cavity mode:

$$\beta' = \frac{\pi(\nu_{carrier} - \nu_{cavity})}{FSR} \quad (\text{A.5})$$

It is interesting to analyze the output optical power in the time domain for different modulation indexes and detuning parameters. The effect of these parameters can be seen in Figure A.7. A first impression is that the comb generator behaves as an ultrafast optical chopper. The input CW laser signal is transformed into a pulsed signal, whose pulse width is directly related to the modulation index. This is logical since for a higher modulation index a broader spectrum is expected. As a consequence of the scaling property according to Fourier transform theory, the signal in the time domain gets narrower, i. e. the pulse width is reduced. The effect of the detuning parameter is a) to increase the pulse duration and b) to merge neighboring pulses.

The cavity length is changed as the PZTs are scanned, consequently  $\beta'$  and the output electric field change as described by equation A.4. Therefore, if the output optical power is represented as a function of  $\beta'$ , one

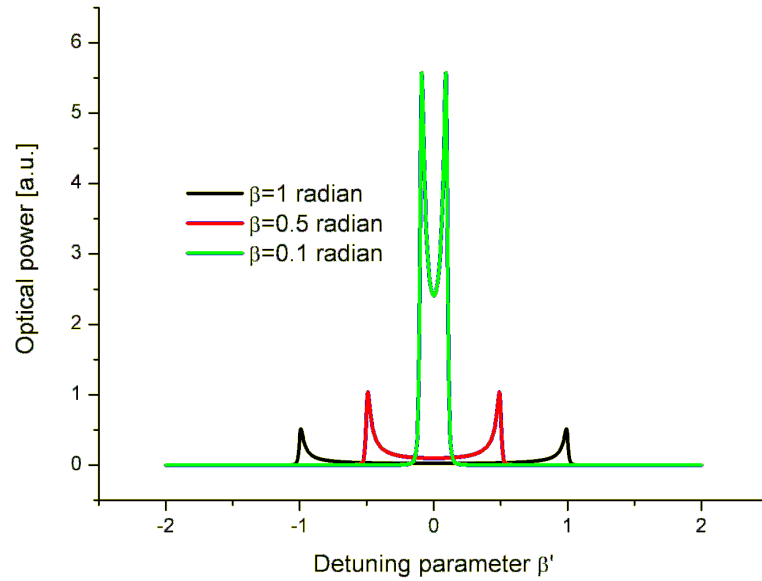


**Fig. A.8:** Calculated time-averaged optical power as a function of the detuning parameter  $\beta'$ .

should expect the same results as those experimentally obtained by varying the PZTs. As can be seen in figure A.8, the shape of the scanning FP curve of figure A.6 can be perfectly reproduced.

$\beta$  can be empirically determined from figure A.6 with the formula [97]:

$$\beta = \frac{\pi t_{on}}{2t_{FSR}} \quad (\text{A.6})$$

where  $t_{on}$  and  $t_{FSR}$  indicate the temporal duration of the signal and that corresponding the free spectral range – see arrows in figure A.6. According to Kouroggi et al. [93], the maximum comb width is given by:

$$\Delta\nu_{max} = \sqrt{\frac{2(\beta - \beta')M}{\pi}} \quad (\text{A.7})$$

$M$  is a parameter inversely proportional to the group velocity dispersion in the medium (GVD<sup>5</sup>) and length of the crystal ( $L_{crystal}$ ): [97]:

$$M \approx \frac{1}{L_{crystal}GVD} \quad (\text{A.8})$$

A compromise between signal-to-noise ratio and comb width is achieved for  $\beta' = 0$ . This condition is fulfilled at the center of the "Cologne" signal,

<sup>5</sup>GVD= $v_{group}^{-2} \frac{dv_{group}}{d\omega}$ , being  $v_{group}$  the group velocity. Using the Sellmeier equations for MgO:LiNbO<sub>3</sub> at 780 nm yields  $GVD = 3670 fs^2 cm^{-1}$



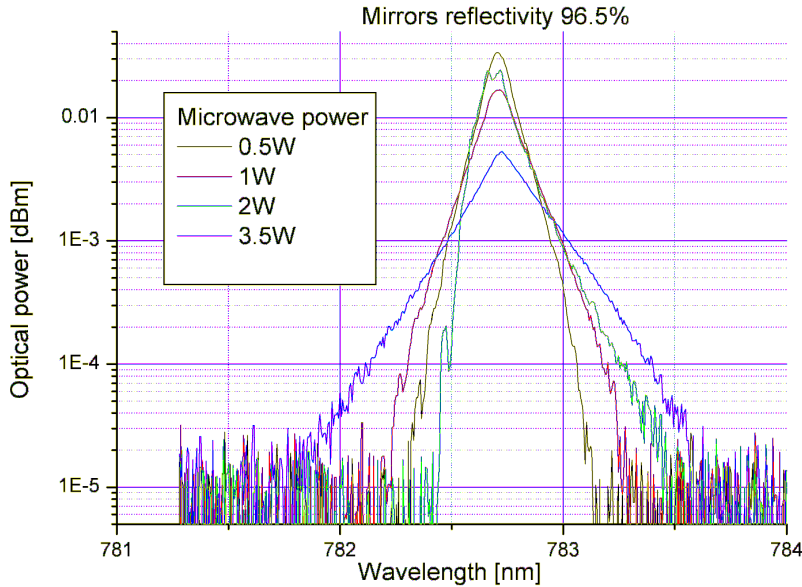


**Fig. A.9:** Spectrum of the comb generator for lenses with reflectivity  $R=96.5\%$  for different microwave powers.

giving a theoretical maximum comb span of 6.5 THz for a microwave power of 7 Watts.

The output of the comb generator was coupled to an optical spectrum analyzer. Measurements were performed at different microwave powers and with lenses having a reflectivity  $R = 98.7\%$  and  $R = 96.5\%$ . The corresponding results are shown in figures A.9 and A.10. The larger reflectivity of the lens results in a higher finesse and consequently the comb spectrum became broader. Unfortunately when using lens with high reflectivity the peak transmission drops dramatically due to the surface accuracy of the lens. Therefore although the finesse of the FP cavity can be increased by choosing lenses with higher reflectivities, the larger finesse is at the expense of the coupled optical power [98]. A practical comb generator should not include lenses with reflectivities larger than  $R > 99.5\%$ .

As can be seen the power roll-off for the measurement at 3.5 Watts from figure A.10 is approximately 16dB/nm. According to formula A.1 the power roll-off per nanometer <sup>6</sup> is

$$\exp\left(-\frac{\pi 500/9.2}{\beta F}\right) \equiv 17.6\text{dB/nm} \quad (\text{A.9})$$

which is consistent with the experimental value.

In order to maintain the condition  $\beta' = 0$  either the laser frequency  $\nu_{carrier}$  or the nearest-cavity mode  $\nu_{cavity}$  can be tuned. In the present work  $\nu_{cavity}$

<sup>6</sup>At 780 nm wavelengths one nanometer is equivalent to 500 GHz. Note that the operating frequency of the phase modulator is 9.2 GHz.

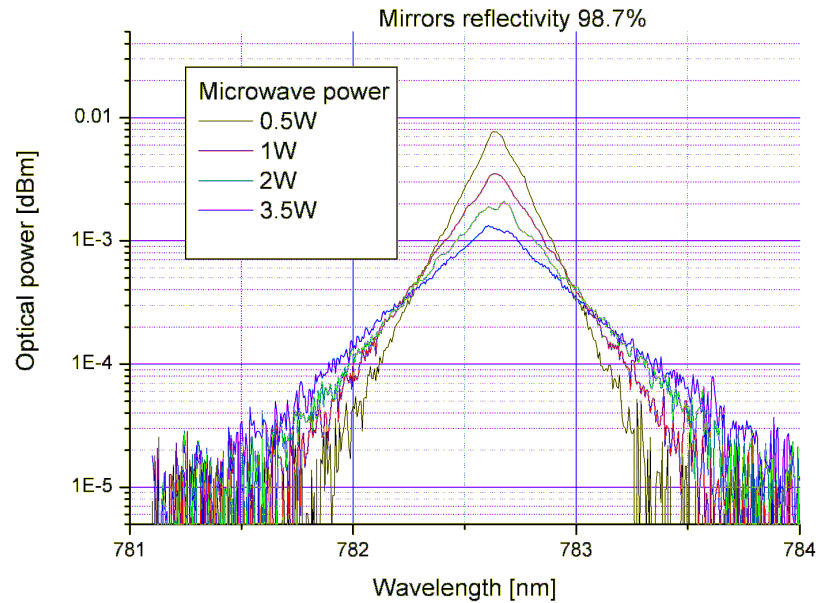


**Fig. A.10:** Spectrum of the comb generator for lenses with reflectivity  $R=98.7\%$  for different microwave powers.

was tuned by minimally changing the Fabry-Perot cavity length via the piezoelectric actuators on which the lenses were mounted.

Locking the FP cavity to  $\beta' = 0$  requires the generation of an error signal. In the frequency domain, the comb consists of a set of periodic sidebands. These result in a set of periodic pulses in the time domain. The temporal pulse width relates to the inverse of the comb width whereas the repetition rate of the pulses relates to the inverse of the frequency separation between the comb components. If a fast photodetector is placed at the output of the comb generator, it generates a frequency component coinciding with the repetition frequency of the periodic pulse train, i. e. the microwave frequency which drives the electro-optic modulator. This component has the necessary information in its phase for locking the cavity to  $\beta' = 0$ . Therefore, the photodetector signal was phase-detected in a harmonic mixer taking the microwave oscillator signal as reference. The output of the phase detector was the required error signal for locking the F-P cavity. A PID circuit generated the feedback signal which was delivered to the piezoelectric actuators thereby modifying the length of the FP cavity. With this procedure [93] the FP cavity could be locked to the  $\beta' = 0$  condition for hours.

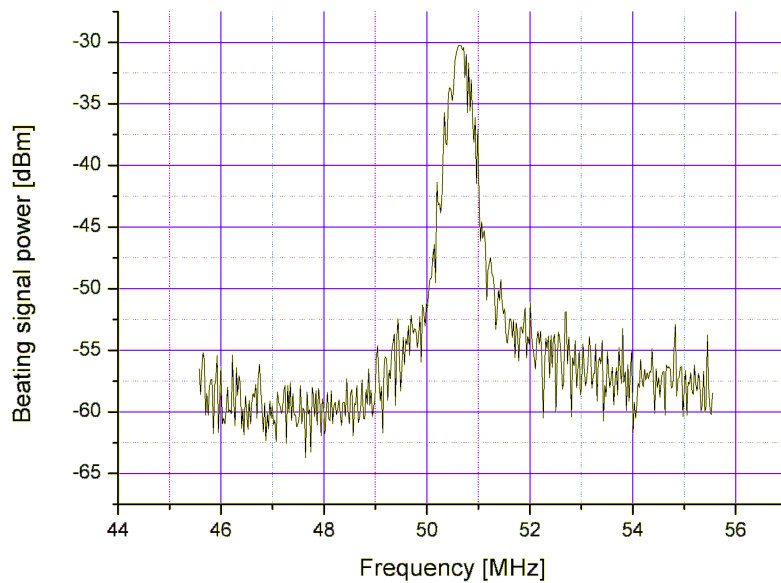


**Fig. A.11:** Spectrum of beat signal under frequency-locked condition. 10 MHz span, 20 ms sweep time, 30 kHz resolution.

## A.6 Relative frequency stabilization with a comb generator

Once the FP cavity was locked, the next step was to stabilize the frequency of a free-running laser (laser A) to the desired comb component generated by a second free-running laser (laser B). Due to the imminent use of a complete photonic system as a local oscillator at the APEX telescope in the Atacama desert (Chile), the measurement results shown hereinafter were performed at the corresponding frequency band of astronomical interest, i. e. the 1.05 THz atmospheric window.

Due to the low power available for the comb component 1.05 THz apart from the optical carrier – 128<sup>th</sup> comb component –, the beat signal between optical comb and laser A was generated in an avalanche photodetector<sup>7</sup> and amplified in order to drive a frequency-to-voltage converter, which delivered an error signal for a 50.5 MHz set-point. The error signal was processed in a PID and delivered the PZT (slow) and current (fast) feedback signals to the laser A. This scheme alone served to provide a large frequency stabilization range (100 MHz) but did not allow to narrow the beat signal to values better than 1 MHz. Figure A.11 shows the spectrum of the beat signal under the frequency-lock condition

In order to narrow the linewidth, a phase-locking scheme was imple-

<sup>7</sup>MenloSystems, APD-210

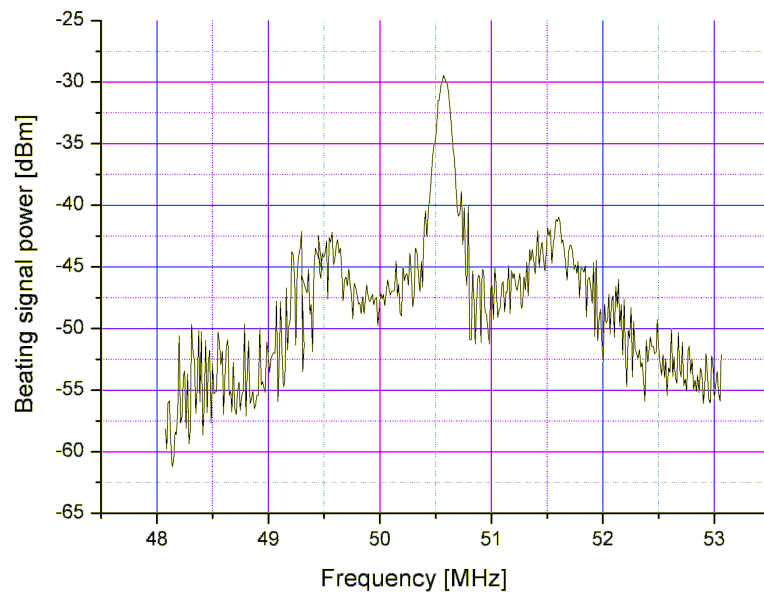


**Fig. A.12:** Spectrum of the beat signal under phase-locked condition. 5 MHz span, 20 ms sweep time, 30 kHz resolution.

mented. A signal generator delivered a reference at the set point frequency whose phase was compared with that of the beat signal in a phase detector (balanced harmonic mixer). The output of the phase detector was directly applied to the high-speed modulation input of laser B. As a result, the linewidth of the beat signal could be narrowed to less than 100 kHz (3dB linewidth, see figure A.12), thereby fulfilling the requirements for a local oscillator on application in radio astronomy. The shape of the spectrum under the phase-locked condition is similar to others reported in the literature [99].

## A.7 Conclusions and future work

The demonstration in the laboratory of relative frequency stabilization between two semiconductor lasers using a comb generator establishes the experimental basis for designing a complete laser stabilized system for field operation. Currently, a compact, robust laser system is being built with the aim of delivering a narrow linewidth, frequency stable LO signal in the 1.05 THz band. The input and output facets of the MgO:LiNbO<sub>3</sub> crystal have been polished and coated (HR). The aim is to construct a bulk comb generator with higher finesse and coupling efficiency. The external-cavity lasers will be substituted by DBR lasers, due to their smaller size, higher power and better integrability.

# Bibliography

- [1] B. J. McMurry and A. E. Siegman. *Appl. Optics*, 51, 1962.
- [2] B. J. McMurry. PhD thesis, Stanford University.
- [3] Javan. Frequency characteristics of continuous-wave He-Ne optical maser. *J. Opt. Soc. Am.*, 52:96, 1962.
- [4] T.H. Maiman. Stimulated optical radiation in ruby. *Nature*, 187(4736):221–230, 1960.
- [5] E. R. Brown. Thz generation by photomixing in ultrafast photoconductors. *International Journal of High Speed Electronics and Systems*, 13:497–545, 2003.
- [6] Wei Shi and Yujie J. Ding. Continuously tunable and coherent terahertz radiation by means of phase-matched difference-frequency generation. *Appl. Phys. Lett.*, 83:848, 2003.
- [7] E. A. Michael, B. Vowinkel, R. Schieder, M. Mikulics, M. Marso, and P. Kordos. Large-area traveling-wave photonic mixers for increased continuous terahertz power. *Appl. Phys. Lett.*, 86:120–123, 2005.
- [8] G. H. Doehler, F. Renner, O. Klar, M. Eckardt, A. Schwanhaeusser, S. Malzer, D. Driscoll, M. Hanson, A. C. Gossard, G. Loata, T. Loeffler, and H. Roskos. Thz-photomixer based on quasi-ballistic transport. *Semicond. Sci. Technol.*, 20:178–190, 2005.
- [9] T. Noguchi, A. Ueda, H. Iwashita, S. Takano, Y. Sekimoto, M. Ishiguro, T. Ishibashi, H. Ito, and T. Nagatsuma. Millimeter wave generation using a uni-traveling-carrier photodiode. *ALMA Memo 399*.
- [10] D. Saeedkia, R. R. Mansour, and S. Safavi-Naeini. Modeling and analysis of high-temperature superconductor terahertz photomixers. *IEEE Trans. Appl. Superconduct.*, 15(3), 2005.
- [11] M. Tonouchi, M. Tani, Z. Wang, K. Sakai, S. Tomozawa, M. Hangyo, Y. Murakami, and S. Nakashima. *Jpn. J. Appl. Phys.*, 35:2624, 1996.

- [12] Andreas Stöhr, Andrei Malcoci, Andres Sauerwald, Iván Cámara Mayorga, Rolf Güsten, and Dieter Stefan Jäger. Ultra-wide-band traveling-wave photodetectors for photonic local oscillators. *Journal of Lightwave Technology*, 21:3062–3070, 2003.
- [13] Daryoosh Saeedkia. *Modeling and Design of Photoconductive and Superconductive Terahertz Photomixer Sources*. PhD thesis.
- [14] S. Y. Chou, Y. Liu, W. Khalil, T. Y. Hsiang, and S. Alexandrou. Ultra-fast nanoscale metal-semiconductor-metal photodetectors on bulk and low-temperature grown GaAs. *Appl. Phys. Lett.*, 61:819, 1992.
- [15] E. R. Brown, K. A. McIntosh, K. B. Nichols, and C. L. Dennis. Photomixing up to 3.8 thz in low-temperature-grown GaAs. *Appl. Phys. Lett.*, 66:285–288, 1995.
- [16] Saeedkia Daryoosh, Mansour Raafat R., and Safavi-Naeini Safieddin. The interaction of laser and photoconductor in a continuous-wave terahertz photomixer. *IEEE Journal of Quantum Electronics*, 41:1188–1196, 2005.
- [17] E. R. Brown, F. W. Smith, and K. A. McIntosh. Coherent millimeter-wave generation by heterodyne conversion in low-temperature-grown GaAs photoconductors. *J. Appl. Phys.*, 73:1480–1484, 1993.
- [18] E. A. Michael, I. Cámara Mayorga, R. Güsten, A. Dewald, and R. Schieder. Terahertz continuous-wave large-area traveling-wave photomixers on high-energy low-dose ion-implanted GaAs. *Applied Physics Letters*, 90:1109–+, April 2007.
- [19] Duffy S.M., Vergheese S., McIntosh A., Jackson A., Gossard A.C., and Matsuura S. Accurate modeling of dual dipole and slot elements used with photomixers for coherent terahertz output power. *IEEE Trans. Microwave Theory and Tech.*, 49:1032–1038, 2001.
- [20] A. Reklaitis, A. Krotkus, and G. Grigaliunaite. Enhanced drift velocity of photoelectrons in a semiconductor with ultrafast carrier recombination. *Semiconductor Science and Technology*, 14:945–947, 1999.
- [21] M. D. Sturge. *Phys. Rev.*, 127:768, 1962.
- [22] Martin Eckardt. *Aspects of high field carrier transport in AlGaAs*. PhD thesis, Friedrich Alexander Universitaet Erlangen Nuernberg, 2003.
- [23] J. S. Blakemore. Semiconducting and other major properties of gallium arsenide. *J. Appl. Phys.*, 53(10):123–181, 1982.
- [24] H. J. Bakker, G. C. Cho, H. Kurz, Q. Wu, , and X. C. Zhang. *J. Opt. Soc. Am. B-Opt. Phys.*, 15:1795, 1998.

- [25] I. S. Gregory, C. Baker, W. R. Tribe, M. J. Evans, H. E. Beere, E. H. Linfield, A. G. Davies, and M. Missous. High resistivity annealed low-temperature GaAs with 100 fs lifetimes. *J. Appl. Phys.*, 83:4199, 2003.
- [26] Shockley W. and Read W.T. Statistics of the recombination of holes and electrons. *Phys. Rev.*, 87:835–842, 1952.
- [27] R.N. Hall. Electron hole recombination in germanium. *Phys. Rev.*, 87:387, 1952.
- [28] N. F. Mott and W. D. Twose. *Adv. Phys.*, 10:107, 1961.
- [29] Matthew C. Beard and Gordon M. Turner and Charles A. Schmuttenmaer. Transient photoconductivity in GaAs as measured by time-resolved terahertz spectroscopy. *Phys. Rev. B*, 62(23), 2000.
- [30] D. Grischkowsky T. I. Jeon, A. K. Mukherjee, and R. Meon. *Appl. Phys. Lett.*, 77:2452–2455, 2000.
- [31] M. R. Melloch, N. Otsuka, K. Mahalingam, C. L. Chang, and J. M. Woodall et al. *J. Appl. Phys.*, 72:3509–3513, 1992.
- [32] S. S. Prabhu, S. E. Ralph, M. R. Melloch, and E. S. Harmon. *Appl. Phys. Lett.*, 70:2419–2421, 1997.
- [33] M. O. Manasreh, D. C. Look, K. R. Evans, and C. E. Stutz. *Phys. Rev. B*, 41:272, 1990.
- [34] J. Gebauer, F. Börner, R. Krause-Rehberg, T. E. M. Staab, W. Bauer-Kugelmann, G. Kögel, W. Triftshäuser, P. Specht, R. C. Lutz, E. R. Weber, and M. Luysberg. Defect identification in GaAs grown at low temperatures by positron annihilation. *Journal of Applied Physics*, 87:8368–8379, June 2000.
- [35] X. Liu, A. Prasad, W. M. Chen, A. Kurpiewski, A. Stoschek, Z. Liliental-Weber, and E. R. Weber. Mechanism responsible for the semi-insulating properties of low-temperature-grown GaAs. *Applied Physics Letters*, 65:3002–3004, December 1994.
- [36] A. Krotkus, K. Bertulis, L. Dapkus, U. Olin, and S. Marcinkevičius. Ultrafast carrier trapping in be-doped low-temperature-grown gaas. *Appl. Phys. Lett.*, 75(21):3336–3338, 1999.
- [37] M. N. Chang, K. C. Hsieh, T.-E. Nee, and J.-I. Chy. *J. Appl. Phys.*, 86:2442–2447, 1999.
- [38] D. C. Look. On compensation and conductivity models for molecular-beam-epitaxial GaAs grown at low temperature. *Journal of Applied Physics*, 70:3148–3151, September 1991.

- [39] M. R. Melloch, N. Otsuka, J. M. Woodall, A. C. Warren, and J. L. Freeouf. Formation of arsenic precipitates in GaAs buffer layers grown by molecular beam epitaxy at low substrate temperatures. *Applied Physics Letters*, 57:1531–1533, October 1990.
- [40] Claverie, Fereydoon Namavar, and Z. Liliental-Weber. Formation of As precipitates in GaAs by ion implantation and thermal annealing. *Appl. Phys. Lett.*, 62:1271–1273, 1993.
- [41] Krotkus, S. Marcinkevicius, J. Jasinski, M. Kaminska, H. H. Tan, and C. Jagadish. Picosecond carrier lifetime in GaAs implanted with high doses of As ions: An alternative material to low-temperature GaAs for optoelectronic applications. *Appl. Phys. Lett.*, 66:3304–3307, 1995.
- [42] R. Winston. Light collection within the framework of geometric optics. *J. Opt. Soc. Amer.*, 60(4):245–247, 1970.
- [43] Robert E. Collin. *Foundations for microwave engineering*. McGraw-Hill.
- [44] Andrew W. Jackson. *Low-temperature-grown GaAs photomixers designed for increased terahertz output power*. PhD thesis, University of California, Santa Barbara, 1999.
- [45] D. B. Rutledge, D. P. Neikirk, and D. P. Kasilingam. *Infrared and Millimeter Waves*, volume 10. Academic, New York, 1983.
- [46] D. F. Filipovic, S. S. Gearhart, and G. M. Rebeiz. *IEEE Trans. Microwave Theory Tech.*, 41:1738, 1991.
- [47] Y.C. Lim and R.A. Moore. Properties of alternately charged coplanar parallel strips by conformal mappings. *IEEE Trans. Electron Dev.*, 15:173–180, 1968.
- [48] D. S. Kim and D. S. Citrin. Efficient terahertz generation using trap-enhanced fields in semi-insulating photoconductors by spatially broadened excitation. *Journal of Applied Physics*, 101:3105–+, March 2007.
- [49] E. R. Weber, H. Ennen, U. Kaufmann, J. Windscheif, J. Schneider, and T. Wosinski. *Journal of Applied Physics*, 53:6140–6143, September 1982.
- [50] Y. H. Chen, Z. Yang, R. G. Li, Y. Q. Wang, and Z. G. Wang. Reflectance-difference spectroscopy study of the fermi-level position of low-temperature-grown gaas. *Physical Review B*, 55:7379–+, March 1997.
- [51] Lavrent'eva L.G., Vilisova M.D., Preobrazhenskii V.V., and Chaldyshev V.V. Low-temperature molecular-beam epitaxy of GaAs: effect of excess arsenic on the structure and properties of the GaAs layers. *Russian Physics Journal*, 45(8):735–752, 2002.



- [52] J. G. Simmons and G. W. Taylor. Nonequilibrium steady-state statistics and associated effects for insulators and semiconductors containing an arbitrary distribution of traps. *Phys. Rev. B*, 4(2):502–511, Jul 1971.
- [53] J. P. Ibbetson and U. K. Mishra. Space-charge-limited currents in nonstoichiometric GaAs. *Appl. Phys. Lett.*, 68:3781–3874, 1996.
- [54] S. E. Ralph and D. Grischkowsky. Trap-enhanced electric fields in semi-insulators: The role of electrical and optical carrier injection. *Applied Physics Letters*, 59:1972–1974, October 1991.
- [55] K.-F. G. Pfeiffer, S. Tautz, P. Kiesel, C. Steen, S. Malzer, and G. H. Döhler. Investigation of deep electronic centers in low-temperature grown GaAs using extremely thin layers. *Applied Physics Letters*, 77:2349, October 2000.
- [56] P. N. Brunkov, V. V. Chaldyshev, A. V. Chernigovskii, A. A. Suvorova, N. A. Bert, S. G. Konnikov, V. V. Preobrazhenskii, M. A. Putyato, and B. R. Semyagin. Accumulation of Majority Charge Carriers in GaAs Layers Containing Arsenic Nanoclusters. *Semiconductors*, 34:1068–1072, September 2000.
- [57] Matsunami K., Takeyama T., Usunami T., Kishimoto S., Maezawa K., Mizutani T., Tomizawa M., Schmid P. and Lipka K.M., and Kohn E. Potential profile measurement of GaAs MESFETs passivated with low-temperature grown GaAs layer by Kelvin probe force microscopy. *Solid-State Electronics*, 43(8):1547–1553, 1999.
- [58] E. R. Brown, K. A. McIntosh, F. W. Smith, K. B. Nichols, M. J. Manfra, C. L. Dennis, and J. P. Mattia. Milliwatt output levels and superquadratic bias dependence in a low-temperature-grown GaAs photomixer. *Applied Physics Letters*, 64:3311–3313, June 1994.
- [59] N. Zamdmer, Qing Hu, K. A. McIntosh, and S. Verghese. *Appl. Phys. Lett.*, 75:2313, 1999.
- [60] H. Yamamoto, Z-Q. Fang, and D. C. Look. Nonalloyed ohmic contacts on low-temperature molecular beam epitaxial GaAs: influence of deep donor band. *Appl. Phys. Lett.*, 57:1537–1539, 1990.
- [61] J. M. Shannon. *Solid-State Electron*, 19, 1976.
- [62] Gregor Segschneider, Frank Jacob, Torsten Loeffler, Hartmut G. Roskos, Soenke Tautz, Peter Kiesel, and Gottfried Doehler. Free-carrier dynamics in low-temperature-grown GaAs at high excitation densities investigated by time-domain terahertz spectroscopy. *Phys. Rev. B*, 65:125205, 2002.
- [63] G. M. Rebeiz. Millimeter-wave and terahertz integrated circuit antennas. *Proceedings of the IEEE*, 80(11), 1992.

- [64] H. G. Brooker. Slot aerials and their relation to complementary wire aerials. *J. Inst. Elect. Engrs.*, 73(pt III A):620–626, 1946.
- [65] I. Cámara Mayorga, M. Mikulics, A. Schmitz, P. Van der Wal, R. Guesten, M. Marso, P. Kordos, and H. Lüth. An optimization of terahertz local oscillators based on LT-GaAs technology. *Proc. SPIE*, 5498:537, 2004.
- [66] A. Schmitz. Erzeugung von THz Strahlung. Praxissemester WS2003/2004. *RheinAhrCampus Fachhochschule*, ED-15, 2004.
- [67] A. J. Lochtefeld, M. R. Melloch, J. C. P. Chang, and E. S. Harmon. The role of point defects and arsenic precipitates in carrier trapping and recombination in low-temperature grown GaAs. *Appl. Phys. Lett.*, 69:1465, 1996.
- [68] G. Segshneider, T. Löffler F. Jacob, H. G. Roskos, S. Tautz, P. Kiesel, and G. Dohler. Free-carrier dynamics in low-temperature-grown GaAs at high excitation densities investigated by time-domain terahertz spectroscopy. *Phys. Rev. B*, 65:125205, 2002.
- [69] I. Cámara Mayorga, E. A. Michael, A. Schmitz, P. van der Wal, R. Güsten, K. Maier, and A. Dewald. Terahertz photomixing in high energy oxygen- and nitrogen-ion-implanted GaAs. *Applied Physics Letters*, 91:1107–+, July 2007.
- [70] A. Claverie, Fereydoon Namavar, and Z. Liliental-Weber. *Appl. Phys. Lett.*, 62:1271–1273, 1993.
- [71] A. Krotkus, S. Marcinkevicius, J. Jasinski, M. Kaminska, H. H. Tan, and C. Jagadish. *Appl. Phys. Lett.*, 66:3304–3307, 1995.
- [72] T.-A. Liu, M. Tani, and C.-L. Pan. *J. Appl. Phys.*, 93:2996, 2003.
- [73] M. Mikulics, M. Marso, I. C. Mayorga, R. Güsten, S. Stanček, P. Kováč, S. Wu, X. Li, M. Khafizov, R. Sobolewski, E. A. Michael, R. Schieder, M. Wolter, D. Buca, A. Förster, P. Kordoš, and H. Lüth. Photomixers fabricated on nitrogen-ion-implanted GaAs. *Applied Physics Letters*, 87:1106–+, July 2005.
- [74] A. W. Sarto and B. J. Van Zeghbroeck. *IEEE J. Quantum Electron.*, 33(12):2188, 1997.
- [75] C. Jagadish, H. H. Tan, J. Jasinski, M. Kaminska, M. Palczewska, A. Krotkus, and S. Marcinkevicius. *Appl. Phys. Lett.*, 67:1724–1726, 1995.
- [76] G.-R. Lin, F. Ganikhanov, W.-C. Chen, C.-S. Chang, and C.-L. Pan. *Appl. Phys. Lett.*, 69:996–998, 1996.

- [77] A. Reklaitis, A. Krotkus, and G. Grigaliuneunaite. *Semicond. Sci. Techn.*, 14:945–947, 1999.
- [78] I. Cámara Mayorga, P. Muñoz Pradas, E. A. Michael, M. Mikulics, A. Schmitz, P. van der Wal, C. Kaseman, R. Güsten, K. Jacobs, M. Marso, H. Lüth, and P. Kordoš. Terahertz photonic mixers as local oscillators for hot electron bolometer and superconductor-insulator-superconductor astronomical receivers. *Journal of Applied Physics*, 100:3116–+, August 2006.
- [79] E. R. Brown, K. A. McIntosh, F. W. Smith, M. J. Manfra, and C. L. Denis. Measurements of optical-heterodyne conversion in low-temperature-grown gaas. *Appl. Phys. Lett.*, 62:1206, 1992.
- [80] K.A. McIntosh S.M. Duffy S.D. Calawa C.Y.E. Tong R. Kimberk S. Verghese, E.K. Duerr and R. Blundell. A photomixer local oscillator for a 630-GHz heterodyne receiver. *IEEE Microwave and Guided Wave Lett.*, 9:245, 1999.
- [81] K. Hagedorn R. Güsten F. Schäfer H. Stür F. Siebe P. van der Wal V. Krozer M. Feiginov D. Jäger A. Stöhr, R. Heinzelmann. Integrated 460 GHz photonic transmitter module. *Electronics Letters*, 37(22):1347–1348, 2001.
- [82] A. Stöhr, A. Malcoci, A. Sauerwald, I. Cámara Mayorga, R. Güsten, and D. S. Jäger. Ultra-Wide-Band Traveling-Wave Photodetectors for Photonic Local Oscillators. *Journal of Lightwave Technology*, 21:3062–+, December 2003.
- [83] S. Calawa W. F. Dinatale E. K. Duerr S. Verghese, K. A. McIntosh and K. A. Molvar. Generation and detection of coherent terahertz waves using two photomixers. *Appl. Phys. Lett.*, 73:3824, 1998.
- [84] For further information refer to P. F. Goldsmith, "Quasioptical Systems: Gaussian Beam Quasioptical Propagation and Applications", IEEE Press/Chapman and Hall Publishers Series on Microwave Tec, 1998, ch. 2.
- [85] Andreas Schmitz. Aufbau und Charakterisierung eines Zwei-Farben Diodenlasers. Master's thesis, Rhein-Ahr Campus, 2005.
- [86] Martin Wingender. *Aufbau eines Laser-Misch-Experiments zur Erzeugung von Differenzfrequenzen im Sub-Millimeter- und Terahertz-Bereich*. PhD thesis, Universität zu Köln, 2000.
- [87] R. Holzwarth, Th. Udem, T. W. Hänsch, J. C. Knight, W. J. Wadsworth, and P. St. J. Russell. Optical frequency synthesizer for precision spectroscopy. *Phys. Rev. Lett.*, 85(11):2264–2267, Sep 2000.

- [88] M. Kourogi, K. Nakagawa, and M. Ohtsu. Wide-span optical frequency comb generator for accurate optical frequency difference measurement. *IEEE Journal of Quantum Electronics*, 29:2693–2701, 1993.
- [89] Masahiko Tani, Osamu Morikawa, Shuji Matsuura, and Masanori Hangyo. *Semicond. Sci. Technol.*, 20:151–163, 2005.
- [90] S. Hoffmann A. Schmitz I. C. Mayorga A. Klehr G. Erbert C.-S. Friedrich, C. Brenner and M. R. Hofmann. New two color laser concepts for thz-generation. *IEEE J. Sel. Top. Quant.*, 14:270, 2008.
- [91] Hyunjoo Kim. *Dual-Mode Laser for a Photonic Local Oscillator in the Submillimeter Band and The Molecular Composition of an Oxygen-Rich Asymptotic Giant Branch Star*. PhD thesis, University of Bonn, 2007.
- [92] M. R. Stone, M. Naftaly, R. E. Miles, I. C. Mayorga, A. Malcoci, and M. Mikulics. Generation of continuous-wave terahertz radiation using a two-mode titanium sapphire laser containing an intracavity Fabry-Perot etalon. *Journal of Applied Physics*, 97:3108–+, May 2005.
- [93] M. Kourogi, B. Widiyatomo, Y. Takeuchi, and M. Ohtsu. Limit of optical-frequency comb generation due to material dispersion. *IEEE Journal of Quantum Electronics*, 31:2120–2126, 1995.
- [94] J. D. Zuegel and D. W. Jacobs-Perkins. Efficient, High-Frequency Bulk Phase Modulator. *Applied Optics*, 43:1946–1950, March 2004.
- [95] E. Bonek, M. Knecht, G. Magerl, K. Preis, and K. R. Richter. Coupling and tuning of trapped-mode microwave resonators. *Archiv Elektronik und Uebertragungstechnik*, 32:209–214, June 1978.
- [96] A. E. Siegman. *Lasers*. University Science Books, 1986.
- [97] R. P. Kovacich. PhD thesis, Department of Physics, University of Western Australia, Perth.
- [98] V. N. del Piano, Jr. and A. F. Quesada. Transmission characteristics of Fabry-Perot interferometers and a related electrooptic modulator. *Applied Optics*, 4:1386–+, November 1965.
- [99] J. L. Hall, L.-S. Ma, and G. Kramer. Principles of optical phase-locking - Application to internal mirror He-Ne lasers phase-locked via fast control of the discharge current. *IEEE Journal of Quantum Electronics*, 23:427–437, April 1987.

# Acknowledgements

This thesis is the result of the experience accumulated during many years in the Submillimeter Technology Group of the Max Planck Institute for Radio Astronomy (MPIfR).

My greatest appreciations and thanks go to Peter van der Wal and Rolf Güsten. Peter is not only a great scientist but also a formidable person. He supported me during all these years giving me advise and sharing with me his wide practical knowledge and experience on lasers. Thanks to our open-minded dialogue I felt always free to discuss any idea with him. I am deeply indebted to Rolf for inviting me to join the MPIfR Submillimeter Technology Group. Without his support, energy and assertiveness our terahertz photonic local oscillator would have not become a reality.

I received incalculable help from Andreas Schmitz in all the laboratory experiments. Furthermore his mastery in mechanical design helped a lot to find solutions for practical difficulties.

I owe a heavy debt of gratitude and sincere thanks to Prof. Dr. Karl Maier for his willingness to supervise my PhD thesis and to Prof. Dr. Karl Menten for his support and interest in my work.

I would like to thank Christoph Kasemann, Thomas Klein, Frank Schäfer, Sener Türk, Gundula Lundershausen, Alan Roy and all colleagues from the MPIfR who supported me in my work. From the University of Cologne I give special thanks to Ernest Michael, Alfred Dewald and Karl Jacobs. Last but not least I thank Martin Mikulics and his colleagues from the Institut für Schichten und Grenzflächen (Forschungszentrum Jülich) for the preparation of LTGaAs photomixers.

From the "social" point of view I made lots of good friends in Bonn with whom I shared very pleasant moments. In this respect I give my thanks especially to Michael Eichholtz and all of the "Sebastianstrasse Nummer Zwei" troop: Justine, Nico, Nick and Tatjana. Our long breakfasts and cocktails in "Extra-dry" will remain forever in my memory.

A Jabata, Lord y a Calva les debo todo; ya que me han dado ayuda, cariño y comprensión a lo largo de toda mi vida. A Pirichitipiritún le agradezco su entusiasmo por la física y las ideas que me da continuamente.

El núcleo de esta tesis fue escrito en una dacha en Zavidovo, Rusia, acompañado de mis abuelos rusos Dyadya Kostya y Babushka Mila. A ellos les

estaré siempre agradecido por su hospitalidad y buen humor. Las deliciosas tartas y blinís que me prepararon durante mi estancia fueron un alimento indispensable para la mente en la preparación de este trabajo.

Hay una persona muy especial que, a pesar de no aparecer en ninguna publicación de este trabajo, es la que más ha contribuido al éxito del mismo; se trata de Evgenia Muraviova, mi esposa. Es a ella a quien deseo darle mi más emotivo y profundo agradecimiento. Gracias a su paciencia y apoyo incondicional a lo largo de estos años, las páginas de esta tesis doctoral son una realidad.

# Publications and Conferences

1. Claus-Stefan Friedrich, Carsten Brenner, Stefan Hoffmann, Andreas Schmitz, **Iván Cámara Mayorga**, Andreas Klehr, Götz Erbert, and Martin R. Hofmann. New Two-Color Laser Concepts for THz Generation. IEEE Journal Of Selected Topics In Quantum Electronics, vol. 14, no. 2, March/ April (2008).
2. **Cámara Mayorga I.**, Ernest Michael , Andreas Schmitz , Peter van der Wal , Rolf Guesten, Karl Maier, Alfred Dewald et al. Terahertz Photomixing in high energy oxygen- and nitrogen-ion-implanted GaAs, Applied Physics Letters, 91 (2007)
3. E. A. Michael, **Cámara Mayorga Iván**, Rolf Güsten, Alfred Dewald, Rudolf Schieder, Terahertz continuous-wave large-area traveling-wave photomixers on high-energy low-dose ion-implanted GaAs, Applied Physics Letters, 90 (2007).
4. **Cámara Mayorga I.**, P. Muñoz Pradas, M. Mikulics, A. Schmitz, C. Kasemann, P. van der Wal, K. Jakobs and R. Güsten, Terahertz photonic mixers as local oscillators for hot electron bolometer and superconductor-insulator-superconductor astronomical receivers, J. Appl. Phys, 100, Issue 4, pp. 043116-043116-4 (2006).
5. **Cámara Mayorga I.**, P. Muñoz Pradas, M. Mikulics, A. Schmitz, C. Kasemann, P. van der Wal, K. Jakobs and R. Güsten, Superconductor- Insulator- Superconductor (SIS) and Hot Electron Bolometer (HEB) pumping with LT-GaAs based photonic local oscillators. International Symposium on Space Terahertz Technology (Gothenburg 2005)
6. Stone M.R., Naftaly M., Miles R.E., **Cámara Mayorga I.** , Malcoci A., Mikulics M., 2005, Generation of continuous-wave terahertz radiation using a two-mode titanium sapphire laser containing an intracavity Fabry-Perot etalon, J. Appl. Phys. 97, 103108 (2005)
7. M. Mikulics, M. Marso, **I. Cámara Mayorga**, R. Güsten, S. Stancek, P. Kovac, S. Wu, X. Li, M. Khafizov, R. Sobolewski, E.A. Michael, R. Schieder, M. Wolter, D. Buca, A. Förster, P. Kordoš, H. Lüth, Photomixers fabricated on nitrogen-ion-implanted GaAs, Applied Physics Letters, 87 (2005), 041106

8. M. Naftaly, M.R. Stone, A. Malcoci, R.E. Miles and **I. Cámara Mayorga**. Generation of CW Terahertz radiation using two-colour laser with Fabry-Perot etalon. *Electronic Letters*, Vol. 41 no. 3, pp 128. (2005)
9. M. Marso, M. Mikulics, R. Adam, S. Wu, X. Zheng, **I. Cámara Mayorga**, F. Siebe, A. Förster, R. Güsten, P. Kordoš, and R. Sobolewski, Ultrafast phenomena in freestanding LT-GaAs devices, *Acta Phys. Polonica A* 107,109 (2005)
10. **I. Cámara Mayorga**, M. Mikulics, A.Schmitz, P.van der Wal, R.Güsten, M.Marso, P. Kordoš, H. Lüth. An Optimization of Terahertz Local Oscillators based on LT-GaAs Technology. *Proc. SPIE*, Volume: 5498, pp. 537 (SPIE, Glasgow 2004)
11. Mikulics, M., **Cámara Mayorga, I.**, Marso, M., v.d.Hart, A., Fox, A., Förster, A., Güsten, R., Lüth, H., and Kordoš, P.: Generation of THz radiation by photomixing in low-temperature-grown MBE GaAs. In: *ASDAM 2004*, pp. 231-234, Piscataway: IEEE 2004
12. Mikulics, M., Wolter, M.J., Marso, M., **Cámara Mayorga, I.**, Stancek, S., Wu, S., Buca, D., Sobolewski, R., Kovác, P., Guesten, R., Lüth, H., and Kordoš, P.: Nitrogen implanted GaAs for ultrafast photodetectors and photomixers. In: *ASDAM 2004*, pp. 53-56, Piscataway: IEEE 2004
13. Adam, R., Mikulics, M., Wu,S., Zheng,X., Marso, M., **Cámara Mayorga, I.**, Siebe, F., Güsten,R., Förster,A., Kordoš,P., and Sobolewski,R.: Fabrication and performance of hybrid photoconductive devices based on freestanding LT-GaAs, *Proc. SPIE Vol.5352*, pp. 321, 2004
14. M. Marso, M. Mikulics, R. Adama, S. Wu, X. Zheng, **I. Camara Mayorga**, F. Siebe, A. Forster, R. Gusten, P. Kordoš and R. Sobolewski, Ultrafast Phenomena in Freestanding LT-GaAs Devices. *Proceedings of the 12th International Symposium UFPS, Vilnius, Lithuania 2004*
15. A.Stöhr, A.Malcoci, A. Sauerwald, **I. Cámara Mayorga**, R.Güsten, D.Jäger, Ultra-Wide-Band Traveling-Wave Photodetectors Photonic Local Oscillators. *Journal Of Lightwave Technology*, Vol. 21, No. 12, December 2003
16. Güsten, R.; **Camara, I.**; Hartogh, P.; Hübers, H.-W.; Graf, U.; Jacobs, K.; Kasemann, C.; Röser, H.-P.; Schieder, R.; Schnieder, G.; Siebertz, O.; Stutzki, J.; Villanueva, G.; Wagner, A.; van derWal, P.; Wunsch, A.; GREAT: The German Receiver for Astronomy at Terahertz Frequencies. *Proc. SPIE*, 56-61 (2003)



17. **I. Cámara Mayorga**, M. Mikulics, M. Marso, P. Kordoš, A. Malcoci, A. Stoer, D. Jaeger and R.Güsten: THz Photonic Local Oscillators. Workshop: New Perspectives for Post-Herschel far infrared astronomy from space. 1-4 September 2003 Madrid, Spain

Reviewer of several papers in:

- Journal of Applied Physics
- Applied Physics Letters
- IEEE/OSA Journal of Lightwave Technology

## Terahertz photonic mixers as local oscillators for hot electron bolometer and superconductor-insulator-superconductor astronomical receivers

I. Cámara Mayorga<sup>a)</sup>*Max-Planck-Institute for Radioastronomy, Auf dem Hügel 69, 53121 Bonn, Germany*

P. Muñoz Pradas and E. A. Michael

*1. Physics Institute, University of Cologne, Zùlpicher Strasse 77, 50937 Cologne, Germany*

M. Mikulics

*Institute of Thin Films and Interfaces (ISG-1), Research Center Jùlich, 52425 Jùlich, Germany*

A. Schmitz, P. van der Wal, C. Kaseman, and R. Gùsten

*Max-Planck-Institute for Radioastronomy, Auf dem Hügel 69, 53121 Bonn, Germany*

K. Jacobs

*1. Physics Institute, University of Cologne, Zùlpicher Strasse 77, 50937 Cologne, Germany*

M. Marso, H. Lùth, and P. Kordoš

*Institute of Thin Films and Interfaces (ISG-1), Research Center Jùlich, 52425 Jùlich, Germany*

(Received 4 October 2005; accepted 19 July 2006; published online 30 August 2006)

A pump experiment of two astronomical heterodyne receivers, a superconductor-insulator-superconductor (SIS) receiver at 450 GHz and a hot-electron-bolometer (HEB) receiver at 750 GHz, is reported. A low-temperature-grown GaAs metal-semiconductor-metal photonic local oscillator (LO) was illuminated by two near infrared semiconductor lasers, generating a beat frequency in the submillimeter range. *I-V* junction characteristics for different LO pump power levels demonstrate that the power delivered by the photomixer is sufficient to pump a SIS and a HEB mixer. SIS receiver noise temperatures were compared using a conventional solid-state LO and a photonic LO. In both cases, the best receiver noise temperature was identical ( $T_{\text{sys}}=170$  K).

© 2006 American Institute of Physics. [DOI: 10.1063/1.2336486]

### I. INTRODUCTION

Photomixing has been used for several years as a technique for signal generation in the millimeter and submillimeter ranges.<sup>1</sup> The huge bandwidth offered by a single photomixing device (from dc to several terahertz) has tremendous potential for various applications such as radio astronomy, terahertz imaging, high-resolution spectroscopy, medicine, security, and defense. The progress made in the fabrication of low-temperature-grown GaAs (LT-GaAs) has lead to carrier trapping times below 1 ps at moderate bias voltages, which is essential for fabrication of photomixers in the terahertz range.

In this paper we report on photomixing as a local oscillator (LO) source for heterodyne detection in radio astronomy. The development is aimed at the integration of a photonic LO in the German Receiver for Astronomy at Terahertz Frequencies (GREAT), which will be a first-generation dual-channel heterodyne instrument for high-resolution spectroscopy aboard Stratospheric Observatory For Infrared Astronomy (SOFIA), and in the high-frequency heterodyne receivers at the Atacama Pathfinder Experiment (APEX), currently in final commissioning.

### II. PHOTONIC GENERATION OF TERAHERTZ RADIATION

The scheme for optical heterodyning (Fig. 1) consisted of two slightly detuned near infrared (NIR)  $\sim 780$  nm continuous-wave (cw) monomode lasers in Littman configuration (New Focus, model Velocity 6312), where at least one laser was tunable to make frequency selection possible. The output power of the lasers,  $\sim 6$  mW, was insufficient for satisfactory rf power generation in the photomixer. With a set of mirrors and beam splitters, the laser beams were made col-

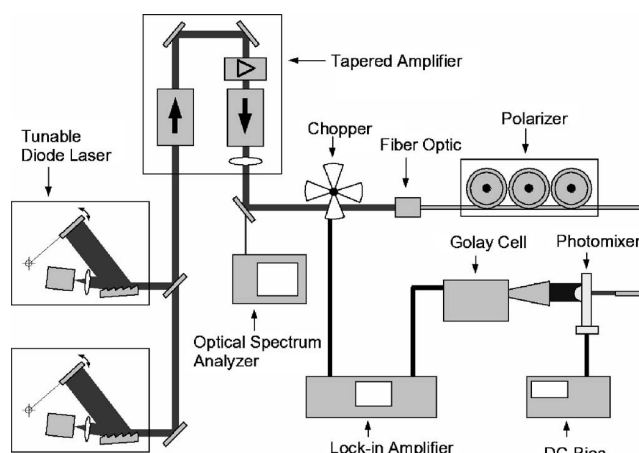


FIG. 1. Schematic diagram of the measurement setup.

<sup>a)</sup>Author to whom correspondence should be addressed; electronic mail: imayorga@mpifr-bonn.mpg.de

linear and drove a tapered laser amplifier (Toptica TA100). This configuration provided up to 0.5 W of combined power.

The beam was then coupled into a single-mode optical fiber (95%) and to an optical spectrum analyzer (with 5%) to monitor frequency difference and to guarantee equal power distribution between the two colors. To avoid optical feedback to the lasers and amplifier, we included in the setup optical isolators and fiber optics with angled polished connectors (APC), providing  $>60$  dB reflection losses. A fiber polarizer converted the laser polarization of the optical fiber input to a polarization orthogonal to the finger direction of the photomixer. This procedure is mandatory to minimize reflection from the photomixer, since the finger structure has dimensions comparable to the laser wavelength.

To achieve optimal photomixer illumination, the optical fiber was positioned with a piezoelectric actuator. This device allowed a fine ( $\sim 100$  nm) position control in three axes. The air gap between the optical fiber and photomixer substrate acts as a Fabry-Pérot etalon, so we used an optical adhesive<sup>2,3</sup> with a similar refraction index as the optical fiber core to pigtail the fiber optic to the photomixer. This process also inhibited the negative effects of mechanical vibrations, which potentially could lead to mispositioning of the fiber optic over time thus limiting the reproducibility of our experiments.

Once the two lasers interfere on the LT-GaAs photoactive area, electron-hole pairs are generated. The bias voltage applied to the electrodes builds an electric field that separates the photocarriers, creating a photocurrent proportional to the optical intensity. The ultrashort electron lifetimes of LT-GaAs allow the photocurrent to “follow” the envelope of the optical instantaneous power. Details of the underlying physical phenomena can be found elsewhere.<sup>4-6</sup>

The photoactive area was patterned at the feed point of a resonant or broadband antenna, so that the beat signal was radiated to free space. The high dielectric constant of the GaAs photomixer substrate ( $\epsilon_r=12.8$ ) prevented the signal from being radiated backwards to the fiber optic. The hyper-hemispherical form of the substrate suppressed surface modes and provided acceptable beam directivity.<sup>7,8</sup>

### III. MIXING EXPERIMENT WITH A SIS RECEIVER AT 450 GHz

The power performance and noise temperature of our photomixers were verified first with a superconductor-insulator-superconductor (SIS) mixer. Similar pump<sup>9-11</sup> and noise temperature<sup>11</sup> experiments have already been reported.

It is well known that photomixers have a high internal resistance,<sup>12</sup> and thus impedance matching is difficult. For this reason, high radiation resistance antennas are needed. Full-wave dipole antennas show a higher resistance ( $\sim 210 \Omega$  on a GaAs substrate) than broadband logarithmic spiral antennas ( $\sim 73 \Omega$  on a GaAs substrate). The polarization of a dipole is linear, having the same orientation as the dipole itself, whereas the polarization of a spiral is circular (supposing a photomixer area with dimensions much smaller than the wavelength of the terahertz signal). Furthermore, the Gaussicity of a dipole is better than that of a spiral antenna.

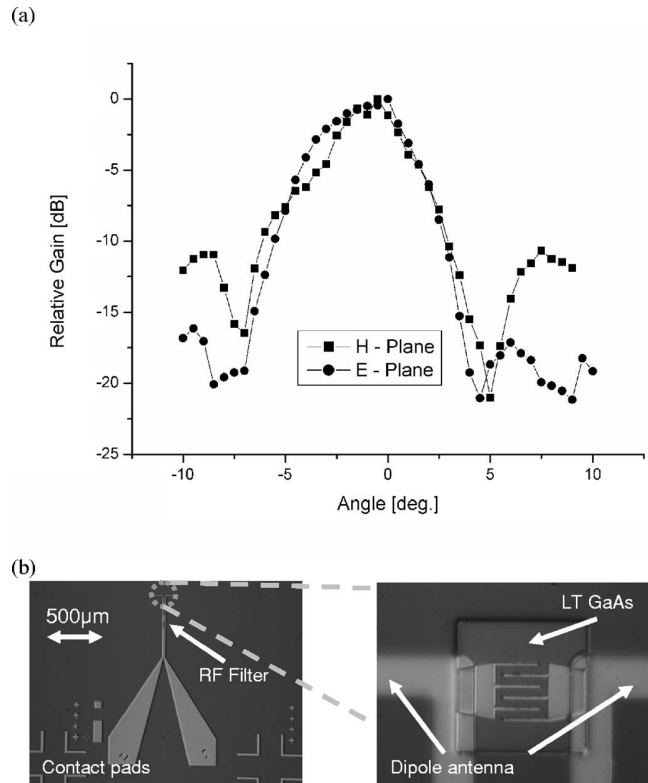


FIG. 2. (a) *E*-plane and *H*-plane power patterns measured for a full-wave dipole in resonance at 450 GHz. The high-resistivity Si substrate has a hyper-hemispherical form to reduce the divergence of the beam. (b) Microphotograph of the dipole antenna and finger structure of the photoactive area.

Our SIS mixer was sensitive only to linearly polarized signals, further favoring the use of a dipole antenna.

In our first experiment, a SIS mixer was pumped with a dipole antenna photomixer. Amplitude measurements across the *E* and *H* planes showed good Gaussicity and low side-lobes (Fig. 2).

The SIS junction *I-V* characteristic of an astronomical heterodyne receiver at 450 GHz is shown in Fig. 3 for two different LO power pump levels. With a photocurrent of 0.6 mA and a NIR optical power of 70 mW, the rf power generated was  $0.8 \mu\text{W}$ , which is a factor of three below the device burnout at room temperature, so that an acceptable safety margin is available to operate the photonic LO.

To investigate whether the photonic LO adds significant internal noise to the mixer, we compared receiver noise temperatures derived from hot and cold measurements using a conventional solid-state LO and the photonic LO. A Martin-Puplett (MP) diplexer was used to inject the LO signal into the signal path. The divergent beam from the MP diplexer output was transformed to a convergent beam with a plane-convex Teflon lens.

The double sideband (DSB) noise temperatures of the astronomical receiver pumped by the photomixer and by the solid-state LO (both measured at an intermediate frequency band of 2–4 GHz) were identical ( $T_{\text{receiver}}=170$  K). In contrast to cascading multipliers, the noise contribution of a photonic LO is not expected to increase with frequency be-

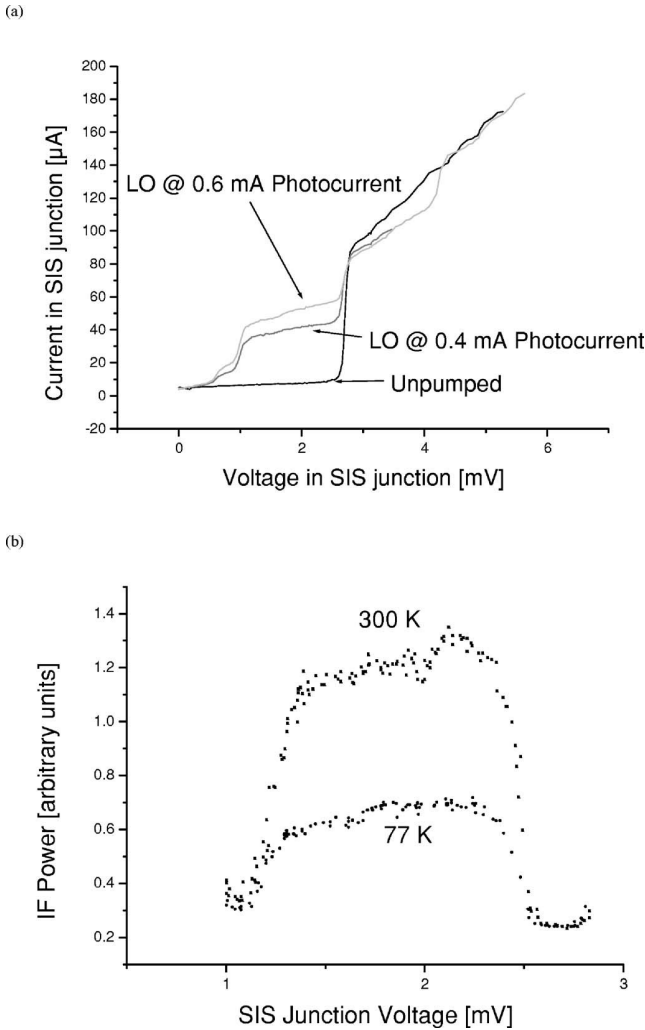


FIG. 3. (a) The  $I/V$  curve of the SIS mixer in the absence of LO signal and pumped by a photonic LO signal at 450 GHz for two different LO power levels. (b) Corresponding IF power performance for hot and cold blackbodies.

cause the terahertz signal is directly generated by optical mixing of two laser signals, a process which is frequency independent.

#### IV. MIXING EXPERIMENT WITH A HEB AT 750 GHz

The hot electron bolometer (HEB) consisted of a NbTiN bridge on a  $\text{Si}_3\text{N}_4$  membrane with dimensions approximately  $4 \times 0.4 \times 0.004 \mu\text{m}^3$ . The design frequency was 750 GHz. At this frequency no resonant antenna photomixer device was available, so a photomixer with an integrated logarithmic spiral antenna was used.

The membrane waveguide HEB mixer used for the experiment was sensitive to vertical polarization. The beam waist position was located at the Dewar window. To optimize the design of the quasioptical coupling, the beam parameters of the photomixer beam were determined previously. For this purpose, a power detector (Golay Cell) was installed on a computer-controlled motorized translation stage. The terahertz beam was scanned bidimensionally, varying the position of the Golay Cell over a matrix of  $30 \times 30$  pixels. This

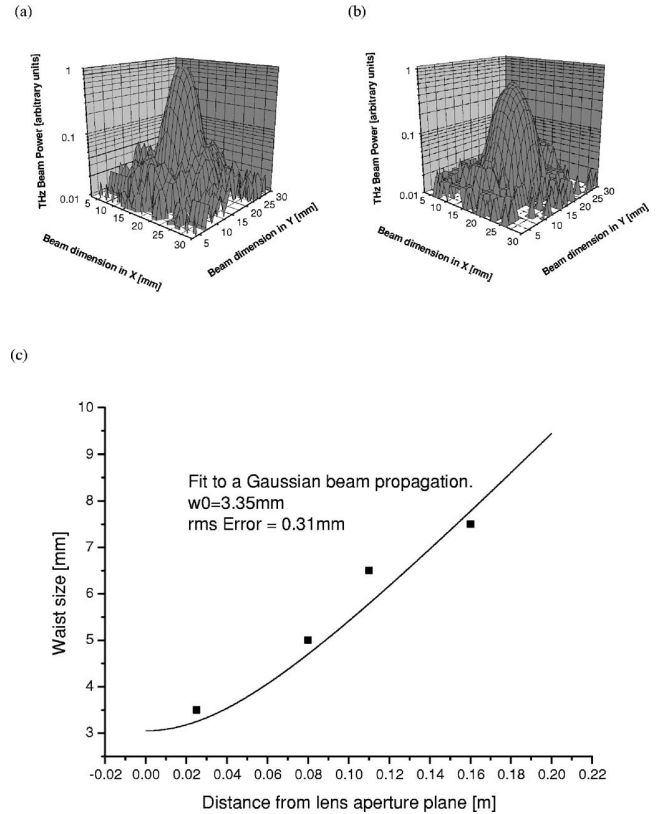


FIG. 4. [(a) and (b)] Beam characterization at 50 and 110 mm from the lens aperture plane. (c) The waist size of the propagating LO beam was measured at different distances from the photomixer lens aperture plane. The data points were fitted to a Gaussian-beam propagation curve. From the fit, the minimum waist (beam waist)  $w_0$  was extracted. The dimensions of the photomixer substrate lens were calculated to synthesize an ellipse. The position of the beam waist coincides with the lens-to-air interface.

process was repeated at different positions to obtain the beam diameter dependence on distance. By fitting the experimental beam diameters to a theoretical Gaussian-beam propagation, the beam waist  $w_0$  was determined to be 3.3 mm (see Fig. 4). The beam waist of the HEB mixer was similar to the photomixer beam waist, avoiding the need of a Gaussian-beam telescope for matching the HEB and photomixer beam waists.

The immediate problem associated with the use of a spiral antenna is the need of transforming its circular polarization to vertical to match the polarization of the HEB mixer. For this purpose, two MP diplexers were used in the quasioptical setup (Fig. 5). The first transformed the polarization from circular to linear. The second MP diplexer was used to inject the hot and cold loads for noise temperature measurements. An off-axis paraboloidal mirror with a focal length of 250 mm was positioned at the center of the quasioptical setup to image the photomixer beam waist into the HEB beam waist. The calculated object and image distances were 485 mm.

To assure that beam truncation in the MP diplexers did not play a major role, the ratio between the beam and aperture diameters at the output and input of the MP diplexers was computed and found to be in the worst case  $1/3$ , which represents<sup>13</sup> negligible spillover losses.

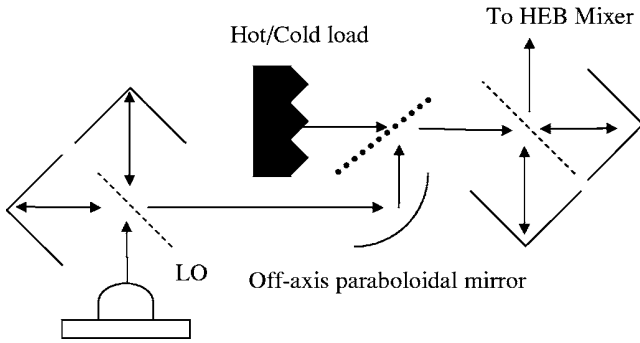


FIG. 5. Schematic of the quasioptical setup. A first MP diplexer transforms the circular polarization from the log-spiral antenna photomixer to vertical. The paraboloidal mirror makes the diverging LO beam convergent. The second MP diplexer injects the hot and cold load signals.

Figure 6 represents the  $I$ - $V$  characteristic of the HEB mixer with and without photonic LO power. The noise temperature measurements were not reproducible due to the standing waves and microphony. Usually HEBs are much more sensitive than SIS mixers to these effects.

The photomixer was illuminated by 70 mW of NIR power and the photocurrent was 1.7 mA, generating 450 nW of rf power at 750 GHz, which is near the photomixer burn-out point at room temperature. At the output of the quasioptical system, the rf power was 375 nW, which implies 20% quasioptical and water absorption losses.

The absorbed rf power in the HEB was calculated using the isothermal method to be 300 nW, which is consistent with the measured power at the input of the HEB Dewar. The same HEB mixer was used in a different experiment pumped with a conventional (frequency-multiplied Gunn oscillator) local oscillator source and showed good heterodyne response ( $T_{\text{receiver}}$  as low as 500 K at 750 GHz). The direct detection

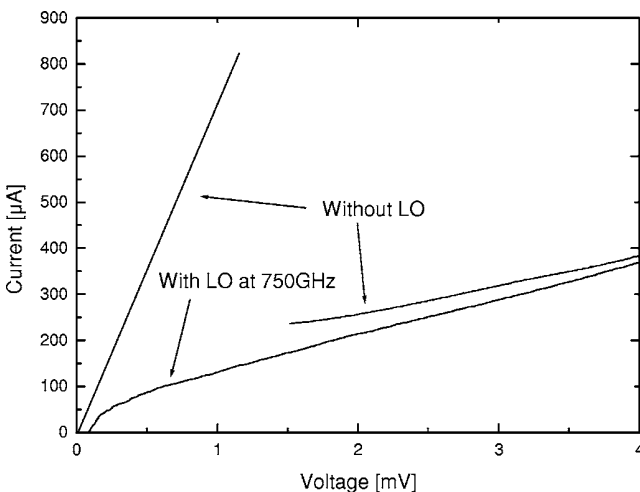


FIG. 6. The  $I$ / $V$  curve of the HEB without LO power and pumped by the photomixer at 750 GHz. The pumped curve has been averaged to eliminate the scatter which resulted from standing waves and microphony. Due to the hysteretic HEB  $I$ / $V$  characteristic in the unpumped case, the superconducting branch and the normal conducting branch of the  $I$ / $V$  curve are separated. The resistance in the superconducting branch (straight line at left) comes from a series resistance in the bias circuit. When irradiated by the local oscillator power, the HEB  $I$ / $V$  becomes nonhysteretic as shown in the lower curve. The difference in current at a given bias voltage between the two curves is proportional to the absorbed local oscillator power.

effects (e.g., by thermal broadband emission) in this relatively large ( $4 \times 0.4 \times 0.004 \mu\text{m}^3$ ) device embedded in a waveguide are negligibly small compared to the effect seen by the photomixer pumping. The blackbody radiation power of a 300 K source in a 200 GHz bandwidth (which is roughly the rf bandwidth of the mixer) would only be 0.8 nW. This has to be compared to the 300 nW seen as the absorbed rf power of the photomixer in the device.

There is room for rf power improvement by using a full-wave dipole antenna photomixer. In that case, the expected output power would be higher by a factor of 3, due to its higher radiation resistance. Also its better Gaussicity and linear polarization would simplify considerably the quasioptical setup.

## V. CONCLUSIONS AND FUTURE WORK

This is an experiment in which a photonic local oscillator has pumped a HEB and is the highest frequency (750 GHz) at which a photonic LO has pumped an astronomical receiver. Noise temperature measurements performed with a SIS receiver at 450 GHz showed a best system noise temperature of 170 K for both photonic LO and a solid-state LO pumping.

Next, we will push our experiments to even higher frequencies using SIS and HEB mixers operated at 1.0 and 1.4 THz, respectively. For this purpose, dipole antenna based photomixers will be processed with inductive canceling of the finger capacity. A further rf power increase is expected through cryogenic operation,<sup>14</sup> which will push up the photomixer breakdown conditions and allows photomixer illumination at higher laser power and bias voltages (rf power scales quadratically with laser power and bias voltage).

<sup>1</sup>E. R. Brown, K. A. McIntosh, F. W. Smith, M. J. Manfra, and C. L. Denis, *Appl. Phys. Lett.* **62**, 1207 (1992).

<sup>2</sup>Norland Optical Adhesive 61.

<sup>3</sup>S. Verghese, K. A. McIntosh, and E. R. Bown, *Appl. Phys. Lett.* **71**, 2743 (1997).

<sup>4</sup>E. R. Brown, F. W. Smith, and K. A. McIntosh, *J. Appl. Phys.* **73**, 1480 (1993).

<sup>5</sup>E. R. Brown, K. A. McIntosh, F. W. Smith, K. B. Nichols, M. J. Manfra, C. L. Dennis, and J. P. Mattia, *Appl. Phys. Lett.* **64**, 3311 (1994).

<sup>6</sup>N. Zamdmer, Q. Hu, K. A. McIntosh, and S. Verghese, *Appl. Phys. Lett.* **75**, 2313 (1999).

<sup>7</sup>D. B. Rutledge, D. P. Neikirk, and D. P. Kasilingam, *Infrared and Millimeter Waves*, edited K. J. Button (Academic, New York, 1983), Vol. 10, pp. 1–90.

<sup>8</sup>D. F. Filipovic, S. S. Gearhart, and G. M. Rebeiz, *IEEE Trans. Microwave Theory Tech.* **41**, 1738 (1991).

<sup>9</sup>S. Verghese, E. K. Duerr, K. A. McIntosh, S. M. Duffy, S. D. Calawa, C. Y. E. Tong, R. Kimberk, and R. Blundell, *IEEE Microw. Guid. Wave Lett.* **9**, 245 (1999).

<sup>10</sup>A. Stöhr *et al.*, *Electron. Lett.* **37**, 1347 (2001).

<sup>11</sup>A. Stöhr, A. Malcoci, A. Sauerwald, I. C. Mayorga, R. Güsten, and D. Jäger, *J. Lightwave Technol.* **21**, 3062 (2003).

<sup>12</sup>S. Verghese, K. A. McIntosh, S. Calawa, W. F. Dinatale, E. K. Duerr, and K. A. Molvar, *Appl. Phys. Lett.* **73**, 3824 (1998).

<sup>13</sup>The edge taper  $T_e(\text{dB}) = 8.686(r_a/w_a)^2 = 78$  dB, where  $r_a$  and  $w_a$  represent the aperture radius and beam radius at the aperture plane, respectively, describes the truncation of a fundamental mode Gaussian beam. For further information refer to P. F. Goldsmith, *Quasioptical Systems: Gaussian Beam Quasioptical Propagation and Applications* (IEEE, New York/Chapman and Hall, London, 1998), Chap. 2.

<sup>14</sup>I. Cámara Mayorga, M. Mikulics, A. Schmitz, P. Van der Wal, R. Güsten, M. Marso, P. Kordos, and H. Lüth, *Proc. SPIE* **5498**, 537 (2004).

# Terahertz photomixing in high energy oxygen- and nitrogen-ion-implanted GaAs

I. Cámara Mayorga,<sup>a)</sup> E. A. Michael, A. Schmitz, P. van der Wal, and R. Güsten  
 Max-Planck-Institute for Radio Astronomy, Auf dem Hügel 69, 53121 Bonn, Germany

K. Maier

Helmholtz-Institut für Strahlen- und Kernphysik, University of Bonn, Nußallee 14-16 53115 Bonn, Germany

A. Dewald

Institute for Nuclear Physics, University of Cologne, Zùlpicher Str. 77, 50937 Cologne, Germany

(Received 6 March 2007; accepted 9 June 2007; published online 19 July 2007)

In this letter, the authors elaborate a detailed study of ion-implanted GaAs terahertz photomixers. The authors implanted several GaAs samples with oxygen and nitrogen ions with energies between 2 and 3 MeV and doses ranging from  $2 \times 10^{11}$  to  $3 \times 10^{13}$  cm<sup>-2</sup>. The samples were processed by patterning metal-semiconductor-metal structures on the feed point of self-complementary log-periodic spiral broadband antennas. From dc measurements and analysis of frequency roll-off in the 100 GHz–1 THz range under variable bias conditions, the authors studied systematically the carrier trapping time, terahertz power, and photocurrent dependence on applied voltage and frequency for the different samples. © 2007 American Institute of Physics.

[DOI: 10.1063/1.2753738]

The generation of terahertz radiation by photomixing in low-temperature-grown gallium arsenide (LT GaAs) has been extensively investigated in the last decade. This material shows a high breakdown field ( $>300$  kV/cm), low dark current, acceptable carrier mobility ( $>200$  cm<sup>2</sup>/V s), and ultrashort carrier trapping time ( $\approx 200$  fs), features which are very attractive for photomixing applications. Owing to excess arsenic (1%–2%) during deposition, a nonstoichiometric, defect rich material is created. Ionized arsenic antisites As<sub>Ga</sub><sup>+</sup> and arsenic precipitates seem to be responsible for electron trapping in the subpicosecond range. The defect type and concentration have been reported to be highly dependent on the arsenic pressure and growth temperature of the sample during molecular beam epitaxy. The annealing temperature has been shown to be critical,<sup>1</sup> and small changes of this parameter cause large variations in dark resistance, mobility, and carrier lifetime.

In contrast to LT GaAs, the defects created in ion-implanted GaAs (Refs. 2–5) can be tailored by varying the implantation dose and energy. The precise control over these parameters helps to overcome the reproducibility limitations of LT GaAs. The collision of incoming ions with the lattice atoms forms vacancies, interstitials, antisites, and other defects, so that the material can exhibit similar carrier trapping mechanisms as LT GaAs. It is important that the ions do not change by themselves the properties of the material but rather that the material properties be defined by the bombardment through the ion beam. To achieve this, the implantation energies can be selected so that the peak of implantation profile is situated substantially deeper than the optical absorption length in GaAs, which is  $\sim 1$  μm. As seen in Fig. 1(a), the ion-simulated concentration peak is located deeper than the photoactive volume for the energies and species used. The defect concentration shows an almost linear in-

crease in the micron—see inset of Fig. 1(b)—from which one should expect similar behavior for the samples implanted with nitrogen at 2 MeV and oxygen at 3 MeV.

We implanted a set of semi-insulating (100) GaAs wafers with N<sup>3+</sup> and O<sup>4+</sup> with doses varying from  $3 \times 10^{11}$  to  $3 \times 10^{13}$  cm<sup>-2</sup> at 2 and 3 MeV ion energies.

No sample annealing was performed after implantation, so that the primary trapping mechanism is expected to be the point defect As<sub>Ga</sub><sup>+</sup>, in contrast to annealed LT GaAs where both As<sub>Ga</sub><sup>+</sup> and As precipitates are present. After the ion implantation, photomixer structures were processed on the different wafers using standard e-beam lithography. The metalization consisted of a 10/200 nm thick Ti/Au layer and the metal-semiconductor-metal (MSM) photomixing area with dimensions of  $\sim 9 \times 9$  μm<sup>2</sup> was composed of eight fingers with 200 nm width and 1 μm gap. The patterned antennae were self-complementary log-periodic spirals with three turns to exhibit a nearly constant impedance in the range of study (100 GHz–1 THz). Each individual photomixer was cleaved and mounted on a high resistivity silicon hyperhemi-

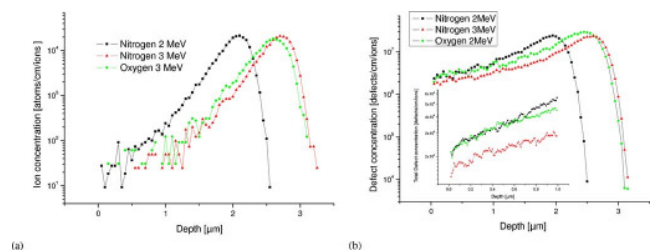


FIG. 1. (a) Concentration of ions vs depth. If multiplied by the dose in ions/cm<sup>2</sup>, this yields the ion concentration in ions/cm<sup>3</sup>. In all cases the peak is situated deeper than the optical absorption length. (b) Concentration of defects vs depth in the same units as (a). The peak coincides with that of the ion concentration. Note that defect concentration is around three orders of magnitude larger than the ion concentration in the first micron. The ion and defect concentrations were computed by stopping and range of ions in matter, where a Monte-Carlo simulation of  $10^5$  ions was performed.

<sup>a)</sup> Author to whom correspondence should be addressed; electronic mail: imayorga@mpifr-bonn.mpg.de

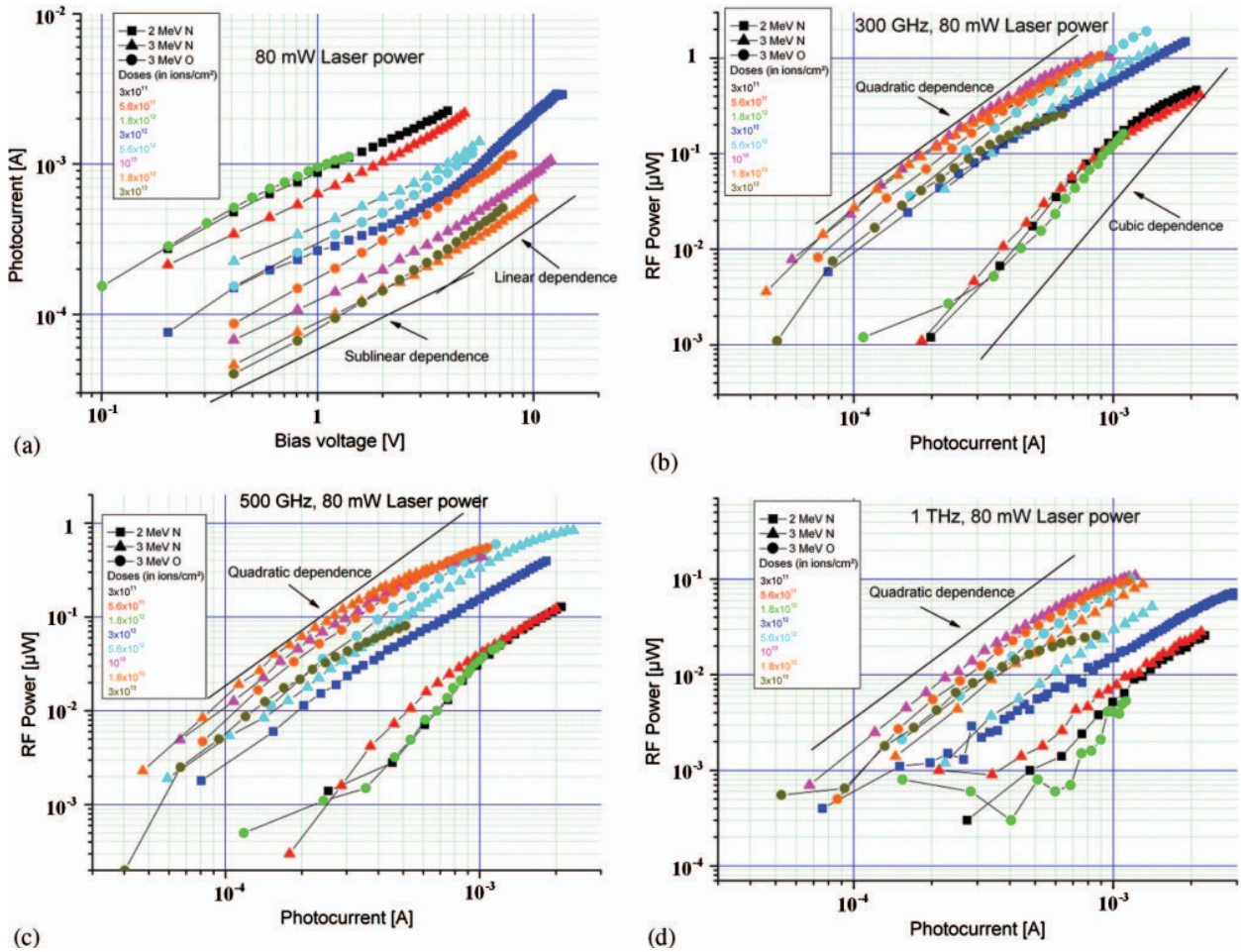


FIG. 2. (Color) (a)  $I$ - $V$  curves at different implantation energies and doses. The photocurrent has been calculated from the measured current under illumination by subtracting the dark current. This operation was necessary only for samples with doses above  $10^{13}$  ions/cm<sup>2</sup> since, for lower doses, the dark current was negligible (under  $10 \mu\text{A}$  for all bias voltage conditions). In (b)–(d), the terahertz power as a function of the photocurrent is represented. Note: the noise floor of our terahertz power detector was  $\sim 0.4$  nW.

spherical lens whose dimensions were calculated to collimate the terahertz radiation from the planar antenna. We bonded the outer spiral antenna arms to bias the photomixer structure.

The standard optical heterodyne theory states that the rf power  $P_\omega$  generated in a photomixer with bias voltage  $V_B$  equals<sup>6</sup>

$$P_\omega = \frac{(1/2)(V_B G_0(\tau, \nu, I_{\text{opt}}))^2 R_L}{(1 + (\omega\tau)^2)(1 + (\omega R_L C)^2)}, \quad (1)$$

where  $G_0$  is the time averaged photoconductance of the photomixer, which is a linear function of effective carrier lifetime, drift velocity, and optical intensity,  $R_L$  is the antenna input resistance ( $\sim 73 \Omega$  on a GaAs substrate for our spiral antenna) and  $C$ ,  $\tau$ , and  $\omega$  are the capacity of the finger structure, carrier lifetime, and beat angular frequency, respectively. This expression, which is valid only in the small-signal limit, assumes that both laser sources deliver the same power and have the same polarization. The two bracketed terms in the denominator describe two cutoff frequencies resulting from the carrier lifetime and a  $RC$  constant. For frequencies above 100 GHz, the rf power is mainly due to photoelectrons due to their smaller carrier lifetime and larger drift velocity.

In our terahertz measurement setup which is described elsewhere,<sup>12</sup> we performed three different measurements to study the implanted materials: (a) dc curves relating photocurrent to applied voltage for 80 mW laser power, (b) terahertz power curves at 300 GHz, 500 GHz, and 1 THz versus bias voltage for the same laser power, and (c) terahertz power versus frequency curves for constant bias voltage and dc photocurrent, thereby varying the laser power up to 80 mW. From the last set of curves, the effective photocarrier lifetime was estimated by fitting Eq. (1) to the measurement data.

Figure 2(a) represents the photocurrent as a function of bias voltage for photomixers on different implanted materials where the laser power was set to 80 mW. The  $I$ - $V$  characteristic begins with a sublinear dependence which becomes linear and superlinear at higher voltages (this is especially evident in the sample with a dose of  $3 \times 10^{12}$  cm<sup>-2</sup>). Drift velocity saturation explains<sup>7</sup> the sublinear range whereas at higher voltages, the well known<sup>8</sup> increase of carrier lifetime with voltage would increase the photoconductance and, consequently, the photocurrent. Other effects such as impact ionization may play a role as well. In contrast to  $P$ - $I$ - $N$  photodiodes, no plateau was found in the  $I$ - $V$  curve since the electric field was not uniform, so that the regions next to the electrodes showed velocity saturation first whereas the re-

gions located deeper into the substrate and in the middle of the electrodes needed higher voltages for velocity saturation to occur. As a result, the saturation mechanism is smeared out in the  $I$ - $V$  characteristic. There was an evident reduction of dc photocurrent at higher implantation doses since the presence of defects reduce the carrier lifetime and, consequently, the steady-state carrier concentration in accordance with  $J_{dc}(E) \propto \tau_p(E)v_{p, drift}(\mu_p, E) + \tau_n(E)v_{n, drift}(\mu_n, E)$ , where  $\tau_{n,p}$ ,  $\mu_{n,p}$ , and  $v_{n,p, drift}$  are the carrier lifetime, mobility, and drift velocity for holes and electrons. At implantation doses above  $1.8 \times 10^{13} \text{ cm}^{-2}$ , the dark current increased drastically and was comparable to the photocurrent. We think that the increased hopping conductivity<sup>9,10</sup> due to the larger point defect concentration was responsible for this behavior.

The family of curves in Figs. 2(b)–2(d) relate the terahertz power to the photocurrent for a constant laser power. For doses higher than  $1.8 \times 10^{12} \text{ cm}^{-2}$ , there was a quadratic dependence, as expected from formula (1), followed by a saturation component which appeared at lower photocurrents as the frequency increased. According to Reklaitis *et al.*,<sup>11</sup> an electron saturation velocity enhancement is expected for samples with smaller electron lifetime. This effect would explain why the superlinear increase in dc photocurrent with voltage (due to both electrons and holes) does not lead to a superquadratic increase of terahertz power, which is mainly due to electron photocurrent: the increased electron lifetime was counteracted by a reduced electron saturation velocity, so that the net effect was a saturation of the electron photocurrent. Higher frequencies are affected by the saturation mechanism at lower photocurrents because the influence of the carrier lifetime in the power-attenuating factor  $1 + (\omega\tau)^2$  from formula (1) is frequency dependent. Thus, for high frequencies and low currents, even small changes in the carrier lifetime due to the increase of carrier lifetime with voltage may attenuate the power considerably. For the high average electric field conditions (up to 100 kV/cm) in the interdigitated region, electron scattering into the  $L$  and  $X$  valleys might occur. Nevertheless, scattering with electron traps and other defects probably occurs before electrons reach enough kinetic energy as needed for intervalley scattering.

We measured the frequency response [Fig. 3(a)] of photomixers for a constant bias voltage of 3 V and adjusted the laser power so that the photocurrent was similar in all photomixers ( $250 \mu\text{A}$ ). By this procedure we held the numerator of Eq. (1) constant for all samples so that we could directly compare the terahertz power between different doses and extract the recombination lifetime by a fit to the measured data [inset of Fig. 3]. Note that adjusting the voltage instead of laser power to achieve the same photocurrent in all photomixers have allowed comparison of curves but would not be representative since the carrier lifetime of every individual photomixer would have been altered according to the applied voltage. The tendency shows that the higher the dose, the higher the terahertz power for the same dc photocurrent, which is related to the reduced carrier lifetime. Nevertheless, there is a limit to the maximum implantation dose since above  $10^{13} \text{ cm}^{-2}$  the dark current increased dramatically, whereas, due to the reduced mobility and lifetime, the photocurrent diminished. For example, the dark current at a dose

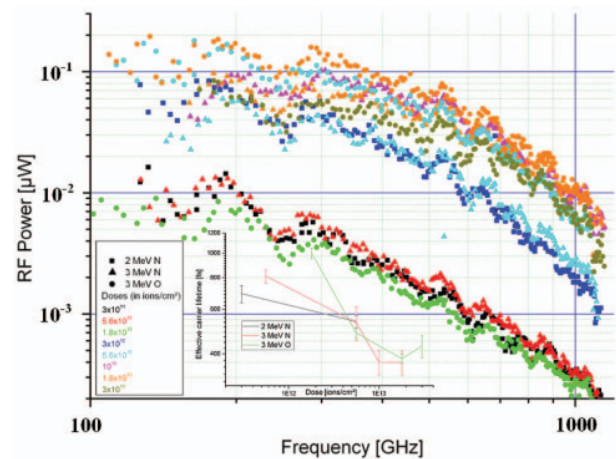


FIG. 3. (Color) (a) rf power vs frequency for different doses and energies. The bias voltage was 3 V and the photocurrent  $250 \mu\text{A}$ . (Inset) By fitting the theoretical curve Eq. (1) to the measured data, the effective carrier lifetime was estimated. The fits were calculated for a MSM structure capacity of 1.5 fF, yielding a 3 dB bandwidth of 1.45 THz for the RC constant.

equal to  $3 \times 10^{13} \text{ cm}^{-2}$  accounted for  $\sim 30\%$  of the total current and we had to raise the optical power to 100 mW, which was the device burnout point, to maintain the same photocurrent as for the rest of the samples. From these measurements we conclude that implanting nitrogen and oxygen ions at energies of 3 MeV and doses around  $10^{13} \text{ cm}^{-2}$  achieves a compromise between dark current, photoconductivity, and bandwidth. The carrier lifetime and rc power have been shown to be slowly varying functions of the fabrication conditions, without showing any abrupt dependencies as occurs with LT GaAs. This, combined with our excellent control of energy and dose during implantation, allows us to fabricate a highly reproducible photoconductive material. The reported terahertz power performance of ion-implanted photomixers is comparable to our best results achieved with LT GaAs.<sup>12</sup>

<sup>1</sup>I. S. Gregory, C. Baker, W. R. Tribe, M. J. Evans, H. E. Beere, E. H. Linfield, A. G. Davies, and M. Missous, *Appl. Phys. Lett.* **83**, 4199 (2003).

<sup>2</sup>A. Claverie, F. Namavar, and Z. Liliental-Weber, *Appl. Phys. Lett.* **62**, 1271 (1993).

<sup>3</sup>A. Krotkus, S. Marcinkeviciu, J. Jasinski, M. Kaminska, H. H. Tan, and C. Jagadish, *Appl. Phys. Lett.* **66**, 3304 (1995).

<sup>4</sup>T.-A. Liu, M. Tani, and C.-L. Pan, *J. Appl. Phys.* **93**, 2996 (2003).

<sup>5</sup>M. Mikulics, M. Marso, I. Cámara Mayorga, R. Stanček, P. Kováč, S. Wu, Xia Li, M. Khafizov, R. Sobolewski, E. A. Michael, R. Schieder, M. Wolter, D. Buca, A. Förster, P. Kordoš, and H. Lüth, *Appl. Phys. Lett.* **87**, 143501 (2005).

<sup>6</sup>E. R. Brown, K. A. McIntosh, F. W. Smith, M. J. Manfra, and C. L. Denis, *Appl. Phys. Lett.* **62**, 1206 (1992).

<sup>7</sup>A. W. Sarto and B. J. Van Zeghbroeck, *IEEE J. Quantum Electron.* **33**, 2188 (1997).

<sup>8</sup>N. Zamdmer, Qing Hu, K. A. McIntosh, and S. Verghese, *Appl. Phys. Lett.* **75**, 2313 (1999).

<sup>9</sup>C. Jagadish, H. H. Tan, J. Jasinski, M. Kaminska, M. Palczewska, A. Krotkus, and S. Marcinkevicius, *Appl. Phys. Lett.* **67**, 1724 (1995).

<sup>10</sup>G.-R. Lin, F. Ganikhanov, W.-C. Chen, C.-S. Chang, and C.-L. Pan, *Appl. Phys. Lett.* **69**, 996 (1996).

<sup>11</sup>A. Reklaitis, A. Krotkus, and G. Grigaliūnaitė, *Semicond. Sci. Technol.* **14**, 945 (1999).

<sup>12</sup>I. Cámara Mayorga, P. Muñoz Pradas, E. A. Michael, M. Mikulics, A. Schmitz, P. van der Wal, C. Kaseman, R. Güsten, K. Jacobs, M. Marso, H. Lüth, and P. Kordoš, *J. Appl. Phys.* **100**, 043116 (2006).



## Terahertz continuous-wave large-area traveling-wave photomixers on high-energy low-dose ion-implanted GaAs

E. A. Michael,<sup>a)</sup> I. Cámara Mayorga, and R. Güsten  
*Max Planck-Institut für Radioastronomie, Auf dem Hügel 51, 53121 Bonn, Germany*

A. Dewald  
*Institut für Kernphysik, Universität zu Köln, Zùlpicher Str. 77, 50937 Köln, Germany*

R. Schieder  
*1. Physikalisches Institut, Universität zu Köln, Zùlpicher Str. 77, 50937 Köln, Germany*

(Received 19 January 2007; accepted 12 March 2007; published online 25 April 2007)

Nitrogen ion implantation at 3 MeV and low doses into commercial semi-insulating GaAs ( $10^7 \Omega \text{ cm}$ ) is used to manufacture continuously operated metal-semiconductor-metal terahertz photomixer radiation sources based on a traveling-wave interdigitated-finger coplanar stripline structure. The authors systematically investigated the terahertz efficiency over the implantation dose range of  $5.6 \times 10^{11}$ – $1.8 \times 10^{13}$  ions/cm<sup>2</sup> and determined the optimum implantation dose range for operation in the frequency range 500–1000 GHz, where a significant higher efficiency is obtained compared to low-temperature-grown GaAs. © 2007 American Institute of Physics.  
 [DOI: 10.1063/1.2722235]

Ion implantation into GaAs opens up a promising way to design ultrafast materials for more efficient continuous-wave terahertz photonic radiation sources based on the beat of two near-infrared diode lasers separated in frequency in the terahertz range. For 15 years, low-temperature-grown (LT) GaAs is established as the material of choice for ultrafast photoconductive switches and terahertz photomixers, and therefore has been studied extensively.<sup>1</sup> Grown by a molecular beam epitaxy process at 200–300 °C and under an arsenic overpressure, LT-GaAs is a nonstoichiometric material with 1%-2% of excess arsenide, which creates a high concentration of point defects in the crystal structure. Therefore as-grown LT-GaAs already shows a subpicosecond photoelectron lifetime, but electron mobility and dark resistance are still too low due to a hopping conductivity between the closely spaced arsenic point defects.<sup>2</sup> To obtain higher dark resistance and mobility at only slightly increased electron trapping time, the material is annealed at 400–600 °C,<sup>2</sup> allowing excess arsenide in point defects to rearrange into precipitates.<sup>3</sup> However, excess arsenide, growth and annealing temperatures, as well as unavoidable contaminations all together result in a complexity of the material production process, explaining well the experienced lack of reproducibility of the best cw terahertz-efficiency results with LT-GaAs.

In contrast to this, the ion-implantation process is much simpler and therefore shows a much better reproducibility of the terahertz-efficiency results, because commercial semi-insulating GaAs wafers of proven and documented constant quality can be used and the implantation energy and dose can be controlled very precisely. During the implantation process, point defects—vacancies and corresponding antisites and interstitials containing the displaced lattice atoms—are produced. However, by adjusting the dose, the concentration of defects can be tailored to obtain an ultrashort carrier lifetime and, at the same time, preserve a reasonably good mobility, while no trace of implantation atoms is produced in

the terahertz-active surface layer if the implantation energy is chosen high enough.

In this letter, we report that an implantation process at MeV energies into commercial semi-insulating GaAs of  $10^7 \Omega \text{ cm}$  and doses below the amorphization dose without any subsequent annealing already results in a high-resistivity and short-carrier-lifetime material which is superior to LT-GaAs for continuous-wave terahertz photomixing. Moreover, we have characterized the behavior of the photomixers as the implantation dose is varied and therefore could extract information about an optimal implantation dose range.

Using the tandem accelerator at the Institute for Nuclear Physics at the University of Cologne, we have implanted N<sup>4+</sup> ions at 3 MeV. Density profiles of the produced defects and the implanted atoms were calculated with the Stopping and Range of Ions in Matter (SRIM) program.<sup>4</sup> At high implantation energies, most ions are implanted far below a surface layer of about 0.5  $\mu\text{m}$  thickness at high bias where most terahertz power is generated at an electrode separation of  $s=1 \mu\text{m}$  (“terahertz-active layer,” Fig. 1). The ion concentration in this region is a factor of  $10^3$  lower than the peak concentration, whereas the vacancy density profile is nearly flat below the surface. Another reason to use high implantation energies is to reduce the lifetime and therefore strongly reduce the density of photocarriers produced at a depth of a couple of micrometers, which are not only useless for terahertz generation but also absorb energy from the terahertz field below the stripline, an effect which will be reported elsewhere.

The ion beam had a full width at half maximum (FWHM) of about 3 mm and was scanned over an area of about  $3 \times 3 \text{ cm}^2$  to cover a quarter piece of a 2 in. wafer. To achieve constant implantation density over this area, Lissajous figures were suppressed by applying nonharmonic frequency signals to the two scan axes. In order to prevent overheating of the GaAs sample and subsequent formation of amorphous zones, the ion current density within the beam was held below  $0.5 \mu\text{A}/\text{cm}^2$ .<sup>5</sup>

On all as-implanted wafers, an identical interdigitated-finger traveling-wave (TW) structure as described earlier<sup>6</sup>

<sup>a)</sup>Electronic mail: michael@ph1.uni-koeln.de

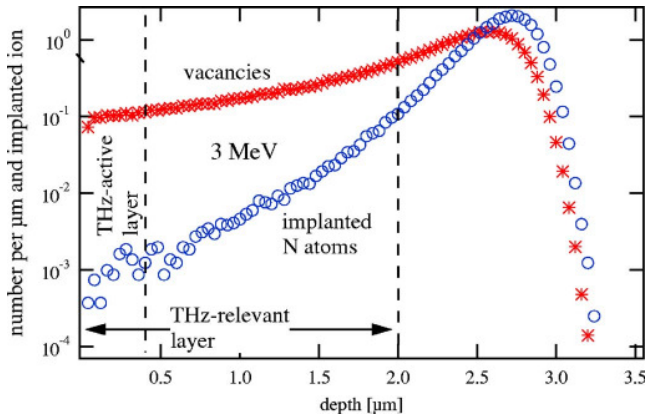


FIG. 1. (Color online) Nitrogen implantation and vacancy profile calculated with SRIM for  $10^5$  ions. As the used tandem accelerator preferentially runs stable at energies above 10 MeV, aluminum foils of calculated and prepared thickness were used to slow down the ions in front of the samples to the desired energy. According to SRIM, the energy dispersion was around 10% FWHM for all implantation energies. Also, the resulting angle dispersion avoids possible channeling to the crystal axis.

was manufactured using a 10/200 nm Ti/Au layering with electrode gap of  $s=1 \mu\text{m}$  and a finger width of  $0.2 \mu\text{m}$ . This work was done on a commercial basis at the MC2 microstructure facility at Chalmers Technical University, Gothenburg, Sweden.

The TW mixers were tested with the free-space traveling-wave optics setup described in Ref. 7, which implements an automatic phase-matching angle between the two laser colors for all terahertz frequencies. Terahertz powers were measured with a carefully calibrated LiHe-cooled InSb hot-electron bolometer.<sup>6,8</sup>

Assuming pure traveling-wave behavior of the mixer,<sup>6,7</sup> the frequency roll-off of the terahertz power measured for a bias voltage of 12 V is fitted to a one-time-constant Lorentz curve  $P_{\text{THz}}(\nu) \sim 1/[1+(2\pi\tau\nu)^2]$  (Fig. 2). Values of these fit curves at 800 GHz are plotted against the implantation dose (Fig. 3), retrieving an optimum implantation dose range of  $5\text{--}10 \times 10^{12} \text{ cm}^{-2}$  for a constant optical power. In order to

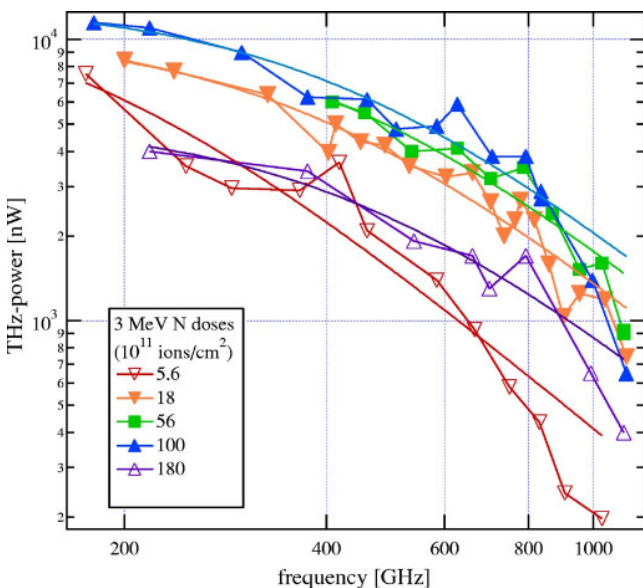


FIG. 2. (Color online) Frequency plots of traveling-wave mixers at bias voltages of 12–13.5 V and constant optical power of 330 mW.

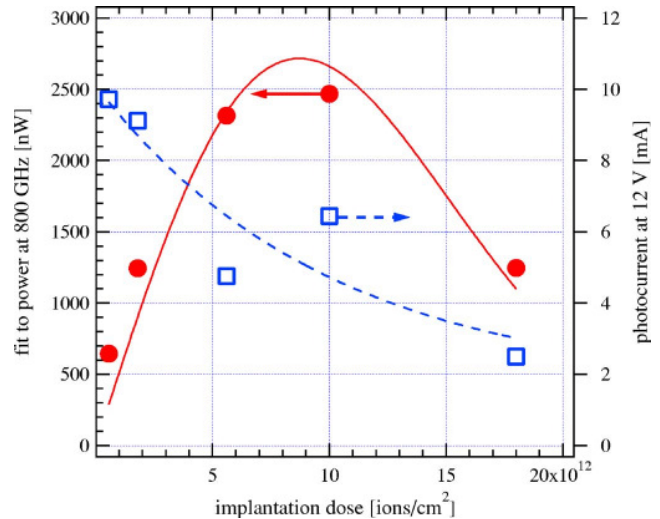


FIG. 3. (Color online) Determination of optimum implantation dose: terahertz-power values at 800 GHz taken from the Lorentz fits to the terahertz-power curves of Fig. 2 (at 12 V and 330 mW). Plotted also are the corresponding photocurrents. The curves are just guides for the eyes and are not based on a physical model, except that we assumed the power at 800 GHz to be negligible for zero dose (pure semi-insulating GaAs).

determine also the dose dependency of the time constant  $\tau$  with sufficient precision from frequency fits, a much tighter frequency sampling is needed due to standing waves in the optical setup. Here, a complementary experiment with small-area mixers in spiral antennas pumped with commercial mode hop-free tunable diode lasers<sup>9</sup> clearly revealed the expected decrease of carrier lifetime with implantation dose.<sup>10</sup> This is consistent with the observed decrease of photocurrent towards higher implantation dose [Figs. 4(b) and 3]. The relation  $j_{\text{ph}}(E) \sim \tau_e(E)v_{\text{dr,sat}}$  reflects this tendency at high fields, where the saturated drift velocity  $v_{\text{dr,sat}}$  is constant with respect to the  $E$  field, but might increase towards shorter recombination times.<sup>11</sup>

Typical  $I$ - $V$  curves measured [Fig. 4(b)] consist of three regimes<sup>12</sup> in terms of  $I \sim V^n$ : (1) Ohmic ( $n=1$ ) at  $V < 1$  V, (2) sublinear ( $n < 1$ )  $1 \text{ V} < V < 4$  V, and (3) a transition towards a quadratic ( $n=2$ ) regime at  $V > 10$  V. While regions (1) and (2) correspond to an increase and saturation of the electron drift velocity with the electric field (theoretical plateau<sup>13</sup> smeared out due to electric field gradient with depth), region (3) can be explained by the increase of trapping time due to Coulomb-barrier lowering of the traps,<sup>14</sup> and/or by the production of secondary carriers through impact ionization of traps (avalanche effect), which is also equivalent to an increase of effective photoelectron lifetime.<sup>12,15</sup> The transition to quadratic behavior of the photocurrent in our ion-implanted mixers occurs smoother than in LT-GaAs [rather sharp onset at  $V/s \approx 5 \text{ V}/\mu\text{m}$  (Ref. 6)] and seemingly at electric field strengths and with a smoothness increasing with the implantation dose, which suggests the avalanche effect as the primary reason for carrier trap time increase with voltage. Accordingly, we attribute the sharper onset in LT-GaAs to the larger collision cross section of the arsenic precipitates for the production of secondary free carriers.

Within the one-time-constant (traveling-wave) model for photomixers,<sup>6,7</sup> the saturation of the terahertz power-photocurrent curve [Fig. 4(a)], found synchronous to the on-

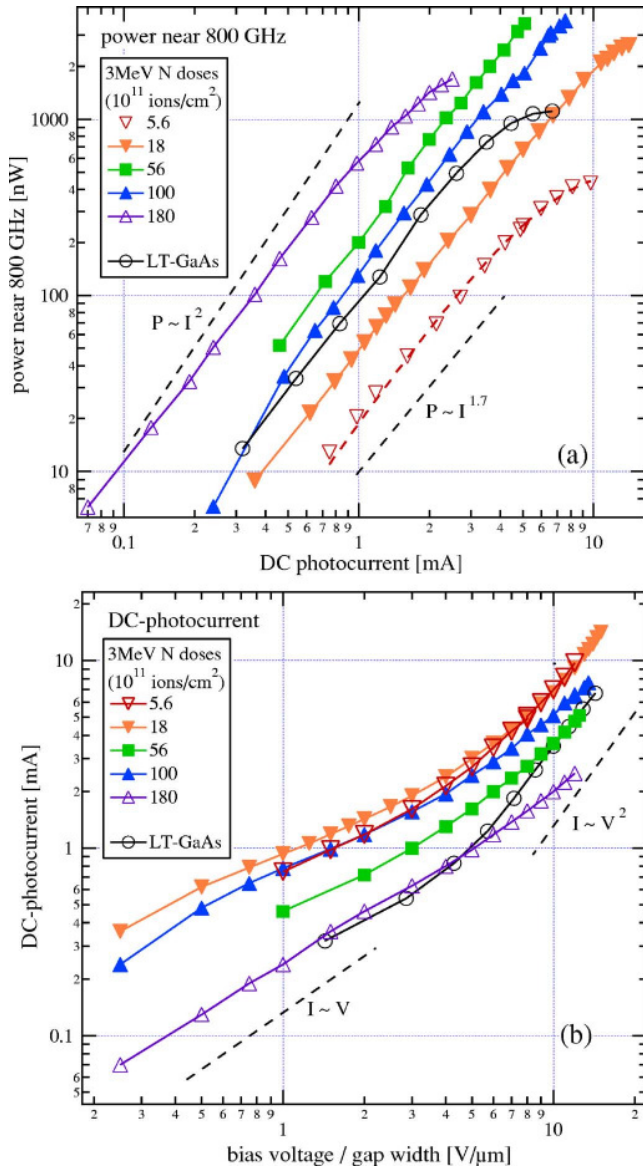


FIG. 4. (Color online) (a) Terahertz power vs voltage-dependent dc photocurrent for different implantation doses, at a constant optical power of 330 mW. The best result for LT-GaAs ( $s=1.4 \mu\text{m}$ ) is plotted for comparison (from Ref. 6). For higher currents, the power curves can be fitted by  $\sim I_{\text{ph}}^2 \exp(-bI_{\text{ph}})$  (dashed curve for dose  $5.6 \times 10^{11}$ ); for low currents, better by  $\sim I^{1.7}$ . (b) dc-photocurrent as a function of voltage at 330 mW. Not shown: Terahertz power as a function of optical power  $P_{\text{opt}}$  shows a saturation independent of implantation dose:  $P_{\text{THz}} \sim I_{\text{ph}}^2 \exp(-bI_{\text{ph}})$  with  $b \approx 0.06 \text{ mA}^{-1}$  (or  $\sim I_{\text{ph}}^{1.8}$ ) and  $I_{\text{ph}} \sim P_{\text{opt}}$  up to 330 mW in good approximation.

set of quadratic behavior in the  $I$ - $V$  curve, can also be modeled with the increase of carrier lifetime with voltage. The apparent increase of onset voltage for quadratic behavior in the  $I$ - $V$  curve with implantation dose corresponds to a consistent reduction of saturation in the  $P_{\text{THz}}$ - $I$  curve. However, the reoccurrence of saturation of terahertz power versus photocurrent in the material with highest dose [Fig. 4(a)] without a corresponding feature in the  $I$ - $V$  curve must then have an additional yet unknown reason. Although the mechanism of

trapping free carriers and their recombination through point defects may be similar in both materials, the absence of additional very large defects, i.e., precipitates which reduce the electron mobility, may not behave as efficient electron traps, and deteriorate the increase of carrier lifetime with voltage, is a clear advantage of ion-implanted material.

Breakdown voltage and associated current (at 330 mW optical illumination over a line focus of  $150 \mu\text{m}$  length) were not tested intentionally because of the small number of available mixers. Therefore, the saturation in the samples of optimal dose range might lie outside the recording range or above the breakdown voltage.

Comparison to samples implanted with oxygen at 3 MeV and comparison between nitrogen and oxygen at 5 MeV showed that the residual concentration of implanted atoms in the terahertz-active layer, lying a factor of 1000 lower than the peak value of the profile, is of no relevance to the performance compared to the point defects created by collisions.

We have shown that high-energy (3 MeV) ion implantation into semi-insulating GaAs at doses of  $5 \times 10^{12} - 1 \times 10^{13} \text{ ions/cm}^2$  and without annealing results in a material superior to LT-GaAs with respect to the terahertz-power performance of continuous-wave dual-laser operated terahertz photoconductive mixers. This is partly due to the fact that the voltage saturation, which is similar to LT-GaAs at too low and too high doses, is strongly reduced in the optimal dose range.

This work was supported by the Deutsche Forschungsgemeinschaft through Grant No. 494 and by the Max Planck Gesellschaft.

- <sup>1</sup>M. Stellmacher, J. Nagle, J. F. Lampin, P. Santoro, J. Vaneecloo, and A. Alexandrou, *J. Appl. Phys.* **88**, 6026 (2000).
- <sup>2</sup>I. S. Gregory, C. Baker, W. R. Tribe, M. J. Evans, H. E. Beere, E. H. Linfield, A. G. Davies, and M. Missous, *Appl. Phys. Lett.* **83**, 4199 (2003).
- <sup>3</sup>E. S. Harmon, M. R. Melloch, J. M. Woodall, D. D. Nolte, N. Otsuka, and C. L. Chang, *Appl. Phys. Lett.* **63**, 2248 (1993).
- <sup>4</sup>J. F. Ziegler, J. P. Biersack, and U. Littmark, *The Stopping and Range of Ions in Solids* (Pergamon, New York, 1985), Vol. 1; see also <http://www.srim.org/>
- <sup>5</sup>E. Wendler, W. Wesch, and G. Götz, *Nucl. Instrum. Methods Phys. Res. B* **52**, 57 (1990).
- <sup>6</sup>E. A. Michael, B. Vowinkel, R. Schieder, M. Mikulics, M. Marso, and P. Kordos, *Appl. Phys. Lett.* **86**, 111120 (2005).
- <sup>7</sup>E. A. Michael, *Semicond. Sci. Technol.* **20**, 164 (2005).
- <sup>8</sup>A recent cross-check with a Golay cell suggests that the measured terahertz-power values may be reduced by a factor of up to 3.
- <sup>9</sup>I. Cámara Mayorga, P. Muñoz Pradas, E. A. Michael, M. Mikulics, A. Schmitz, P. van der Wal, C. Kaseman, R. Güsten, K. Jacobs, M. Marso, H. Lüth, and P. Kordoš, *J. Appl. Phys.* **100**, 043116 (2006).
- <sup>10</sup>I. Cámara Mayorga, E. A. Michael, A. Schmitz, P. van der Wal, R. Gues-ten, K. Maier, and A. Dewald (unpublished).
- <sup>11</sup>A. Reklaitis, A. Krotkus, and G. Grigaliūnaitė, *Semicond. Sci. Technol.* **14**, 945 (1999).
- <sup>12</sup>J. P. Ibbetson and U. K. Mishra, *Appl. Phys. Lett.* **68**, 3781 (1996).
- <sup>13</sup>D. Saeedkia, R. R. Mansour, and S. Safavi-Narini, *IEEE J. Quantum Electron.* **41**, 1188 (2005).
- <sup>14</sup>N. Zamdmer, Q. Hu, K. A. McIntosh, and S. Verghese, *Appl. Phys. Lett.* **75**, 2313 (1999).
- <sup>15</sup>J. P. Ibbetson, J. S. Speck, N. X. Nguyen, A. C. Gossard, and U. K. Mishra, *J. Electron. Mater.* **22**, 1421 (1993).



# Curriculum Vitae



---

## Personal Details

**Name:** Iván Cámara Mayorga.

**Address:**

**Tel.:**

**Birth Date:**

**Marital Status:**

**Nationality:** Spanish.

---

## Education

**PhD in Physics (summa cum laude – Ausgezeichnet 0.0)**

2006 – 2008. University of Bonn (Germany).

Doctoral thesis “*Photomixers as tunable THz local oscillators*”.

Supervisor Prof. Dr. Karl Maier.

**Master Degree in Physics (Licenciado en Ciencias Físicas).**

2006. National Estate Distance University (UNED). Madrid (Spain).

**Master Degree in Electrical Engineering (Ingeniero de Telecomunicación)**

1998 – 2000. Alfonso X El Sabio University. Madrid (Spain).

**Bachelor Degree in Electrical Engineering (Ingeniero Técnico de Telecomunicaciones)**

1994 – 1998. Alcalá de Henares University (Spain).

**High School in IB “Carlos III” (COU)**

1994. Toledo (Spain) - with Honours.

---

**Professional Experience:****Max Planck Institut für Radioastronomie (Bonn - Germany) 2002 – Present.**

Research Associate (Wissenschaftlicher Mitarbeiter)

- R & D of Photonic Local Oscillators (100 GHz - 2.7 THz) for radio astronomy applications.
- R & D of Laser Systems (Solid State Ti:Sa and Semiconductor Lasers) and comb generators.
- Quasioptics & Cryogenic Design.

**University Alfonso X (Madrid – Spain).**

**May 2001 - July 2002.**

Associate Professor in Telecommunications Engineering.

Responsible for:

- Electromagnetic Theory.
- Microwave Theory.
- Communications Electronics.
- Signal & Systems Laboratory.
- Optical Communications Laboratory.

**Nortel Networks. RF Planning Engineer (Madrid – Spain).**

**July 2000 - September 2001.**

Contractor in Xfera UMTS project.

- UMTS RF Planning for the north of Madrid.
- Simulation of signal coverage.
- On field activities related to antenna site acquisition and design for civil engineering.

**Alcatel Espacio. Department of Radio frequency Engineering. (Madrid – Spain). Scholarship from January 2000 - July 2000.**

Simulation of satellite transponder circuits (Phase locked loops, oscillators) with the simulation tool application Libra.

**Moscow Aviation Institute. Summer 1997. Moscow – Russia.**

Scholarship

Development of a software application for the Glonass Satellite Positioning System through IAESTE (International Association for a technical experience).

---

**Computer Science Skills**

- **RF Design** and Simulation of microstrip, coplanar waveguide, coplanar strip transmission lines and antennas with IE3D (Zeland Software).
- **TCAD Semiconductor Simulation** with ATLAS (Sylvaco)
- **Electronic circuit simulation** with PSpice
- **Programming languages** Matlab, C, C++, Java, Pascal & Visual Basic.
- **Microsoft Office** and Database design with MS Access.

---

**Languages**

- **English**  
Fluent.
  - **German**  
Fluent.
  - **Russian**  
Fluent.
  - **Spanish**  
Mother tongue.
-



# Erklärung

Ich versichere, daß ich diese Arbeit selbständig verfaßt und keine anderen als die angegebenen Quellen und Hilfsmittel benutzt sowie Zitate kenntlich gemacht habe.